SLAC – PUB – 4287
April 1987
(T/E)

EXPERIMENTAL TESTS OF QUANTUM CHROMODYNAMICS*

JONATHAN DORFAN

Stanford Linear Accelerator Center
Stanford University, Stanford, California, 94305

Presented at the SLAC Summer Institute on Particle Physics,
Stanford, California, July 28 – August 8, 1986

* Work supported by the Department of Energy, contract DE – AC03 – 76SF00515.

1. INTRODUCTION

This is a write-up of two lectures given at the 1986 SLAC Summer Institute. The topic of the lectures was "Experimental Tests of Quantum Chromodynamics" and the level was supposed to be aimed at particle physicists who had recently received their doctorates. "Experimental Tests of QCD" is a vast topic and it is impossible to cover all the relevant measurements in two lectures. So I chose a series of topics which could be covered in this time period. My choice of topics presumably will not correspond to everybody else's favorite list, my emphasis of the relative importance of one area will differ from others. But those were my choices and I have in no way tried to make this write-up more complete than were the lectures. I have tried hard to emphasize the measurements and, in particular, how they relate to extracting reliable tests of QCD. I have not stressed the theoretical formalism – much of that area is covered in Rick Field's companion lectures.

QCD provides an SU(3) gauge invariant, field theoretical formalism for the interactions of quarks and gluons. QCD forms the basis of our understanding of what we used to call the "Strong Interactions" – it is in fact a cornerstone of our Standard Model of SU(3)$\wedge$ SU(2)$\wedge$ U(1). It is therefore crucial that we make objective and meaningful tests of QCD. However, this is not a simple matter. Perturbative QCD describes the interactions of partons (quarks and gluons) which at short distances ($\leq$ confinement radius) act as quasi-free constituents. However, we observe hadrons which are the long- distance manifestation of the confined partons. The bridge between the short distance (perturbative) and long distance (non-perturbative) behavior is not well understood theoretically and we are forced to use models – fragmentation models – for this bridge. The parton dynamics which we are trying to test must be inferred indirectly from the distribution of the hadronic fragments. There are some additional practical complications. Since we are trying to study behavior at the confinement scale, we must have probes which have large magnification or large momentum trans-

fer (Q^2). The perturbative behavior is characterized by a coupling constant α_s which is both large ($\simeq 0.2$) and depends on Q^2. This makes the calculations of the theoretical predictions difficult and, in particular, one is always confronted with the question as to the level of convergence associated with the finite order of the calculations. So there are significant complications in the experimental measurements and the theoretical predictions. The level and character of these complications is different for different tests – each must be examined separately to establish the validity or limitations provided by the particular comparison of an experimental measurement with a theoretical prediction. The upshot of this is that, in this reviewers mind, no single experimental measurement provides a conclusive test of the validity of QCD; there are no "smoking guns." Rather we are forced to consider measurements from a wide range of processes spanning a broad range of Q^2. In this way one hopes to build confidence in the validity of QCD based on a wide range of positive indicators.

When we think about testing QCD, we need to remember the tremendous success of its "predecessor," the quark parton model (QPM) exemplified best by its ability to describe the scaling behavior of deep-inelastic lepton-nucleon scattering. It is clear that this model is inadequate to explain all the data we have to date. But much of the low Q^2 data can be interpreted in terms of this simple picture and, as a device, we will often pose the question of when the data begins to depart from this picture and whether QCD, in its role of replacing the QPM, accounts for the disagreements. We recall that the essence of the QPM is that partons in the nucleus are treated as free, point-like constituents which interact with a high Q^2 probe via their electric charge. It is clear that QCD must approximate this behavior at short distances while at the same time adding sufficient complexity to remedy the inadequacies of the QPM (like non-scaling). Part of the "magic" of QCD is the notion of confinement which provides just such a picture. The color force is such that at distances $\lesssim$ the confinement radius ($\approx$ 1 Fermi), quarks act as free constituents. However, at distances larger than the confinement radius the color restoring force becomes increasingly strong and the

quarks cannot be plucked from the color field. De-excitation of the energy stored in the color field occurs via the emission of hadrons, the primary quark eombining with an antiquark liberated from the vacuum, etc etc. Clearly then, the QCD coupling constant is not a constant but is a function of distance or in experimental terms a function of the magnification of the probe, Q^2. So QCD, via this notion of confinement, provides a natural mechanism for mimicking the QPM at short distances while adding sufficient complexity to make it distinguishable from the QPM. The running of the QCD coupling constant is given in second order by

$$\alpha_s(Q^2) = \alpha_s^o(Q^2)[1 - b'\alpha_s^o(Q^2)(\ell n \ell n Q^2/\Lambda^2)]$$

where

$$\alpha_s^o = (b\ell n Q^2/\Lambda^2)^{-1}, b = \frac{33 - 2N_f}{12\pi}$$

$$b' = \frac{(153 - 19N_f)}{2\pi(33 - 2N_f)}.$$

Here N_f is the number of quark flavors and Λ is the QCD scale parameter.

It is worth remembering that there exists a major ambiguity in the interpretation of perturbative expansions in QCD arising from the choice of the expansion parameter. Any observable ρ can take on the general form

$$\rho = C_o\alpha_s(Q^2)\{1 + C_1(Q^2)\frac{\alpha_s(Q^2)}{\pi} + C_2(Q^2)\frac{\alpha_s^2(Q^2)}{\pi^2} + ...\}.$$

The ambiguity arises in that the expansion coefficients $C_i(Q^2)$ depend both on the definition of $\alpha_s(Q^2)$, that is on the "scheme," and on the choice of scale, Q^2. Of course, when working to all orders, ρ is always the same independent of the choice of scheme and scale. However at finite orders, which is what we contend with in real QCD tests, we must keep this ambiguity foremost in our minds. In first order, for example, a change in C_1 can be compensated for either by a change in α_s or Q^2.

With this superficial introduction we now turn our attention to a discussion of the experimental tests.

2. TESTS IN THE e^+e^- CONTINUUM

The e^+e^- colliding beam facilities are excellent for testing QCD because the parton topologies are relatively simple. The basic process is the production of a quark (q) antiquark ($\bar{q}$) pair via a high Q^2 photon (see Fig. 1(a)). It is conventional to take $Q^2 = E^2_{cm}$, where E_{cm} is the total collision energy. This basic process provides direct production of the QCD constituents and in this sense the environment is very "clean." Measurements made at Q^2 in which Fig. 1(a) dominates cannot distinguish between QPM and QCD. To do that requires increasing the Q^2 until one sees the process in Fig. 1(b) which corresponds to the first order QCD process in which a gluon is radiated by the quark or antiquark. Higher level gluon radiation processes (both of the tree and virtual correction type) should become evident at even larger Q^2 (Fig. 1(c)). If this pattern of processes can be isolated in the data one would have a useful laboratory for testing QCD.

What would we expect to observe experimentally? At low $Q^2 \leq 200$ GeV^2 Fig. 1(a) will dominate. Below $Q^2 \leq 25$ GeV^2 one will see roughly spherical events with no obvious jet structure. This is because the kinetic energy of the q(or $\bar{q}$) is insufficient to provide a collimated set of hadrons. However as Q^2 is raised, the hadrons which result from the q(or $\bar{q}$) fragmentation process will follow the parton production direction and clear back-to-back, 2-jet structures should be seen. The production angular distribution of the jet-jet axis should be characteristic of underlying spin $\frac{1}{2}$ constituents. As one raises $Q^2 \geq 600$ GeV^2 one moves into the regime of Fig. 1(b) and clear coplanar, 3-jet structures should be seen. The 3-jet kinematics should be consistent with the QCD matrix elements and should reflect the vector nature of the gluon. At even higher $Q^2 \geq 1000$ GeV^2 one should begin to see evidence for the processes in Fig. 1(c) namely 4-jet topologies. As we will discuss below, this pattern of observations is quite clearly seen and QCD accounts remarkably well for the qualitative features of the data. Quantitative measurements of α_s are, however, difficult to achieve.

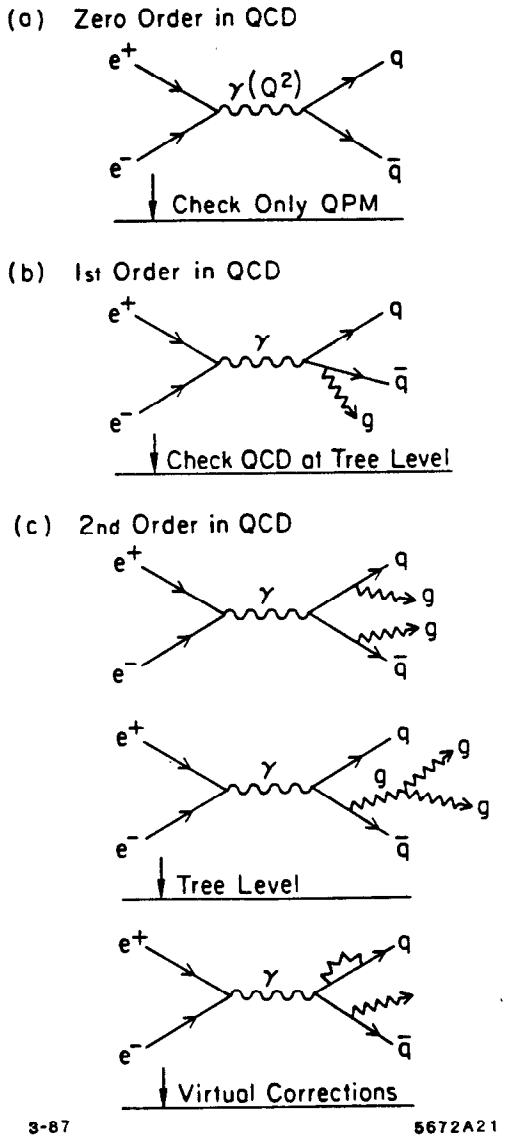

Fig. 1. Feynman diagram for the process e^+e^- →hadrons to zero order QCD(a), first order QCD(b) and second order QCD(c).

2.1 MEASUREMENT OF R

Before we proceed to the study of the $e^+e^- \rightarrow$hadrons cross section in processes corresponding to increasing orders in perturbative QCD, we should ask why we cannot sum these pieces up and obtain a significant test of QCD from the total cross section. In the QPM, the calculation of the total cross section is straight-forward (see Fig. 1(a)). For any final state quark flavor f the differential cross section for $e^+e^- \rightarrow f\bar{f}$ is given by

$$\frac{d\sigma_{f\bar{f}}}{dcos\theta} = \frac{\pi\alpha^2 Q_f^2}{2s}(1 + cos^2\theta)$$

where Q_f = charge of the quark of flavor f, $s = E_{cm}^2$, θ is the polar angle of the quark relative to the incoming e^- direction, and α is the fine structure constant.

For N_f flavors

$$\sigma_{HAD} = \sum_{N_f} \int_{-1}^{+1} dcos\theta \frac{d\sigma_{f\bar{f}}}{dcos\theta} = \frac{4\pi\alpha^2}{3s} \sum_{N_f} Q_f^2.$$

If in fact quarks come in three colors, then

$$\sigma_{HAD} = 3 \sum_{N_f} \frac{4\pi\alpha^2}{3s} Q_f^2.$$

It is more convenient to remove the energy dependence and consider the quantity R:

$$R = \frac{\sigma_{HAD}}{\sigma_{\mu^+\mu^-}} = \sigma_{HAD} / \frac{4\pi\alpha^2}{3s} = 3 \sum_{N_f} Q_f^2.$$

This then is the QPM, or zero order QCD, result. To test QCD we need a calculation which takes into account higher orders – namely all the gluon radiation corrections. It turns out that these corrections were calculated many years ago[1]

and are considered to be one of the least controversial and most trustworthy QCD calculations available to date. The usual term accorded the calculation of R is "gold plated." The result is

$$R(Q^2 = E_{cm}^2) = 3\sum Q_f^2(1 + \alpha_s/\pi + C_2(\alpha_s/\pi)^2.....) \qquad (1)$$

where C_2 depends on the renormalization scheme. However, independent of the choice of renormalization scheme, $C_2(\alpha_s/\pi) << 1$ and the expansion converges. For $N_f = 5$ and $\alpha_s = 0.13$ one obtains the values for C_2 for three different renormalization schemes as shown in Table I.

Table I

SCHEME	C_2	$C_2(\frac{\alpha_s}{\pi})^2$	$C_2(\frac{\alpha_s}{\pi})^2 / (\frac{\alpha_s}{\pi})$
$\overline{\text{MS}}$	1.986-0.115 N_f	0.002	5%
MS	7.359-0.441 N_f	0.009	22%
MOM	-2.193+0.162 N_f	-0.002	-5%

So we have a reliable calculation of R_{QCD}. However, it differs from R_{QPM} by only $\frac{\alpha_s}{\pi} \approx 4\%$ and individual experiments have great difficulty achieving a level of precision sufficient to see such a small effect. The best experimental measurements of R come from PEP and PETRA and have measurement errors of $\gtrsim 2\%$. Where theory is in outstanding shape, the experiments are not.

Experimentally, R is an attractive quantity to study because it should be measured independently of the non-perturbative effects of hadronization. The measurement is in principle simple; one counts hadronic events ($N_{HADRONS}$, which are rather easy to isolate at high energies) and normalize to the measured luminosity ($\mathcal{L}$):

$$R = \frac{N_{Hadrons} - N_{Backg}}{A(1+\delta)\mathcal{L}\sigma_{\mu^+\mu^-}}$$

where N_{Backg} accounts for events arising from background processes, A is the detector acceptance and δ takes into account QED radiative corrections.

The main systematic errors arise in the measurement of the luminosity (normalization of R) and the detector acceptance corrections. To illustrate these problems the systematic errors in the measurement of R by the MAC group at PEP[2] are summarized in Table II. MAC measures $R(Q^2 = 841\ GeV^2) = 3.96 \pm 0.03 \pm 0.09$. This is typical of the precision and systematic limitations encountered by the PEP and PETRA groups. For comparison $R_{QPM} = 3.67$.

Table II

Contribution	Error(%)
Event Selection	0.36
Acceptance:	
Detector Model	1.0
QCD+Frag.	0.5
Radiative Corr(α^3)	1.0
Backgrounds	0.76
Luminosity	1.6
TOTAL	2.3

All the individual groups have labored long and hard to reduce the systematic errors, but the limitations now seem intrinsic and no significant improvement seems possible in the near future. The QED radiative corrections are included up to third order in α. The corrections to the Bhabha normalization events and the multi-hadron events cancel to some extent in the ratio R. However, it has been

estimated that a residual higher order correction (α^4) could be at the 1% level. We will discuss the resulting effect on α_s below. As a contrast to the fixed energy ($E_{cm} = 29$ GeV) measurements of MAC, Fig. 2 shows the measurements of two of the PETRA groups in the energy range from 22-36 GeV. The errors include the statistics plus the point-to-point systematic uncertainty. The TASSO data also indicate the overall normalization uncertainty. The lower curve is for the QPM model, the upper curves the prediction of QCD. The upturn of the QCD curves arises from the fact that besides the $e^+e^- \rightarrow \gamma \rightarrow$ hadrons production process one must also include the interference from the weak production $e^+e^- \rightarrow Z^o \rightarrow$ hadrons. As with the MAC data, the conclusions are clear. The data favor the QCD prediction over the QPM but the errors make this statistically relatively weak and preclude an accurate determination of α_s via formula 1.

Recently the CELLO group at PETRA[3] have done a slightly more systematic extraction of R using an error analysis technique which attempts to handle the point-to-point errors and the overall errors in a rigorous way. Their data is shown in Fig. 3, where as outlined before, the QCD fit contains the effect of the interference term arising from Z^o exchange. From their data CELLO obtains:

(a) $\alpha_s(Q^2 = 1156\ GeV^2) = 0.19 \pm 0.05$

$sin^2\theta_W = 0.20 \pm 0.03$

and fixing $sin^2\theta_W = 0.23$,

(b) $\alpha_s(Q^2 = 1156\ GeV^2) = 0.16 \pm 0.05$.

The χ^2 for the fit to (a) is 3 for 7 degrees of freedom. In order to improve the error on α_s, CELLO has used the same procedure to fit the data[4] from the MAC, PLUTO, CELLO, JADE, MARK J and TASSO experiments (Fig. 4) to obtain R and find

(a) $\alpha_s(Q^2 = 1156\ GeV^2) = 0.165 \pm 0.04$

$sin^2\theta_W = 0.236 \pm 0.020$

and fixing $sin^2\theta_W = 0.23$,

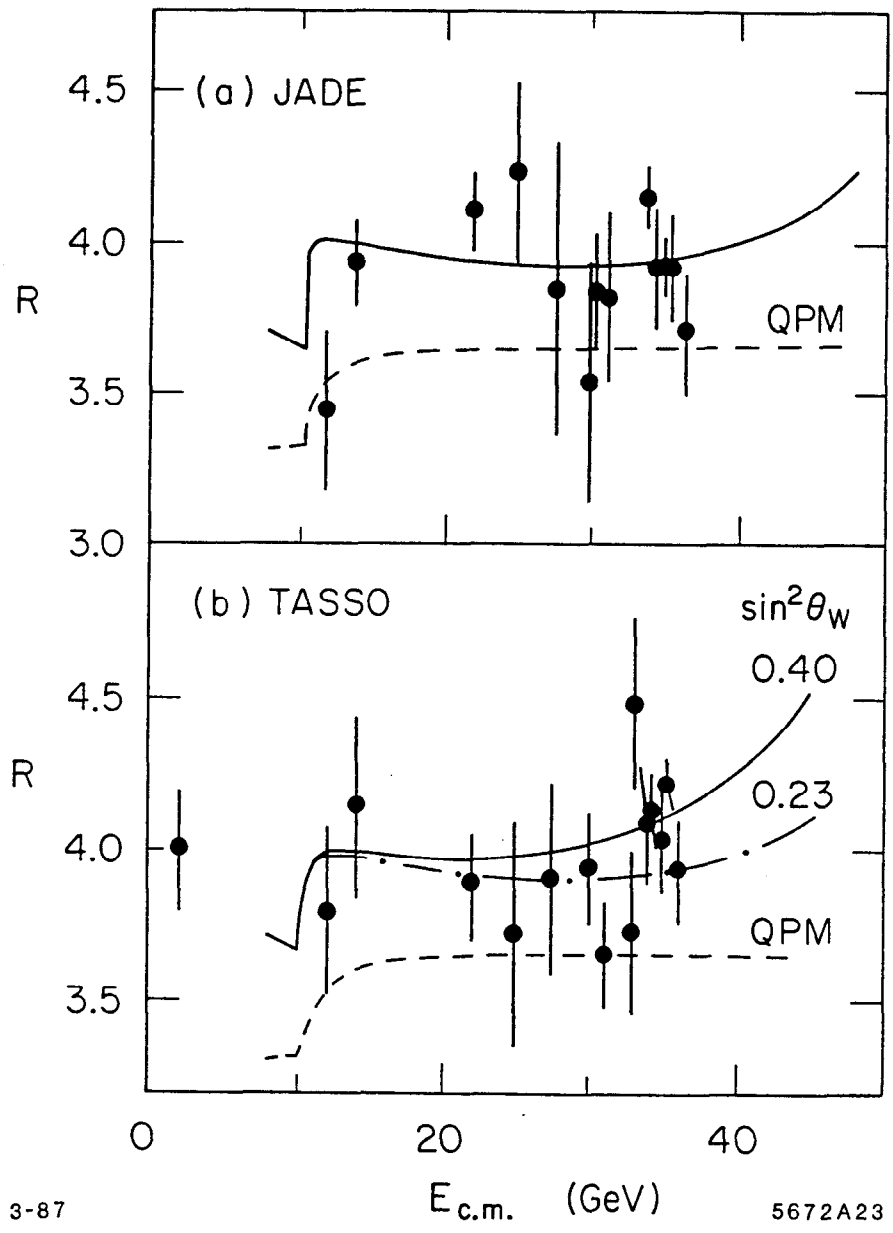

Fig. 2. Measurements of R = σ hadrons/$\sigma_{\mu^+\mu^-}$ as a function of E_{cm} from JADE(a) and TASSO(b). The expectation of the QPM is shown as well as for QCD including electroweak effects.

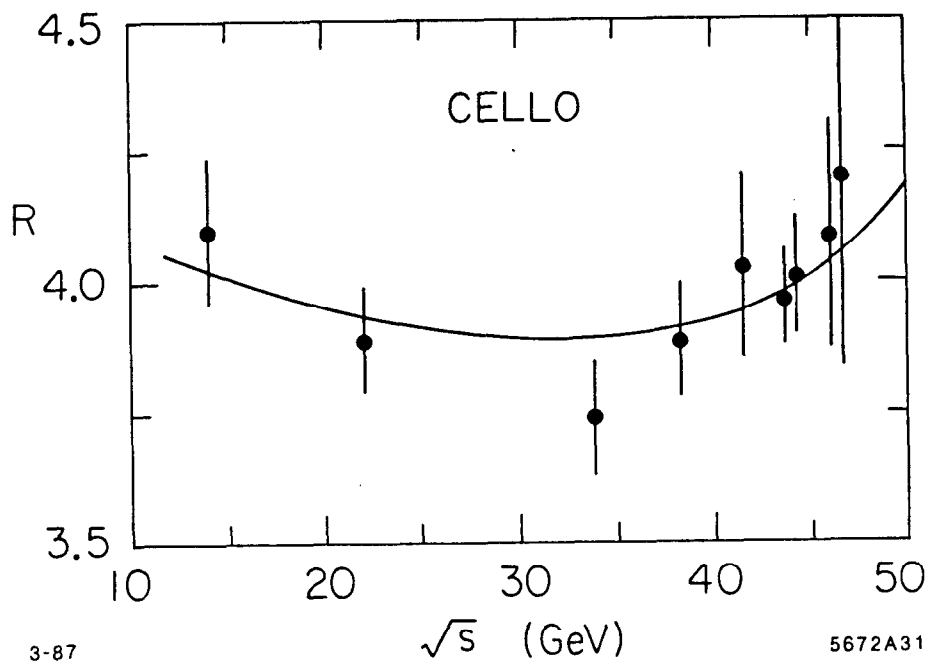

Fig. 3. Data on R from the CELLO group. Also indicated are the expectations from QPM, QCD and the electroweak interference.

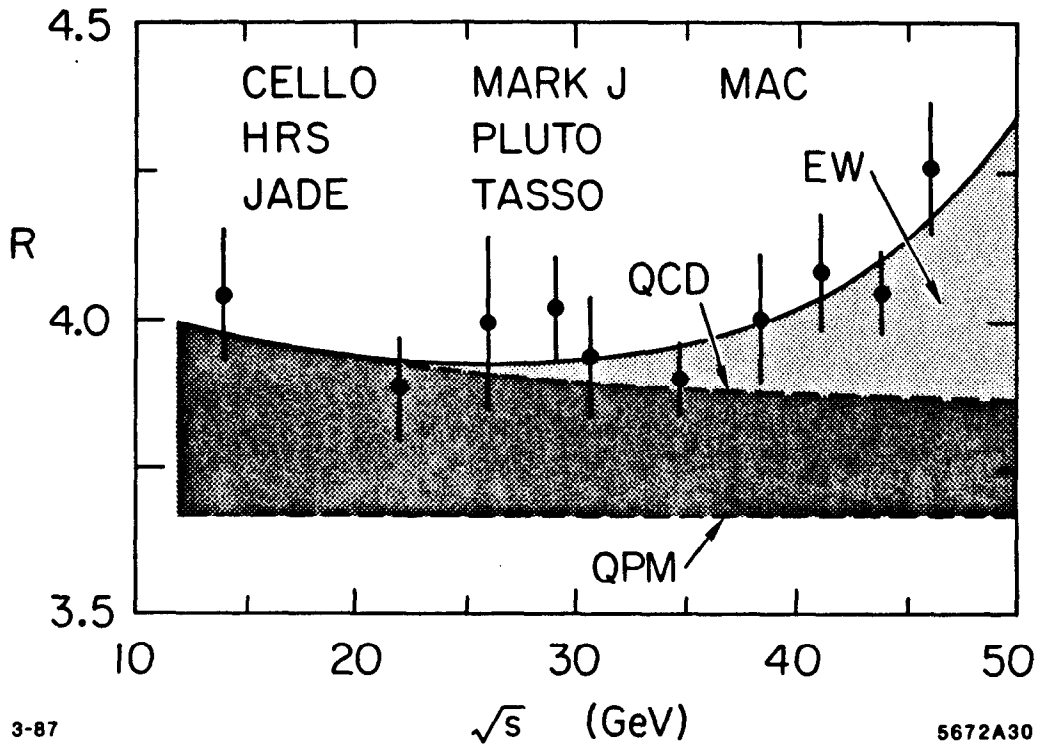

Fig. 4. Same as for Figure 3 except all the data from the experiments indicated are combined together (see Ref. 3).

(b) $\alpha_s(Q^2 = 1156\ GeV^2) = 0.169 \pm 0.025$.

As noted by CELLO, a 1% change in the QED radiative corrections due to higher orders would yield $\alpha_s = 0.145 \pm 0.024$ which implies a potential systematic error from this source comparable to the experimental errors.

I would conclude the R measurement discussion as follows:

1. The data do consistently support a value of R in good agreement with QCD and always larger than QPM. Individual experiments have a difficult time making a meaningful measurement of α_s.

2. If one accepts the inherent jeopardy of combining experiments (their acceptance and radiation correction software are not entirely independent) then a meaningful measurement of α_s results. With the possible exception of having $0(\alpha^4)$ QED correction calculations, we have probably reached the systematic limit of the measurement in this Q^2 range.

3. Although trivial by now, it is worth remembering that from R we clearly see that quarks come in three colors. The QPM and QCD curves shown here all assume three colors. For this non-trivial test of QCD, R is a powerful measurement.

2.2 Qualitative Tests Using Shape Parameters

We now return to the Q^2 dependance of the event shapes to get some more detailed qualitative and quantitative tests of QCD. We will discover that a very consistent picture evolves with QCD unfolded order by order with rather impressive qualitative agreement.

There are many shape parameters and each of the groups uses its favorite one. I will not attempt to illustrate all effects with each variable. Suffice it to say that the conclusions are independent of the shape parameter/procedure used. In addition, I will not explain each shape parameter formalism but rather will refer the interested reader to the excellent review of Sau Lan Wu.[5] In fact, all

the data in this section can be found in Ref. 5 with a more complete discussion and complete experimental references. The most familiar shape parameter used is sphericity. The sphericity axis is the symmetry axis which is chosen such that the sum of the transverse momentum squared of all tracks measured with respect to that axis is minimized. For i detected particles each with momentum p^i and momentum transverse to the event axis P_t^i the quantity S is defined as

$$S = 3/2 \frac{\sum_i (P_t^i)^2}{\sum_i (P^i)^2}. \tag{2}$$

The event axis becomes the sphericity axis and S the sphericity when (2) is minimized. So, spherical events have S$\rightarrow$ 1, while 2-jet, cigar shaped events have S$\rightarrow$ 0. In the sphericity analysis one can define an event plane which is the plane which contains the sphericity axis and has a normal for which the sum of the particle momenta, projected along this normal, are a minimum. As mentioned above the rigorous, mathematical derivation of the momentum tensor/sphericity technique is covered in Ref. 5.

All the analyses discussed in this section involve selecting events of the form $e^+e^- \rightarrow$ hadrons. I will not discuss in detail how this is done for each experiment. It is sufficient to point out that these events can be isolated with high efficiency and low backgrounds. The systematics of this selection process will have no significant effect on any of the conclusions drawn from the analyses. The features most commonly used are large multiplicity ($\geq$ 5 is typical, thus removing backgrounds from leptonic pair production) and relatively large detected energy ($\geq$ 0.25 E_{cm} to remove backgrounds from two photon processes). Typical efficiencies for these cuts are $\geq$ 70% with background contamination of $\leq$ 2%.

The phenomena of jet production in e^+e^- annihilation was first discovered at SPEAR by the MARK I collaboration[6] by observing the decrease in the sphericity with increasing E_{cm} in the range 3-7.4 GeV. In addition, the underlying jet axis was seen to follow a $(1+\alpha cos^2\theta)$ distribution with $\alpha = 0.78 \pm 0.12$. The 2-jet structure becomes much more apparent at higher energies; at 14 GeV the

PETRA hadronic events are dominated by clearly visible back-to-back jets. The sphericity axis shows a $1+cos^2\theta$ distribution characteristic of spin-$\frac{1}{2}$ constituents. (Spin 0 constituents would give a $sin^2\theta$ angular distribution.) The decrease in sphericity with increasing E_{cm} is shown for the SPEAR and PETRA (TASSO) data in Fig. 5 while the angular distribution of the sphericity axis at $E_{cm} = 34$ GeV is shown in Fig. 6.

At this level of magnification ($Q^2 \leq 200GeV^2$) we see that spin-$\frac{1}{2}$ constituents are clearly being produced consistent with the QPM and QCD. To differentiate between these two options we need to raise Q^2 and look for gluon radiation as shown in Fig. 1(b). For the topology of a hard gluon bremsstrahlung off the q(or$\bar{q}$), coplanar 3-jet events should be seen. This is exactly what is seen both at PETRA and PEP. Each group uses its own analysis technique to demonstrate the presence of 3-jet events and quantify the agreement with QCD (see Ref. 5). Irrespective of the method, QCD does an excellent job of accounting for the observed distributions via the inclusion of the tree level branching diagram (Fig. 1(b)). Examples of clear 3-jet topologies are shown in Fig. 7.

To see the onset of the gluon radiation I show data from TASSO and MARK J. (The other PETRA experiments come to identical conclusions.) TASSO uses the sphericity analysis. Shown in Fig. 8 are the average $< P_t^2 >_{out}$, $< P_t^2 >_{in}$ for particles in hadronic events where *in* and *out* refer to the momentum component directions with respect to the sphericity event plane. What one sees is that in going from low center-of-mass energies (2-jet dominated) to higher center-of-mass energies, the $< P_t^2 >_{out}$ does not change but the $< P_t^2 >_{in}$ changes significantly. The distribution of particle momenta in the event plane relative to the sphericity axis have developed a "long tail." This tail cannot be accounted for by assuming a 2-jet model in which the typical transverse momentum in the jet fragmentation (σ_q) grows with E_{cm}. Such a model does not fit the data. One reproduces the distributions in Fig. 8 very well with first order QCD which produces planar 3-jet events which do not add to the $< P_t^2 >_{out}$ but will broaden the P_t distribution in the event plane. The exact same conclusions can be drawn from the MARK J data

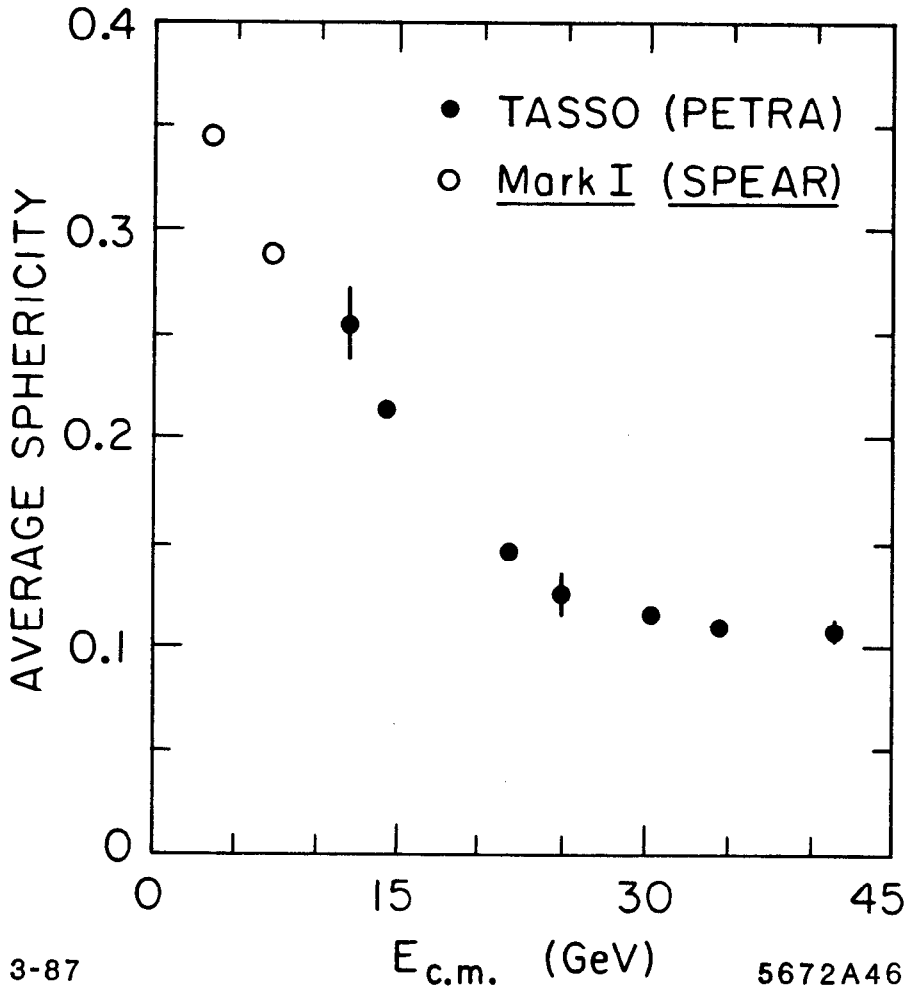

Fig. 5. The average sphericity in hadronic events for data from SPEAR (Mark I) and PETRA (TASSO). The reduction of $< S >$ with increasing energy clearly indicates the increasing domination of 2-jet events.

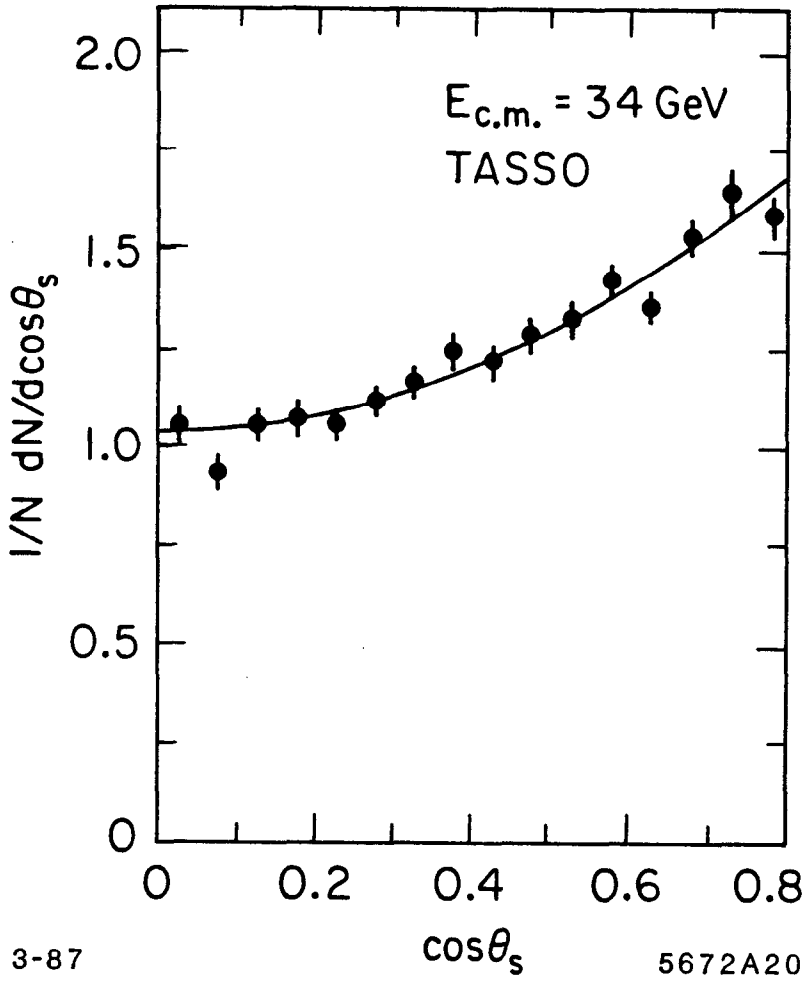

Fig. 6. The production angular distribution for the jet axes as reconstructed using the sphericity axis. The curve shows the expectation for spin-$\frac{1}{2}$ constituents, namely a $(1 + \cos^2\theta_s)$ distribution.

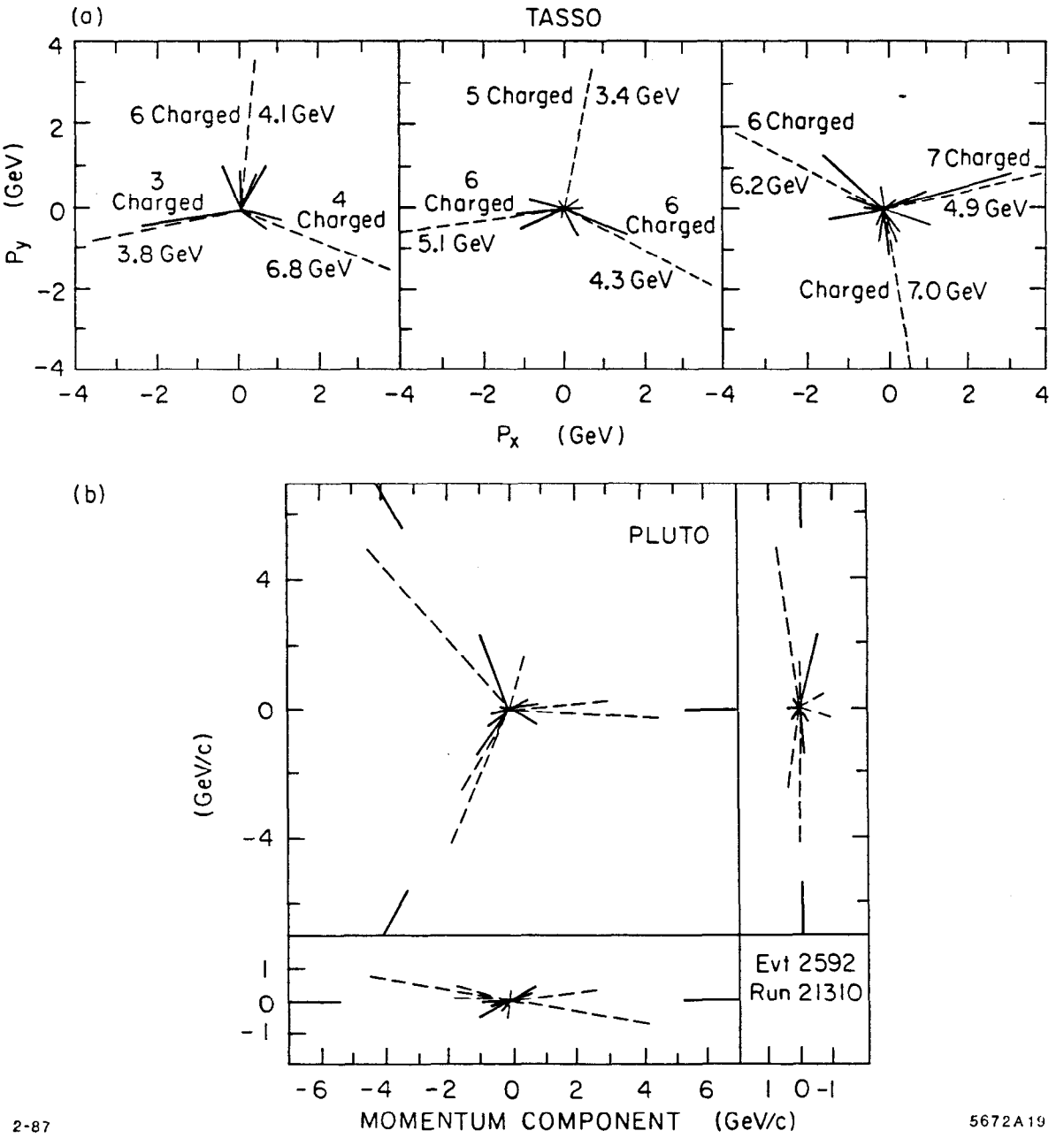

Fig. 7. Examples of 3-jet events at PETRA.

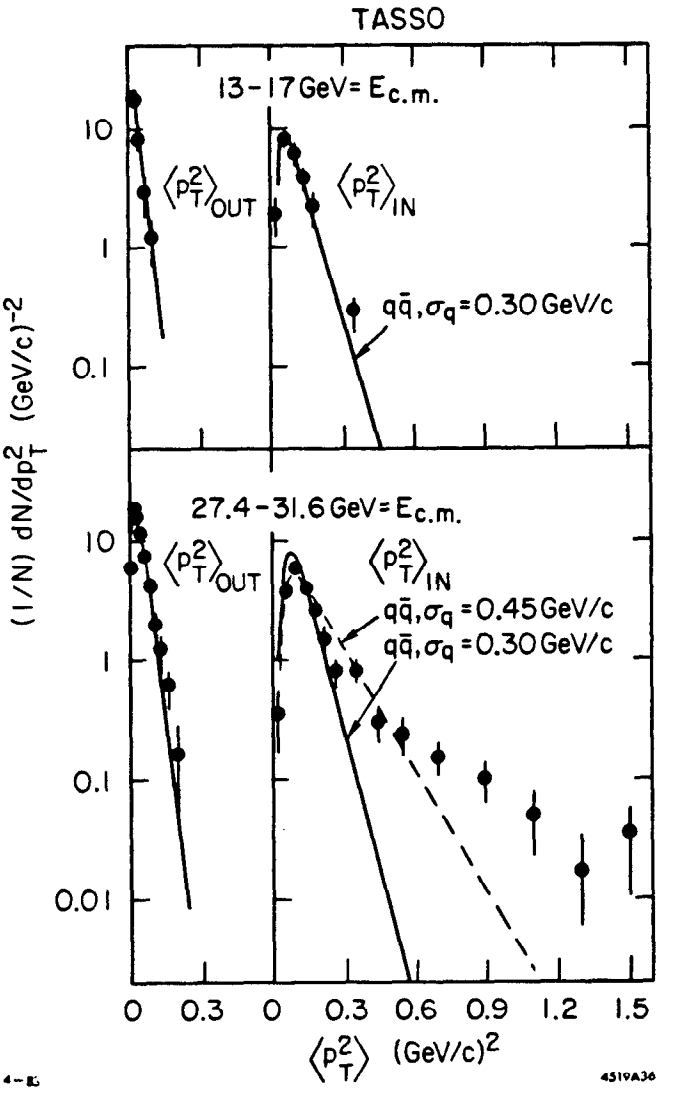

Fig. 8. The growth of the momentum in the event plane as a function of increasing center-of-mass energy is shown. The corresponding momentum component normal to the event plane shows very little growth. The curves are the predictions of 2-jet models in which σ_q represents the mean transverse momentum which characterizes the quark fragmentation. The growth in $< P_T^2 >$ cannot be explained by such a model. This growth arises because of the presence of 3-parton events of the type $q\bar{q}g$.

(Fig. 9) where the shape variable oblateness is used. Again, simple extensions of 2-jet models do not account for the data, while first order QCD does an excellent job. So the conclusion is clear: the change in event shapes is going from $E_{cm} \simeq 17$ GeV to $E_{cm} \simeq 35$ GeV cannot be fit by a 2-jet hypothesis. These changes look qualitatively like those which are generated by a bremsstrahlung type process $(1/k^2)$. First order QCD does a good job of reproducing the observed effects.

Further qualitative examples of QCD tests in this energy range involve testing the QCD predictions for the Dalitz plot distributions for 3 parton (jet) final states. First order QCD predicts

$$\frac{1}{\sigma_o dx_1 dx_2} = \frac{2\alpha_s}{\pi}\{\frac{x_1^2 + x_2^2}{(1-x_1)(1-x_2)}\} + 1,2,3 \; cyclic \; permutations \qquad (3)$$

where $x_i = 2E_i/E_{cm}$ and E_i = parton energies. To check these predictions requires reconstructing 3-jet events. Again there are several methods used – triplicity, trijettiness, cluster finding (see Ref. 5). The details of these methods are not important here, the conclusions are independent of the method. Each method chooses a sample of 3-jet events in which each particle is assigned to one of the 3 jets (see Fig.10). The jet directions are calculated from the momentum vectors of the particles assigned to the jets. The jet energies are then calculated from the jet directions assuming the partons are massless. The jet energies are ordered such that $x_1 > x_2 > x_3$. With a sample of 3-jets so selected, one can test QCD via the Dalitz plot distributions characterized by (3). The differential distribution dn/dx_1 is shown in Figs. 11 and 12 for CELLO and JADE data along with the predictions of QCD. CELLO shows curves for first order QCD using a vector gluon and first order QCD using a scalar gluon. Clearly the vector gluon is preferred and QCD does an excellent job of reproducing the data. JADE shows the prediction of both first and second order QCD. Again, QCD reproduces the data well. The TASSO group uses a slightly different variable to test the QCD matrix element. They transform the 3-jet events (along the axis x_1) into the rest frame of x_2 and x_3. They then look at the decay angular distribution of the x_2^*

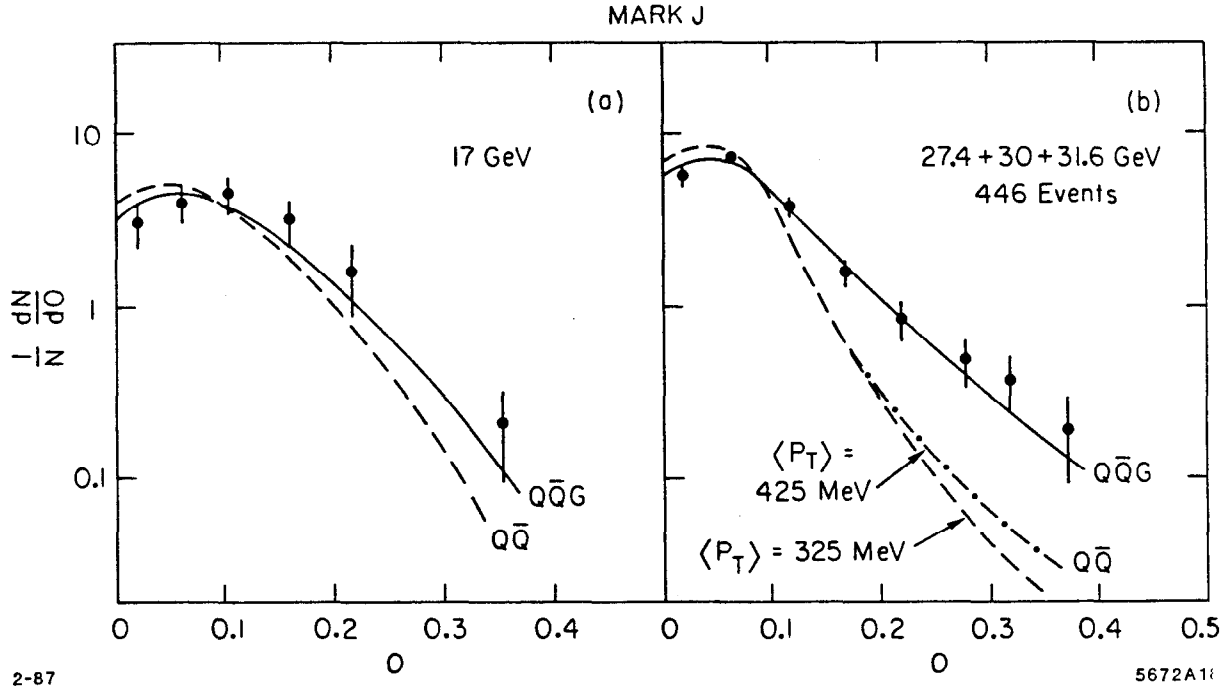

Fig. 9. The onset of 3-jet events seen in Fig. 8 is illustrated here using the variable oblateness. Again 2-jet models cannot account for the data. The predictions of first order QCD ($Q\bar{Q}G$) are explicitly shown and account well for the data.

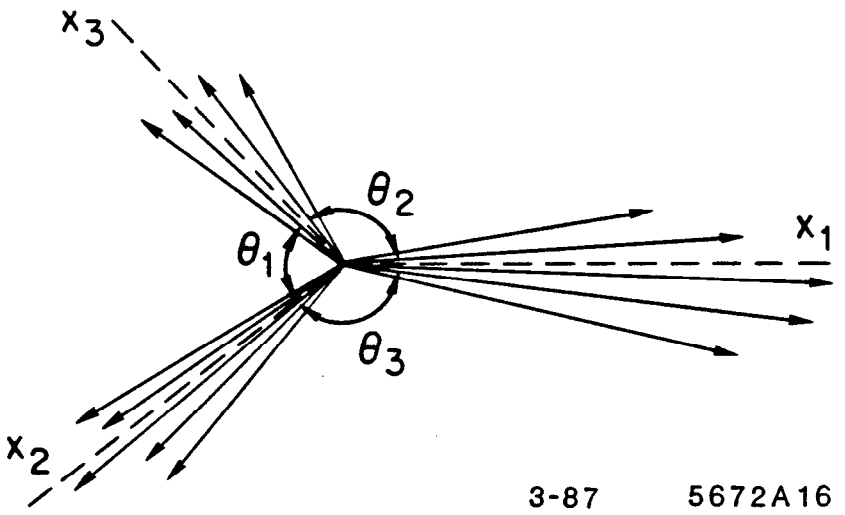

Fig. 10. Parameters of an idealized 3-jet event are shown where the arrows represent the particle momenta. The fractional energy of each jet is $x_i = 2E_i/E_{cm}$ and θ_i is the angle opposite the jet x_i.

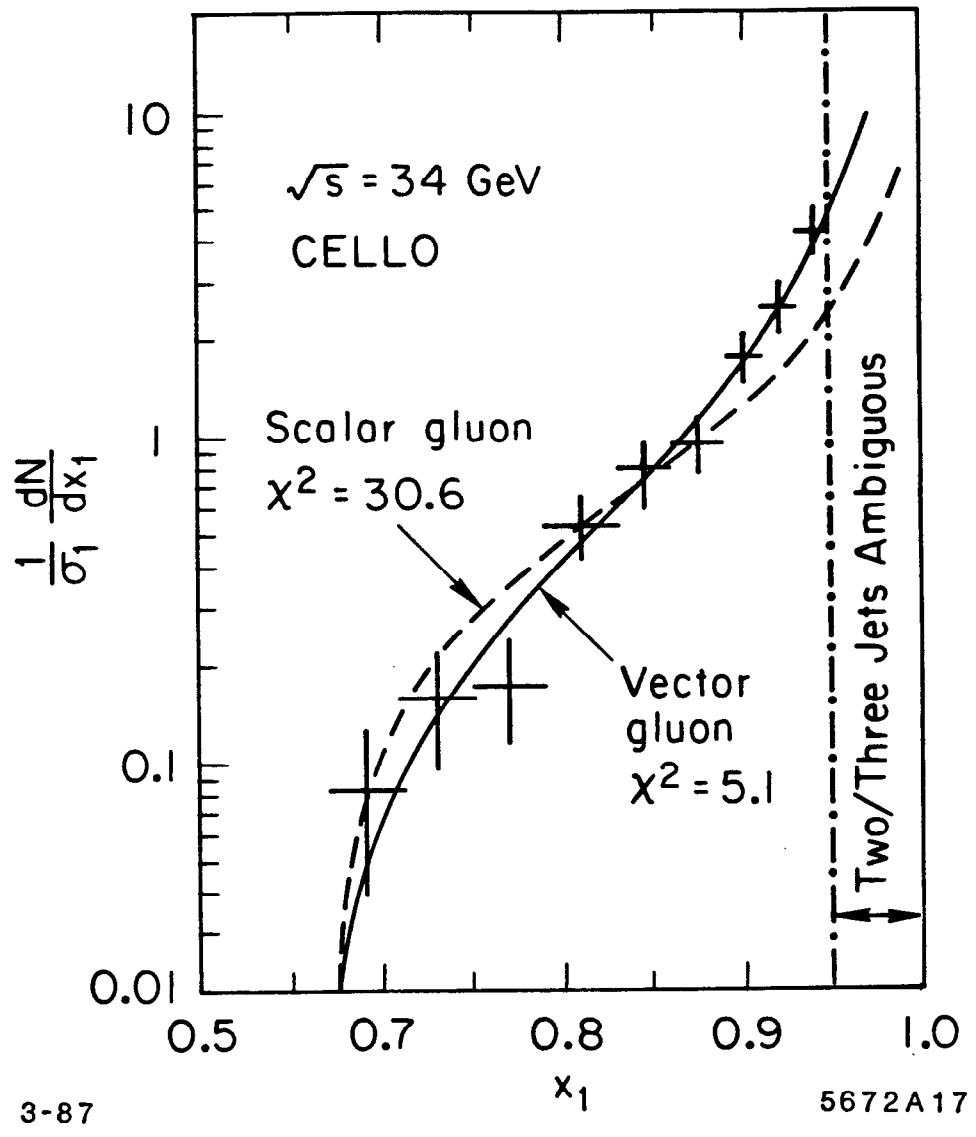

Fig. 11. The distribution of the fractional momentum of the highest energy jet in 3-jet events is shown at E_{cm}= 34 GeV (CELLO data). A cut at x_i <0.9 is made to select clear 3-jet topologies. QCD (solid line) gives a good representation of the data while QCD with a scaler gluon does not.

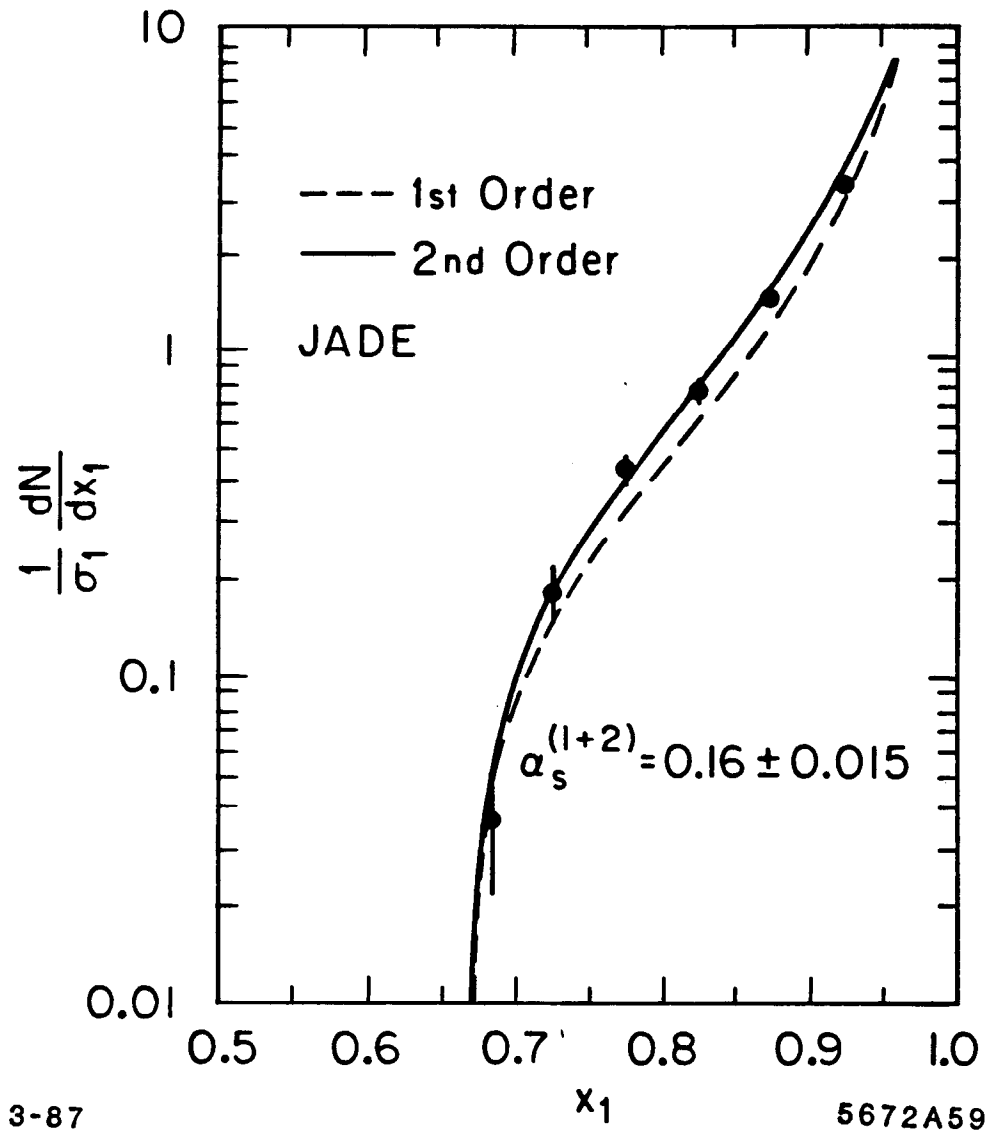

Fig. 12. The distribution of the fractional momentum of the highest energy jet in 3-jet events is shown (JADE data). The predictions of first and second order QCD are indicated. The second order prediction is a better representation of the data.

(x_3^*) parton (see Fig. 13). One finds that this angle, $\tilde{\theta}$, is related to the x_i's via

$$cos\tilde{\theta} = \frac{x_2 - x_3}{x_1}.$$

The distribution of $cos\tilde{\theta}$ is shown in Fig. 14 with the QCD predictions for scalar and vector gluons. Again the scalar hypothesis is ruled out; the vector hypothesis gives a good description of the data.

At energies above 30 GeV at PETRA one sees direct evidence for 4-jet events – hence unfurling yet another order in QCD. Data from the JADE group (Fig. 15) show that a better accounting of the multijet topologies is obtained (L234 rather than L23) when a statistically significant 4-jet piece is added to the QCD cross section. From a fit to the 33 GeV data, JADE finds the percentage of 2, 3 and 4 cluster events to be 56.1±0.4%, 40.2±0.4% and 3.75±0.16%, respectively.

We can close this section by noting that the agreement between event distributions in high energy e^+e^- collisions and the predictions of QCD is non-trivial. There exists no other model which can reproduce all aspects of the data. Many other models have been tried – QPM (2-jet models) with a wide variety of quark fragmentation scenarios, fire string models, etc.[7] These other models can often be tuned to fit some aspects of the data, but never all aspects simultaneously. So if one asks, "Does the e^+e^- data require something beyond the QPM+ fragmentation," the answer is a definitive "yes." In addition, the qualitative features are well accounted for by QCD+fragmentation models, and there exists no other model which can claim such qualitative agreement with the data.

2.3 Quantitative Tests from Events Shapes

We turn our attention now to the question of how well one can extract α_s (or Λ) from the e^+e^- event shapes? It is well known that this has been an uphill struggle and perhaps, after many years of theoretical and experimental study and toil, a clearer picture has emerged. About two years ago most of

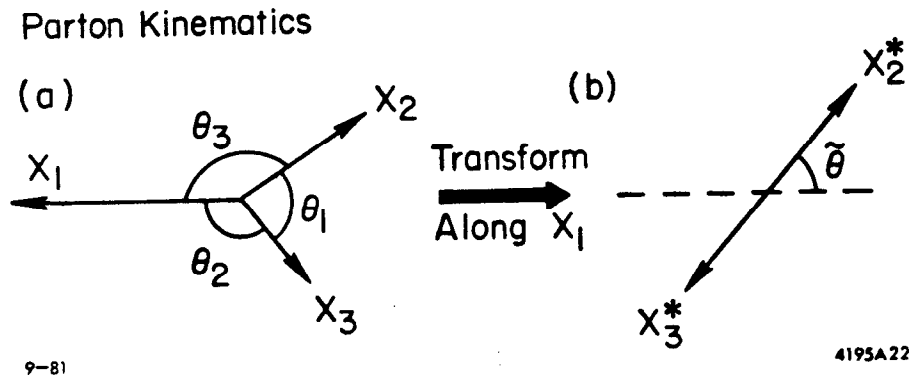

Fig. 13. (a) The kinematics for the process $e^+e^- \rightarrow q\tilde{q}g$ where $x_i = E_i/E_{cm}$ and E_i are the parton energies. (b) The definition of the Ellis-Karliner angle, $\tilde{\theta}$.

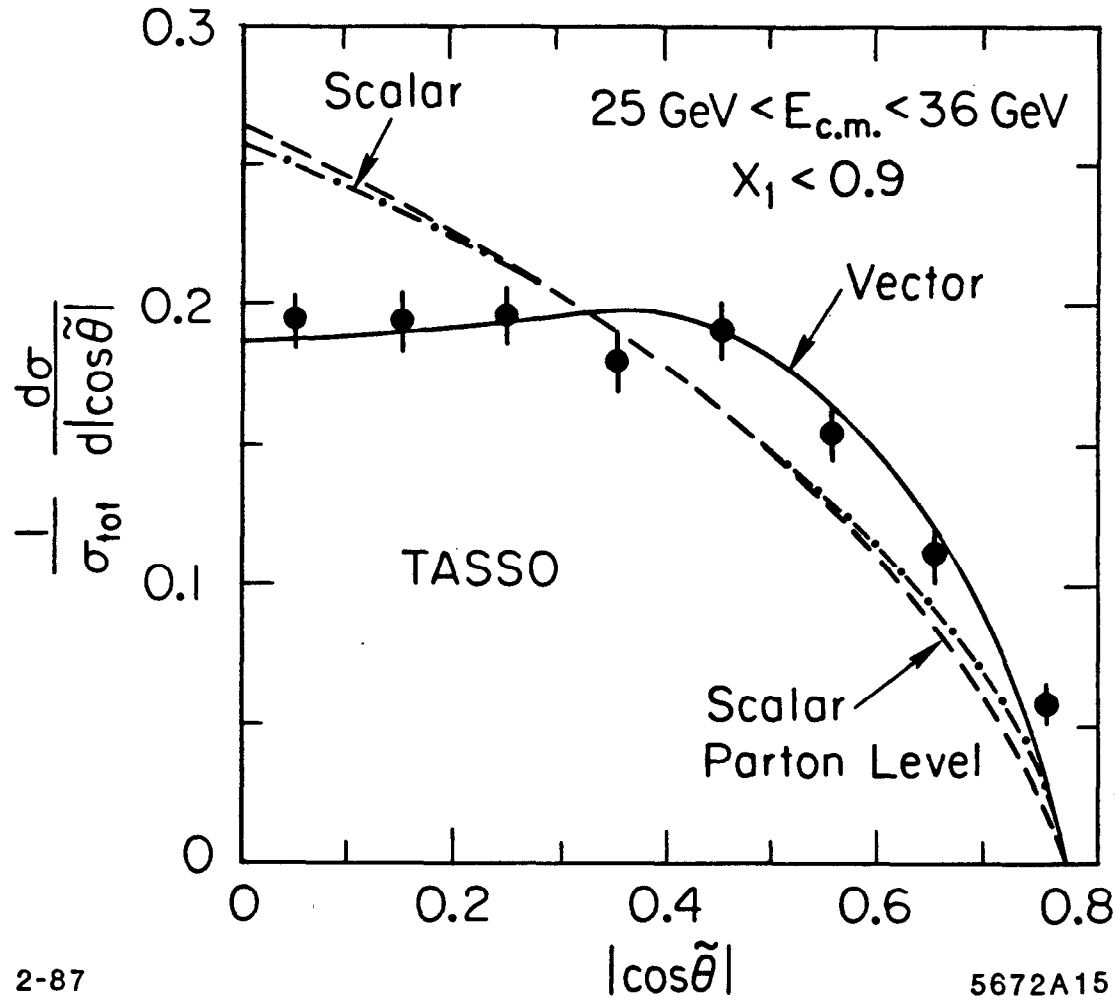

Fig. 14. The distribution of the Ellis-Karliner angle $\tilde{\theta}$, for the 3-jet events with $x_i < 0.9$ obtained by the TASSO group. The solid curve is QCD with $\alpha_s = 0.17$, the dashed curve is the prediction for a scaler gluon.

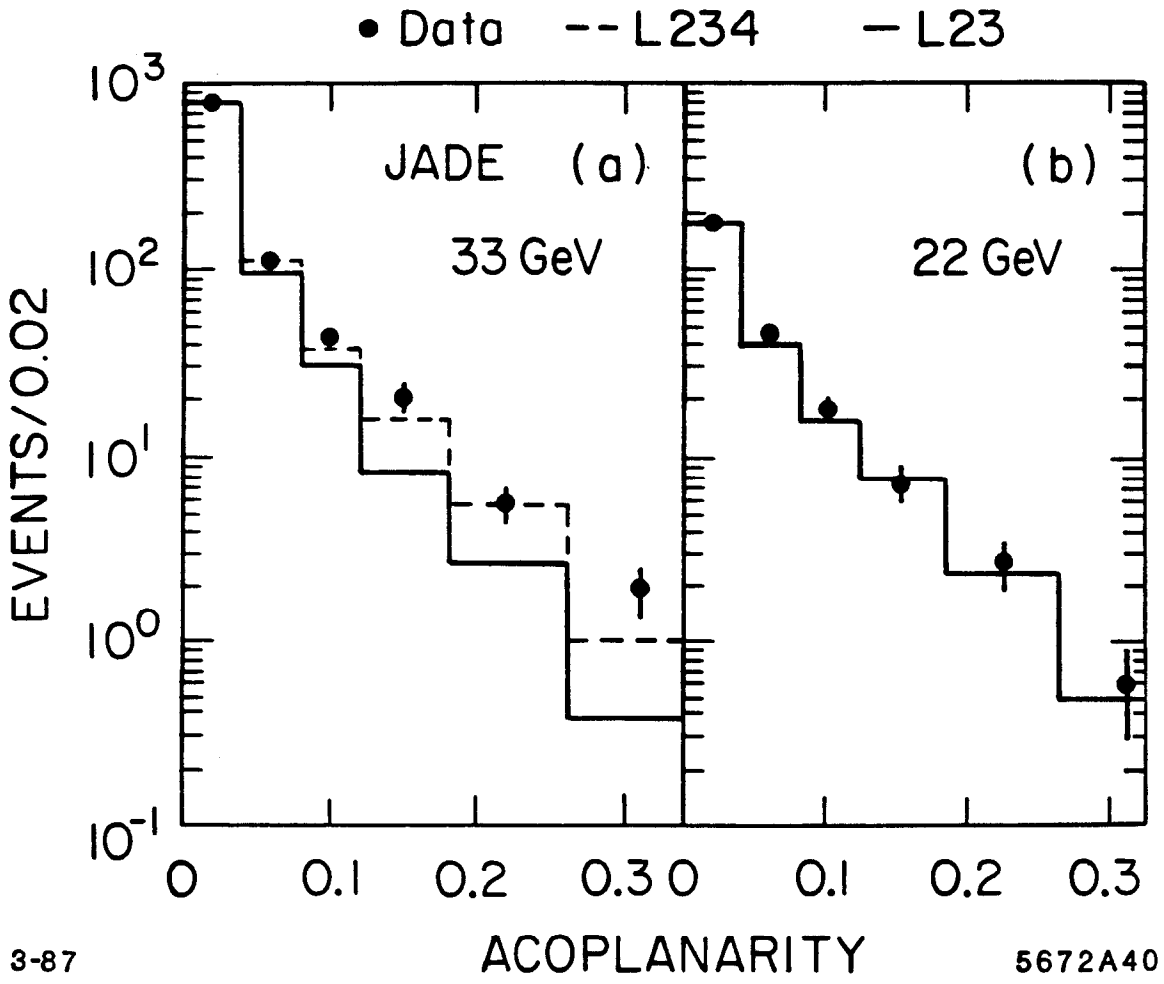

Fig. 15. Data from JADE which show that at lower energies ($E_{cm} \approx 17$ GeV) the aplanarity distribution is well fit by a QCD model with 2 and 3 parton states only (L23). At higher energies this is no longer true and 4 parton states (L234) need to be added to obtain a good fit to the data.

the experimental groups and reviewers characterized the α_s determinations from PETRA/PEP as dependent on fragmentation effects and the schemes used for implementing $O(\alpha_s^2)$ QCD.[8] But since then there have been some theoretical and experimental insights and more recent reviewers now feel that there is a reliable procedure which gives consistent results with significant precision. The favored procedure is the Energy–Energy Correlation Asymmetry with higher order QCD effects incorporated using the so-called ERT scheme. Where do the problems in measuring α_s arise?

The first problem is with the cutoff procedure required to distinguish different parton multiplicities. Roughly speaking, a measurement of α_s is a measurement of the ratio of the number of 3-jet events to 2-jet events. To do this one needs to specify both theoretically and experimentally what belongs to each class. When a gluon, in a qqg topology, is colinear with the quark (or antiquark) or has a vanishingly small momentum, this 3 parton topology becomes indistinguishable from the 2 parton topology. This creates an ambiguity about which parton topology the event belongs to. To avoid this problem a cutoff procedure is established which defines clearly how to resolve these ambiguous topologies. Problems arise when the α_s extracted from the data is sensitive to the cutoff procedure.

Two cutoff methods are used: a) Sterman-Weinberg (ϵ, δ) and b) parton invariant mass (y_{min}). Two partons are considered resolvable if:

(a) Sterman-Weinberg: The energies of both partons are $> \epsilon E_{cm}/2$ and the partons are separated by an angle greater than δ.

(b) Parton invariant mass: For parton momenta P_i and P_j $(P_i + P_j)^2 > y_{min} E_{cm}^2$.

For $O(\alpha_s^2)$ tests we have to include the graphs shown in Fig. 16 and hence we must use the cutoff procedure to partition the events into 2, 3 and 4 parton states. These $O(\alpha_s^2)$ diagrams were originally calculated by three groups:

1. Ellis, Ross and Terano (ERT).[9]

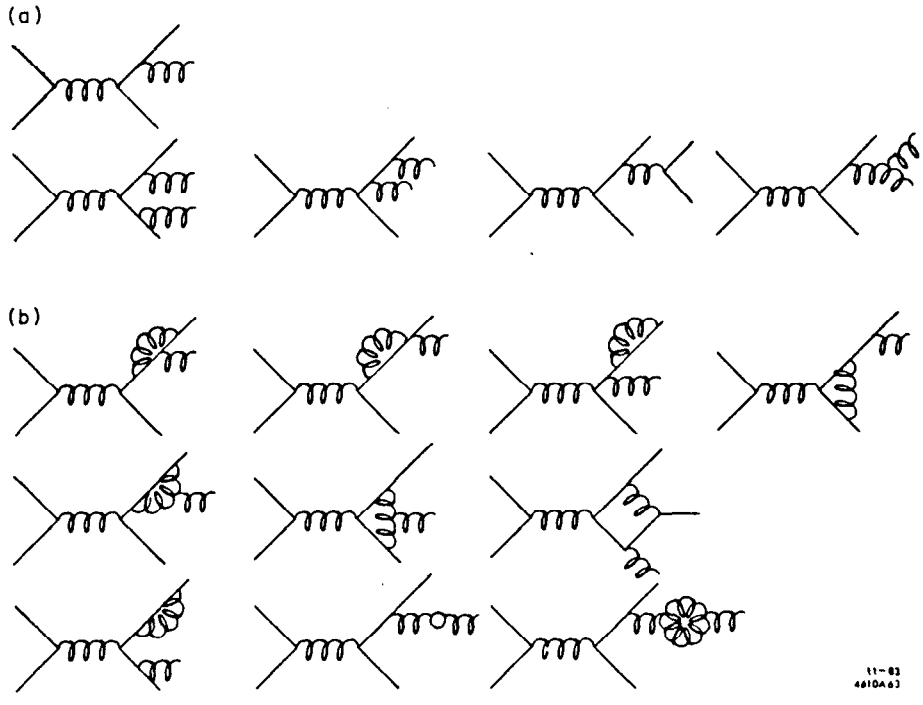

Fig. 16. (a) Tree level diagrams for 3 and 4 parton final states and (b) second order virtual parton contributions.

2. Vermasseren, Gaemers and Oldham (VGO).[10]

3. Fabricius, Kramer, Schierholz and Schmitt (FKSS).[11]

Methods 1) and 2) are exact and are calculated at the bare parton level while 3) is approximate incorporating jet resolution implicitly. Methods 1) and 3) have been widely used at PETRA. As discussed later, an improved version of FKSS was implemented.[12] We refer to it here as the extended FKSS or FKSS'.

A second problem with α_s determinations arises from the fact that QCD makes calculations at the parton level and experimentalists make measurements at the hadron level. To relate experiment to theory inevitably involves a model of perturbative QCD+fragmentation. This leads to the important question about biases which result from the use of these models. For some choices of variables the fragmentation effects mask the perturbative effect which one is trying to measure. With each procedure care must be taken to investigate the effect of hadronization on the ability to extract α_s.

There have been many methods used at PETRA and PEP to measure α_s. Physicists have argued (still do) at great length about which methods are the most reliable. Most methods have significant problems – the principle one being sensitivity to fragmentation. The sceptic should look at all these methods; however, many now seem to agree that the analysis method of choice is the Energy–Energy Correlation Asymmetry (EECA). The main reasons are:

1. The EECA behaves better in second order perturbative theory than any other variable studied (i.e. $0(\alpha_s^2)$ corrections are small).

2. It is infrared stable and, hence, relatively insensitive to the choice of cutoff parameters.

3. For $E_{cm} \geq 30$ GeV fragmentation effects from $q\bar{q}$ are small. (However fragmentation effects from $q\bar{q}g$ are still significant.)

Table III summarizes the sensitivity of some commonly used variables to the inclusion of $0(\alpha_s^2)$ terms.[13] (Taken from Ref. 13 using ERT matrix elements.) The smaller the K factor the smaller the $0(\alpha_s^2)$ corrections.

Table III

VARIABLE	INTEGRATION RANGE	K = $0(\alpha_s^2)/0(\alpha_s)$
Thrust	T < 0.85	18.9
Oblateness	0 > 0.30	3.5
EEC	$\mid cos\chi \mid <$ 0.75	12.3
EECA	$\mid cos\chi \mid <$ 0.75	3.1

The Energy–Energy Correlation[14] involves using hadronic events to study the energy weighted cross section

$$\frac{1}{\sigma}\frac{d\Sigma}{dcos\chi} = \frac{1}{N}\frac{1}{\Delta(cos\chi)}\sum_N\sum_{i,j}\frac{E_iE_j}{E_{VIS}^2}\delta(cos\chi_{ij} - cos\chi)$$

where the sum ranges over all N events including all particles pairs i and j with energies E_i and E_j, and E_{VIS} is the detected energy in the event. The particles i and j are separated by the angle χ_{ij}. In the absence of any transverse momentum in the fragmentation, 2-jet events will give rise to peaks at $cos\chi = \pm 1.0$. The presence of this hadron P_t will provide correlations at other values of $cos\chi$. Gluon emission will contribute an asymmetry to the energy-energy correlation. To isolate such an emission one studies the asymmetry (EECA)

$$A(cos\chi) = \frac{1}{\sigma}\left\{\frac{d\Sigma}{dcos\chi}(\pi - \chi) - \frac{d\Sigma}{dcos\chi}(\chi)\right\}.$$

When using $A(cos\chi)$ to extract α_s it is customary to exclude the forward and backward regions which tend to be strongly influenced by quark fragmentation effects. Typically the region for $\mid cos\chi \mid > 0.75$ is excluded. Table IV shows a

compilation of α_s measurements made using EECA indicating the method used for implementing the $0(\alpha_s^2)$ QCD and the sensitivity of the measurement to the non-perturbative models, SF and IF. The SF and IF models stand for string fragmentation (LUND-type model)[15] and independent fragmentation (Ali et al.[16] or Hoyer et al.[17] type models), respectively. The data came from TASSO,[18] CELLO,[19] JADE,[20] PLUTO,[21] MARK J,[22] and MAC.[23] Looking at the table one sees several clear trends. Here α_s extracted using string fragmentation models is always larger than from independent fragmentation models. The same is true of FKSS (or extended FKSS) relative to ERT. As discussed in the TASSO paper by Gottschalk and Shatz[24] (in collaboration with Gutbrod and Shierholz) the FKSS scheme leads to α_s values which are 15-20% too large. The main contributions to this overestimate arise from the cutoff procedure used ($\approx$ 10%) and, neglecting terms of order ϵ and δ^2 (or y) ($\approx$ 10%). The extended FKSS scheme (FKSS′) inserts missing four parton states which reduces this latter problem by about a factor of 2. It appears as if the ERT scheme does not suffer the problems of the FKSS scheme and we should focus our attention then on the measurements obtained with this scheme.

Table IV

Group	Ref	Year	QCD	α_s(SF)	α_s(IF)
MARK J	22	83	ERT(ϵ, δ)	0.14	0.12
CELLO	19	83	FKSS(y)	0.19	0.15-0.13
JADE	20	84	FKSS(y)	0.165	0.14-0.11
TASSO	18	84	ERT(ϵ, δ)	0.159	0.127-0.117
TASSO	18	84	FKSS′(ϵ, δ)	0.19	0.157-0.139
PLUTO	21	85	ERT(ϵ, δ)	0.145	0.136
MAC	23	85	FKSS(y)	0.185	0.14-0.11

Figures 17 and 18 show that the second order QCD corrections are under control for EECA measurements, namely that there is not a strong E_{cm} dependance. Also shown in Fig. 17 is the contribution to the EECA arising from $q\bar{q}$ fragmentation. Above E_{cm} = 30 GeV $q\bar{q}$ fragmentation has a negligible effect when a sensible $\mid cos\chi \mid$ cut is used. Figure 19 demonstrates the sensitivity of the EECA measurement with respect to variations in the cutoff parameter ϵ. Similar stability for the ERT scheme is obtained for reasonable variations of δ at fixed ϵ.

The data used for the α_s determinations using the EECA and ERT scheme are shown in Figs. 20 (PLUTO), 21 (TASSO), 22 and 23 (MARK J).[25] In all cases the limiting systematic error in α_s comes from the fragmentation models and is about 0.02. In all cases the Monte Carlo predictions for SF and IF agree well with the data. In fact for the MARK J and PLUTO data, the predictions of the models are indistinguishable in the plots. As discussed above, they agree, but with systematically different values of α_s. The results of these measurements are quoted as:

PLUTO(35 GeV)[21]:	$\Lambda_{\overline{MS}}$	=	112±23+25 MeV	(Fit to QCD)
		=	183±31 MeV	(IF) (α_s=0.136)
		=	259±40 MeV	(SF) (α_s=0.145)
TASSO(35 GeV)[18]:	α_s	=	(0.127-0.117)±0.01	(IF)
		=	0.159±0.012	(SF)
MARK J(44GeV)[25]:	$\Lambda_{\overline{MS}}$	=	$60\pm12^{+25}_{-20}$MeV	(IF)
		=	$150\pm30^{+50}_{-40}$ MeV	(SF)

or in summary:

	$\Lambda_{\overline{MS}}$	=	$100\pm30^{+60}_{-45}$
	α_s	=	0.12±0.02
MARK J(35GeV)[22]:	α_s	=	0.13±0.02

One may conclude from these measurements that in the 35-44 GeV region, α_s lies between 0.12-0.16 giving $\Lambda_{\overline{MS}}$ in the range of 100-300 MeV.

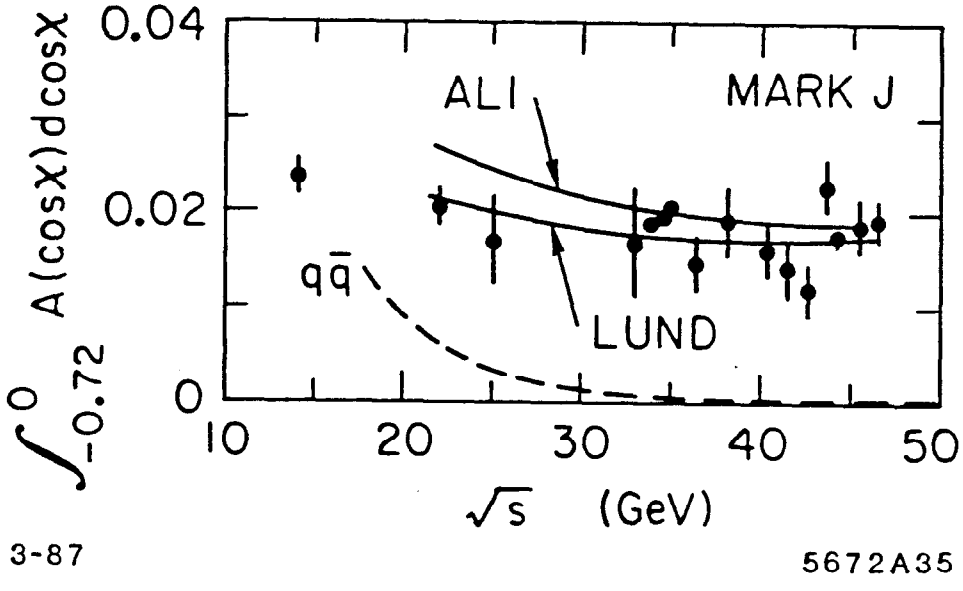

Fig. 17. The energy dependence of the integrated EECA is shown using MARK J data, along with the contribution from $q\bar{q}$ (dashed curve) and the prediction of the LUND and ALI Monte Carlo simulations.

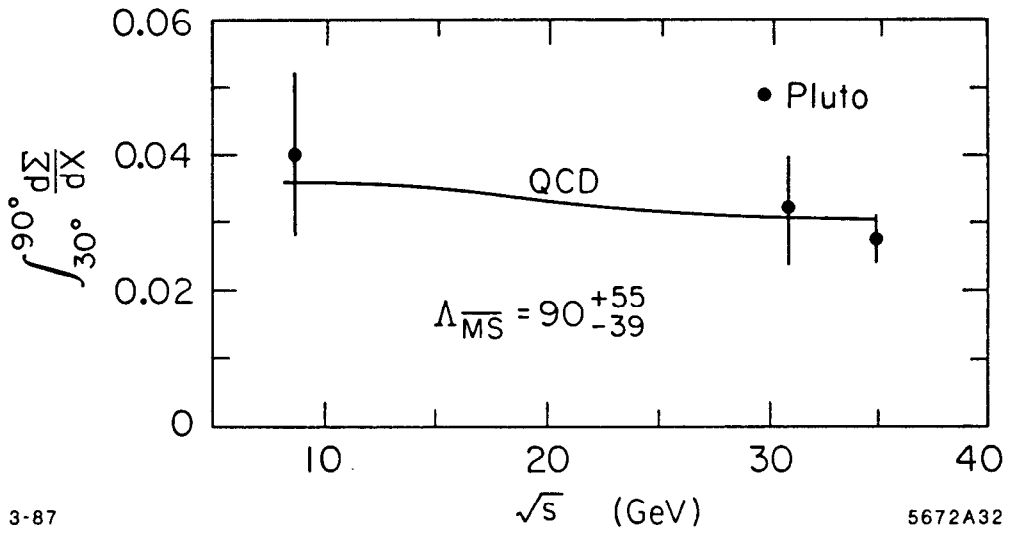

Fig. 18. The energy dependance of the integrated EECA is shown using the PLUTO data. Also shown is the prediction of QCD.

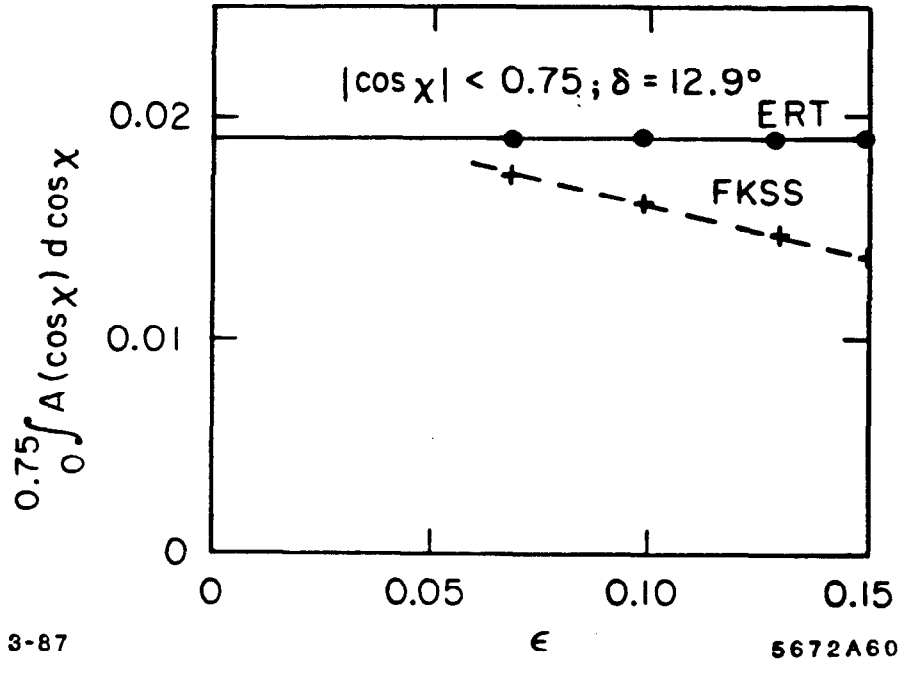

Fig. 19. Sensitivity of the integrated EECA to the cutoff parameter ϵ. Solid line is in the ERT scheme, dashed line the FKSS scheme.

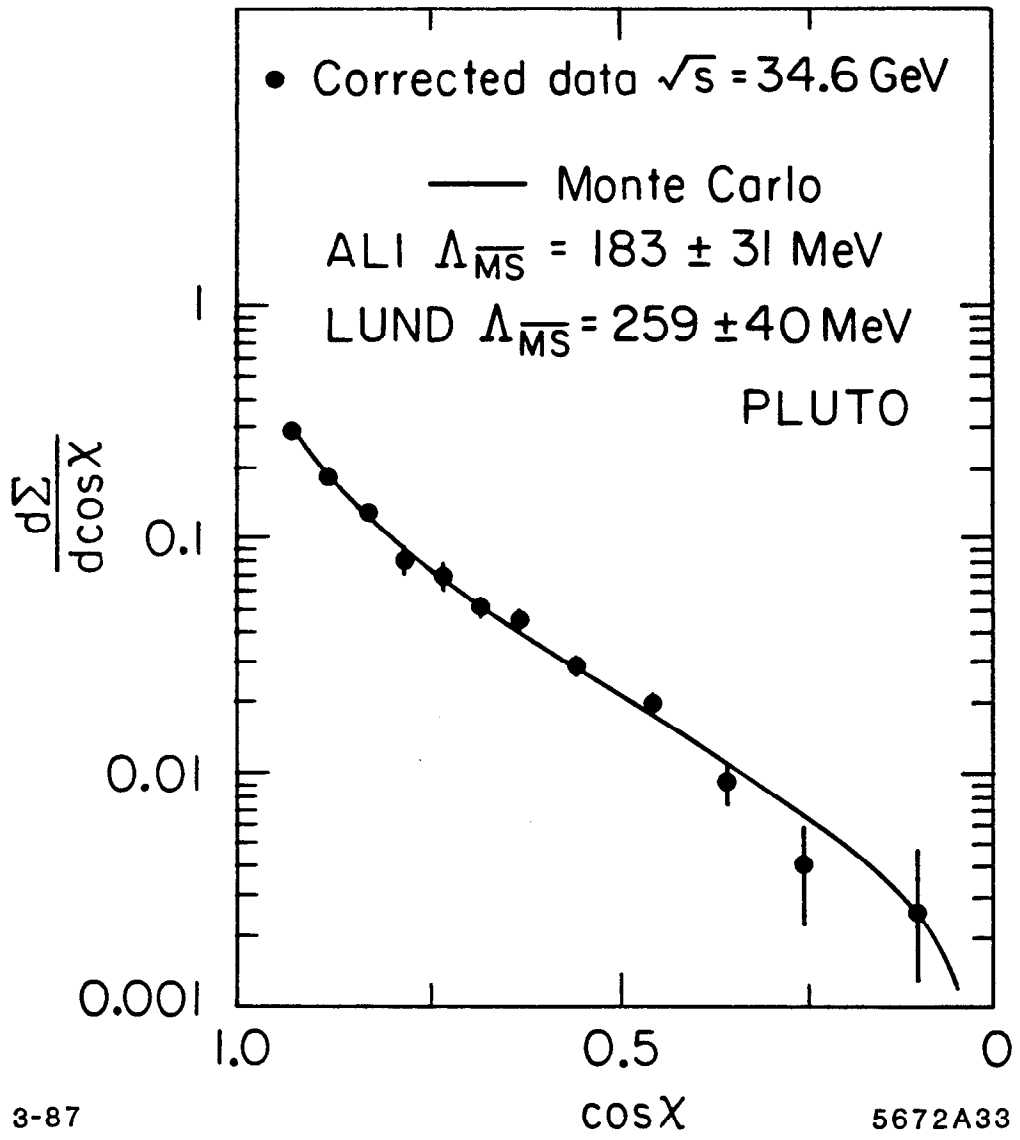

Fig. 20. The EECA as a function of $cos\chi$ as measured by PLUTO at E_{cm}= 34.6 GeV. The solid line is the fit to the LUND and ALI models.

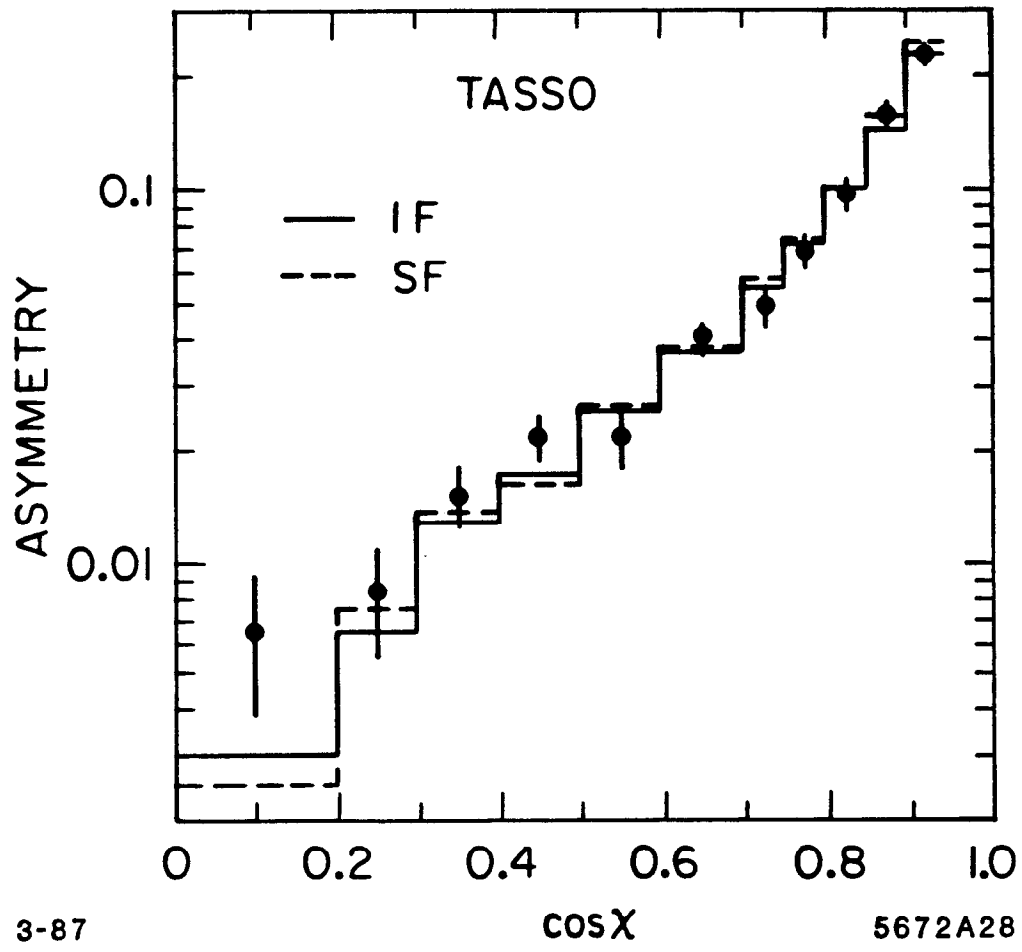

Fig. 21. The EECA as a function of $cos\chi$ as measured by TASSO at E_{cm}= 34.6 GeV. The solid (dashed) line is the prediction of the ALI (LUND) model fit to the data for $|\ cos\chi\ | < 0.7$.

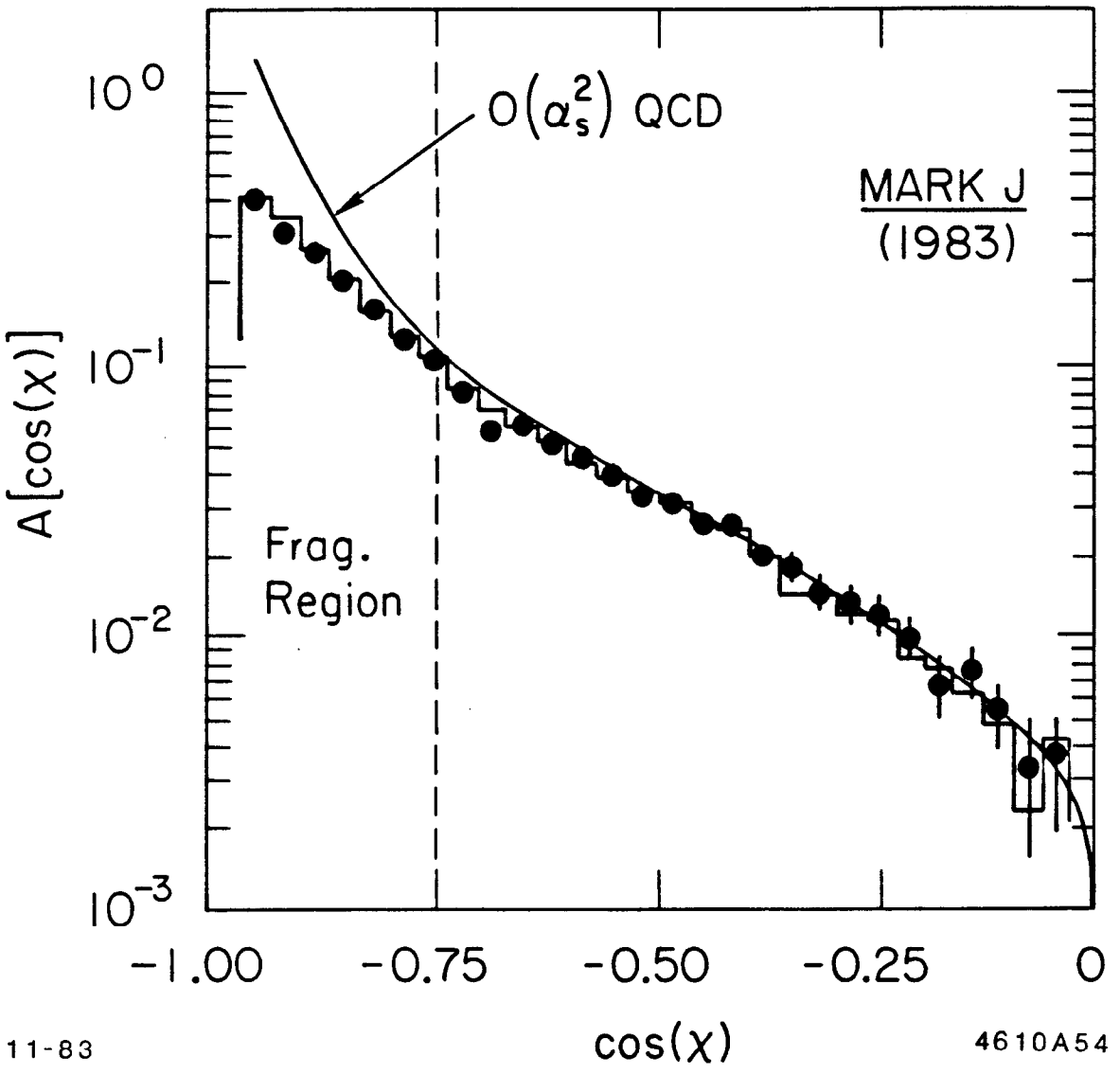

Fig. 22. The EECA as a function of $cos\chi$ as measured by MARK J at E_{cm}= 34.6 GeV. The solid line is the fit to the LUND and ALI model.

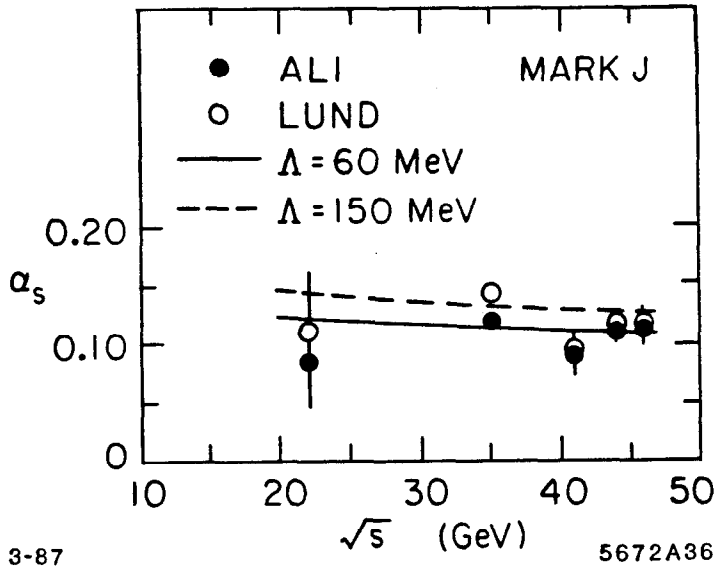

Fig. 23. The coupling constant α_s as measured by MARK J using the EECA. The solid points (open circles) are obtained using the ALI (LUND) model. Curves for Λ of 60 and 150 MeV are also shown.

2.4 Do Gluons Fragment Differently Than Quarks?

QCD predicts that high energy gluon jets should have a "softer" fragmentation function than quarks of the same energy. This prediction goes to the very heart of QCD, namely it arises from the fact that QCD is non-Abelian and, hence, the gluon has a self coupling. Referring to Fig. 24, color factors conspire to make the ggg vertex 9/4 times "stronger" than the qqg vertex. It has been shown[26] that for a highly perturbative topology (namely when the gluon/quark are sufficiently high energy) the jet opening angle δ (ala the Sterman-Weinberg definition) follows the relation

$$\delta_{gluon} = \delta_{quark}^{4/9}$$

where δ is measured in radians. So for example at $E_{cm} \approx 30$ GeV, $\delta_{quark} \approx 30^o$ would imply $\delta_{gluon} \approx 40^o$ while at SLC/LEP energies $\delta_{quark} \approx 10^o$ and $\delta_{gluon} \approx 25^o$. What evidence do we have for such effects?

The first evidence for softer gluon fragmentation was presented by JADE[27] in 1983. They used 3-jet events to show that the average hadron transverse momentum, $< P_t >$, was larger for hadrons in gluon jets than in quark jets of the same energy. A sphericity analysis was performed on the data and cuts ($Q_1 < 0.06$, $Q_2 - Q_1 > 0.07$) were made to select planar, 3-jet events. Particles in these planar events were assigned to one of three jets using the method of triplicity. The jet directions were then calculated from the vector sum of the particles which constitute each jet. Because jet directions are better measured than jet energies, the jet energies were calculated from the jet directions on the assumption that the partons are massless. These energies, E_j^d, were then ordered such that $E_1^d > E_2^d > E_3^d$. Events having a jet with less than four particles or an observed energy of less than 2 GeV were removed from the sample. Both charged and neutral particles were used in the analysis. At 33 GeV the Monte Carlo models for QCD indicate that the probabilities that jets #1, #2 and #3 are the gluon are 12%, 22% and 51%, respectively and 9%, 20% and 34% at 22

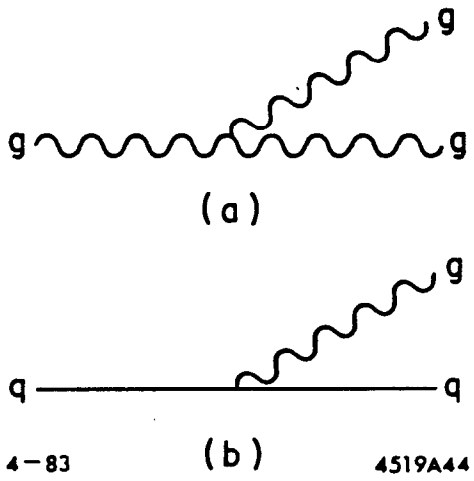

Fig. 24. The contrasting "strengths" of the triple gluon vertex and the quark-quark- gluon vertex.

GeV. The sum of these three probabilities is not 100% because the 3-jet sample is contaminated by $q\bar{q}$ events. The thrust of the analysis is to compare jets of the same energy but with different gluon content.

Figure 25 shows the $< P_t >$ measured relative to the jet axes for the three jets. Data are from the 22 and 33 GeV energy regions. The data are not corrected for detector biases, and both neutral and charged tracks enter into the plot. Jet #2 has a smaller $< P_t >$ than jet #3. The Monte Carlo models predict that the gluon content of jet #2 is ~25% and that of jet #3 is ~50% for $6 < E^d_{2,3} < 10$ GeV. The data in this jet energy region are plotted in Fig. 26 in terms of P_t. In the region of 0.2 GeV/c $< P_t <$ 1.5 GeV/c the data were fit with $d\sigma/dP_t \propto exp(-A_j P_t)$ and the ratio of $A_2/A_3 = 1.13 \pm 0.04$ was found indicating the jet with higher gluon content has a larger $< P_t >$. Using charged particles only, $A_2/A_3 = 1.10 \pm 0.05$.

We return now to Figs. 25(b)-25(d). Two models were used for comparison with the data. The result of the LUND model is shown in Fig. 25(d). The model used in Figs. 25(b) and 25(c) is the independent fragmentation model of Hoyer et al.[17] In Fig. 25(b) the quarks and gluons fragment identically, namely $\sigma_q = \sigma_g =$ 330 MeV/c, whereas in Fig. 25(c) $\sigma_q =$ 330 MeV/c but $\sigma_g =$ 500 MeV/c, namely the gluon is assigned a larger primordial P_t. From Figs. 25 and 26 one can conclude that events which are gluon enriched have a larger hadron $< P_t >$ indicating a softer fragmentation.

Recently this result has been confirmed by the Mark II group using a rather different approach. Mark II[28] capitalized on their large hadronic sample at E_{cm} = 29 GeV to select 3-jet events which were 3-fold symmetric – namely which were close to the orientation in which each jet was separated from its neighbors by 120°. Under these conditions one would expect each jet (parton) to carry an equal energy of 1/3 E_{cm}. In addition, one would expect one-third of the jets to be gluons, two-thirds quarks.

The 3-jet events were found using a cluster algorithm. The requirement of 3-fold symmetry was that all inter-jet angles δ_j satisfy $100^o < \delta_j < 140^o$. A total

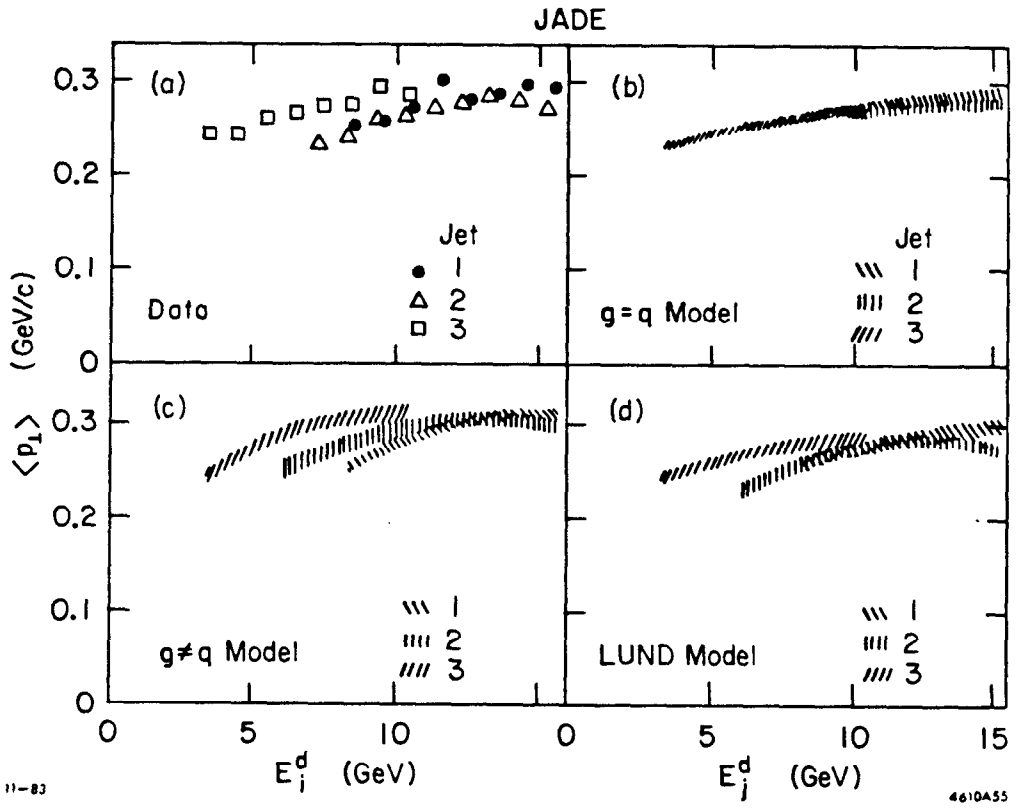

Fig. 25. The JADE measurement of $< P_T >$ as a function of jet energy for particles in 3-jet events. (a) Data from $\sqrt{s} = 22$ and 33 GeV, (b) prediction of the Hoyer model with identical quark and gluon fragmentation, (c) prediction of the Hoyer model with broader P_T for gluon fragmentation relative to quark and (d) prediction of the LUND model.

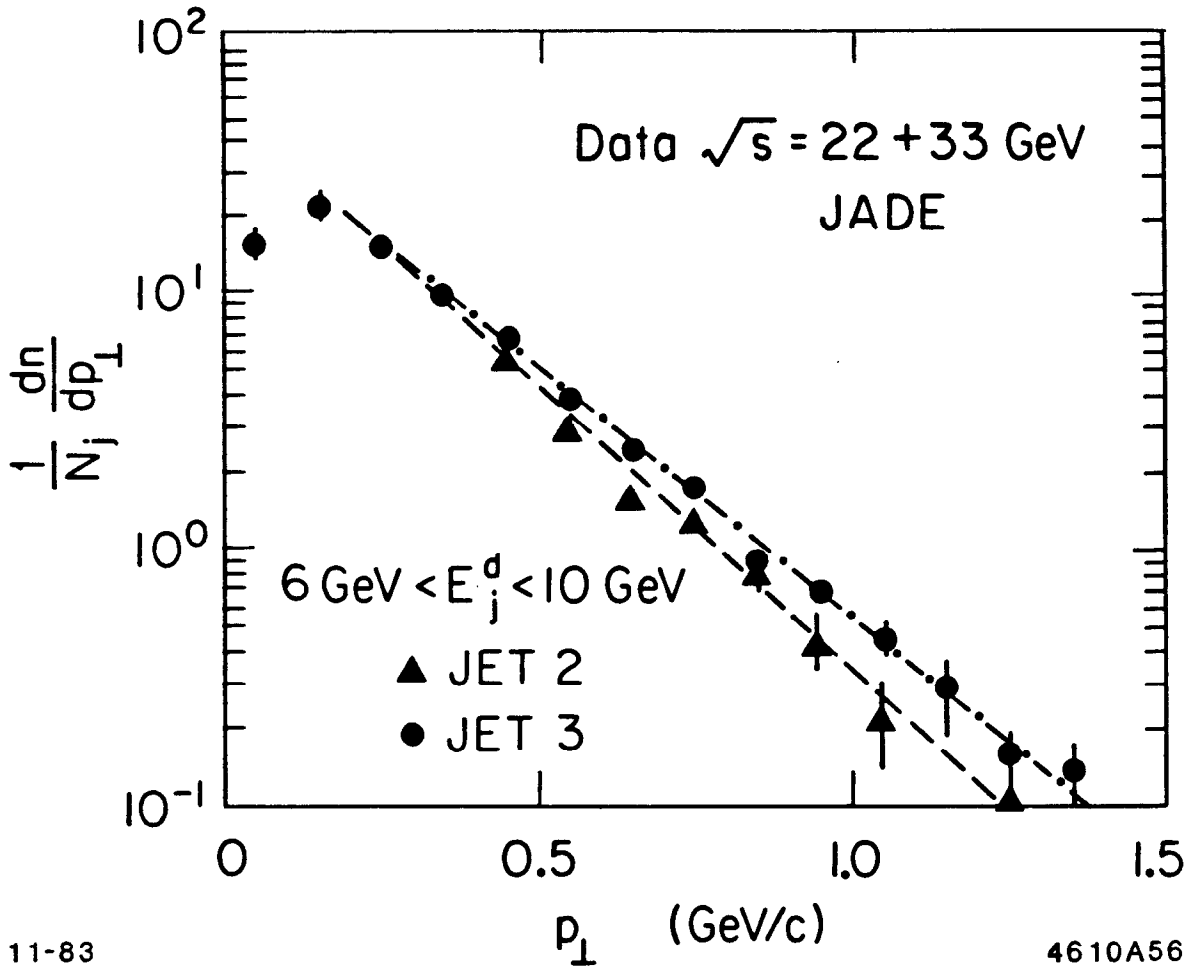

Fig. 26. The normalized differential cross section as a function of P_T for JADE data at $\sqrt{s} = 22$ and 33 GeV. Data are shown for the low and intermediate energy jet.

of 560 such events were found. The variable used to examine the fragmentation was $x_i = P_i/E_{jet}$ where P_i is the ith particle momentum and E_{jet} is the energy of the jet to which the particle was assigned. The particle x distribution was obtained and corrections were made for detector inefficiencies. This distribution is assumed to arise from events which are one-third gluon jets, two-thirds quark jets with each jet energy = 9.67 GeV. The data can be compared (see Fig. 27) with the corrected particle x distributions obtained from Mark II , TASSO, HRS and JADE in the jet energy range from 2.5 GeV to 17.5 GeV, where these data have been plotted assuming that they all come from a 2-jet topology. The 3-fold symmetric events are shown in this figure at $E_{cm}/N_{jet} = 29$ GeV$/3 = 9.67$ GeV. The different curves represent fits to the 2-jet data in the x regions indicated in the figure caption. One sees from Fig. 27 that the 3-fold symmetric events, which are gluon enriched relative to the 2-jet events, show a softer fragmentation function. This is shown more clearly in Fig. 28 where the hadron x distribution for the 3-fold symmetric events (solid points) are compared with the x distribution at $E_{cm} = 19.3$ GeV (as interpolated from the fits in Fig. 27) which are shown as a dashed line. In order to extract the fragmentation function of a 9.67 GeV gluon jet, the 19.3 GeV 2-jet event x distribution is used to subtract out the quark/antiquark x contribution from the 3-fold symmetric events. The resulting gluon x distribution is shown as the open points in Fig. 28. The conclusion drawn by the Mark II group is that gluon jets (open points) have a significantly softer fragmentation than quarks (dashed line) of the same energy.

The UA1 group has also measured the gluon fragmentation function.[20] While this discussion properly belongs in Section 3, it is included here because the result is strikingly similar to the Mark II. Details of how the $p\bar{p}$ collider experiments isolate jets are discussed in Section 3. For this analysis UA1 selects events containing two jets, each with $P_t > 25$ GeV/c, which are collinear within 30^o. Charged tracks are associated with the jets if they lie within the jet cone as specified by the azimuthal angle ϕ and the pseudo-rapidity η. UA1 uses the variable $z = P_\ell/E_{jet}$ where P_ℓ is the longitudinal momentum of the charged particle mea-

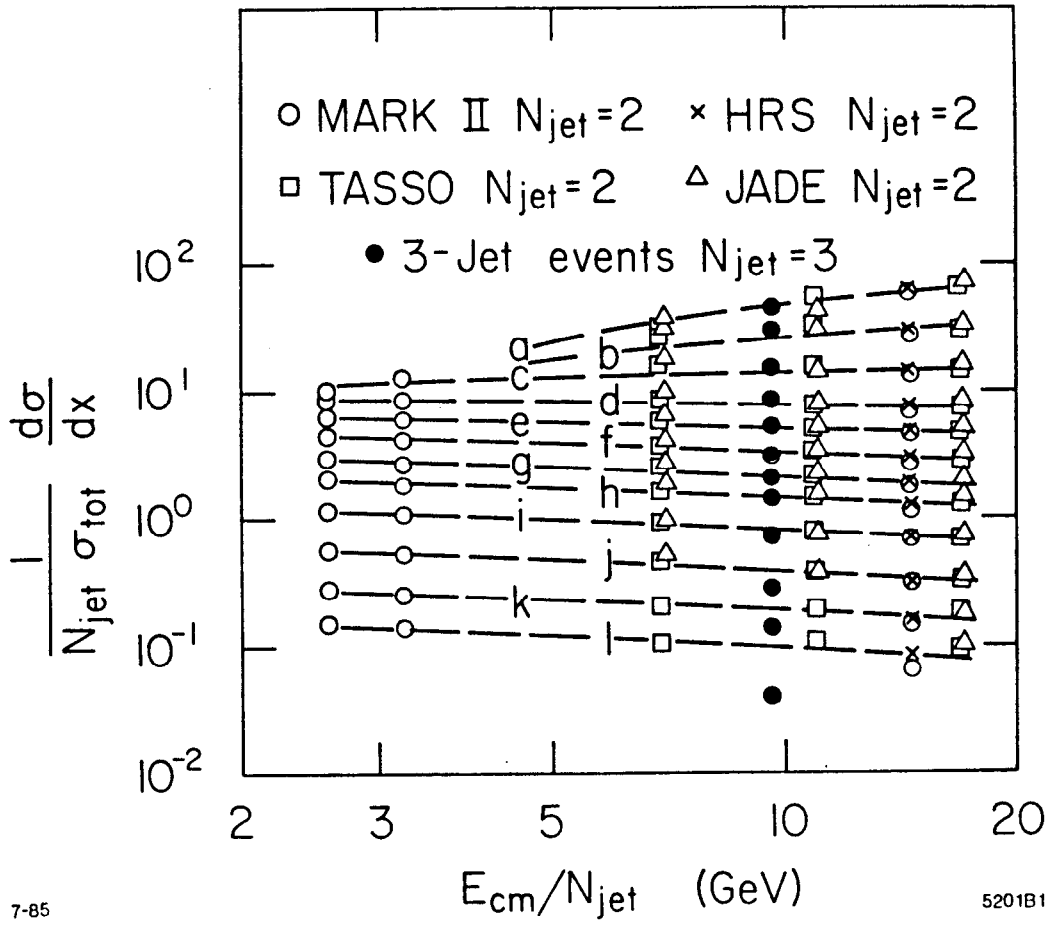

Fig. 27. The inclusive charged-particle cross section for a jet as a function of the jet energy, as measured by various experiments. The curves represent fits to the different data points for twelve x intervals which are defined by a = $0.03< x <0.05$, b = $0.05< x <0.10$, c = $0.10< x <0.15$, d = $0.15< x <0.20$, e = $0.20< x <0.25$, f = $0.25< x <0.30$, g = $0.30< x <0.35$, h = $0.35< x <0.40$, i = $0.40< x <0.50$, j = $0.50< x < 0.60$, k = $0.60< x <0.70$, l = $0.70< x <0.80$. The detector corrected inclusive charged-particle distribution for 3-fold symmetric, 3-jet events at E_{cm}= 29 GeV is also shown.

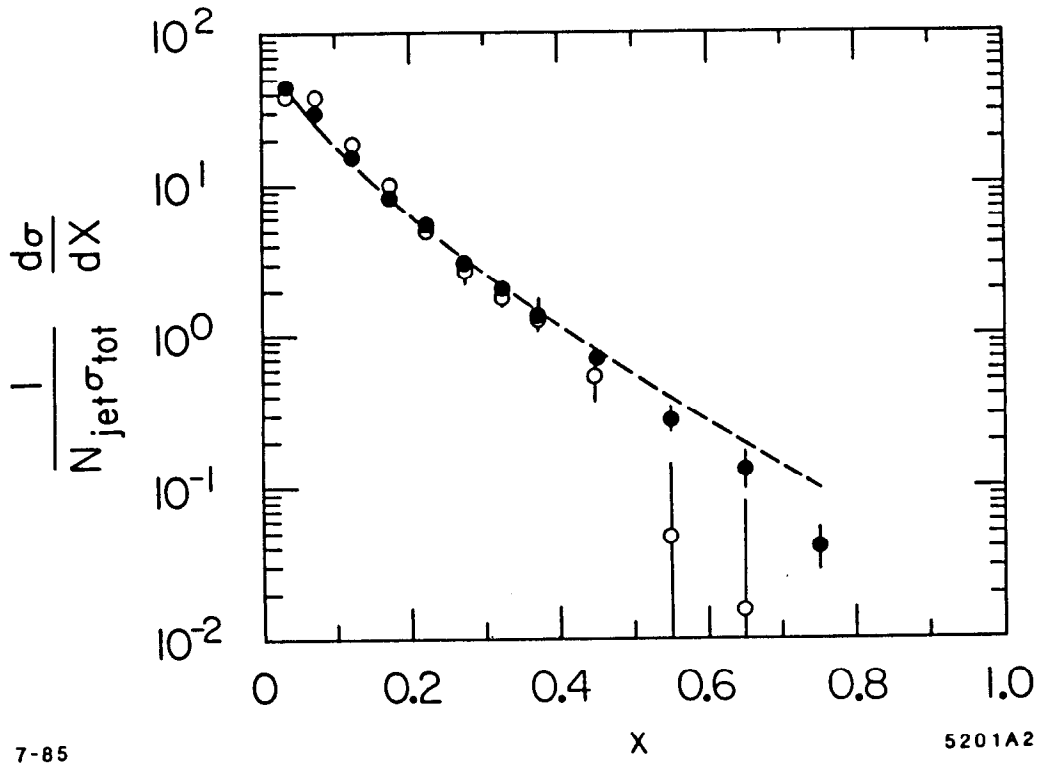

Fig. 28. The detector corrected inclusive charged-particle distribution for 3-fold symmetric 3-jet events at E_{cm} = 29 GeV (full symbols) in comparison with the inclusive charged-particle cross section of hadronic events at E_{cm} = 19.3 GeV, extrapolated from the fitted curves in Fig. 2 (dashed curve). The inclusive charged-particle distribution of a gluon jet of E_j= 9 GeV, assuming the subtraction discussed in the text, is shown by the open symbols.

sured relative to the jet axis. UA1 now needs a prescription for defining a gluon enriched and quark enriched region. Given the measured kinematics of the 2-jet system, one can extract the relevant 2-parton scattering variables $\hat{s}, \hat{t}, \hat{u}, x_1$ and x_2 where x_i are the fractional momentum carried by the 2-partons and $\hat{s}, \hat{t}$ and $\hat{u}$, are the Mandelstam variables of the 2-parton scattering process $(ab \rightarrow cd)$. Assuming the proton structure functions as input, one can calculate, jet-by-jet, the probability that the jet is a gluon or a quark. The probability for the subprocess $ab \rightarrow cd$ is given by

$$P(ab \rightarrow cd) = F_a(x_1, Q^2) \times F_b(x_2, Q^2) \times M^2(\hat{s}, \hat{t}, \hat{u})(ab \rightarrow cd) / \sum all\ subprocesses$$

where $F(x_i, Q^2)$ is the structure function for the appropriate subprocess, M is the QCD matrix element for that subprocess and $Q^2 = 2\hat{s}\hat{t}\hat{u}/(\hat{s}^2 + \hat{t}^2 + \hat{u}^2)$. For each jet the probability that it is a gluon is given by

$$P(jet = gluon) = \sum_{ab} P(ab \rightarrow gluon + anything).$$

Care is taken to compare quark and gluon jets at the same Q^2, thus avoiding quark/gluon fragmentation differences arising from non-scaling behavior. The resulting P(g) (or P(q) = 1-P(g)) distribution is shown in Fig. 29. The shaded regions are used as quark and gluon enriched samples.

Figure 30 shows the extracted quark and gluon fragmentation functions. The gluon fragmentation function appears softer, in agreement with the Mark II result. Figure 31 shows a comparison between the ratio of gluon and quark fragmentation functions as measured by Mark II in e^+e^- interactions at a $Q^2 = 841$ GeV^2 and UA1 in $p\bar{p}$ at $< Q >^2 = 2000$ GeV^2. (The two groups use slightly different variables, namely P/E_{jet} vs. P_t/E_{jet}, but this is a small effect.) The comparison is quite favorable given the experimental difficulties in obtaining these two fragmentation functions.

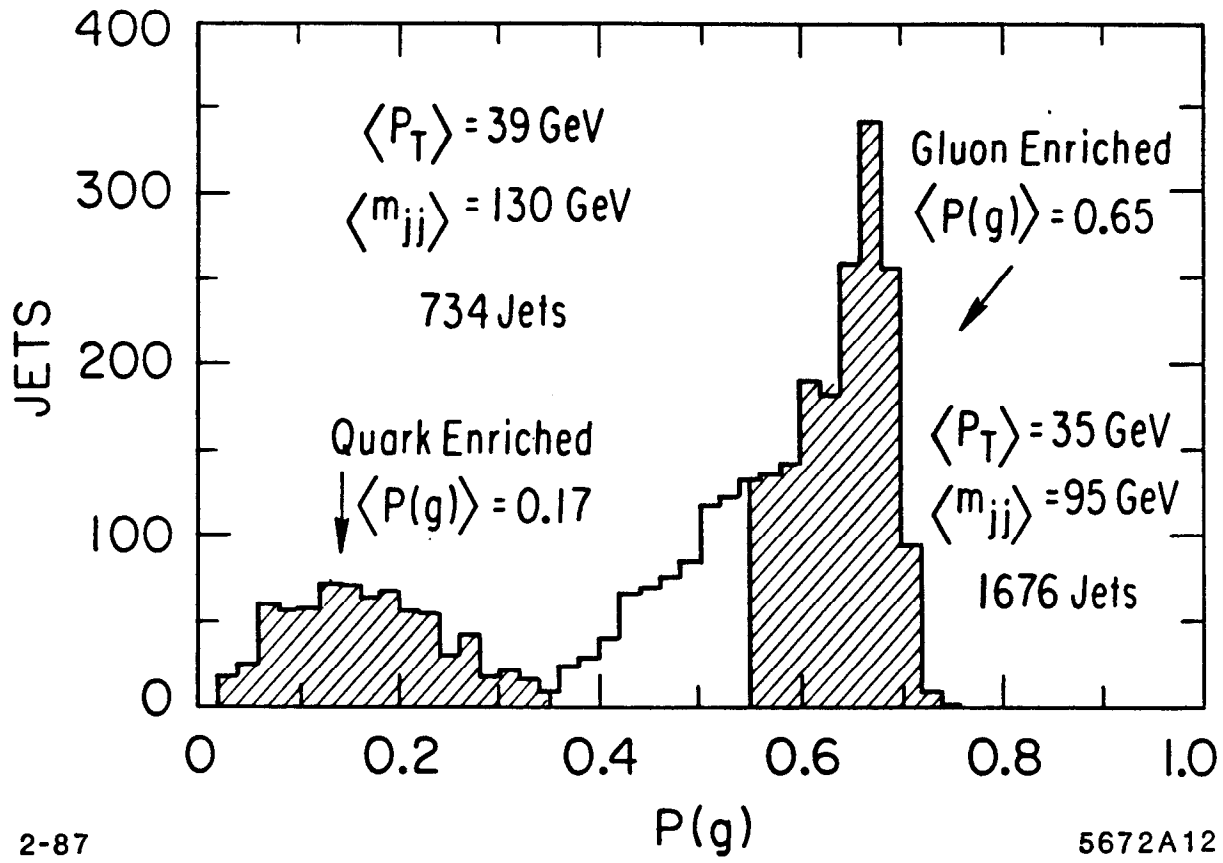

Fig. 29. The probability distribution for individual jets to be gluons. The shaded regions indicate the quark and gluon enriched samples.

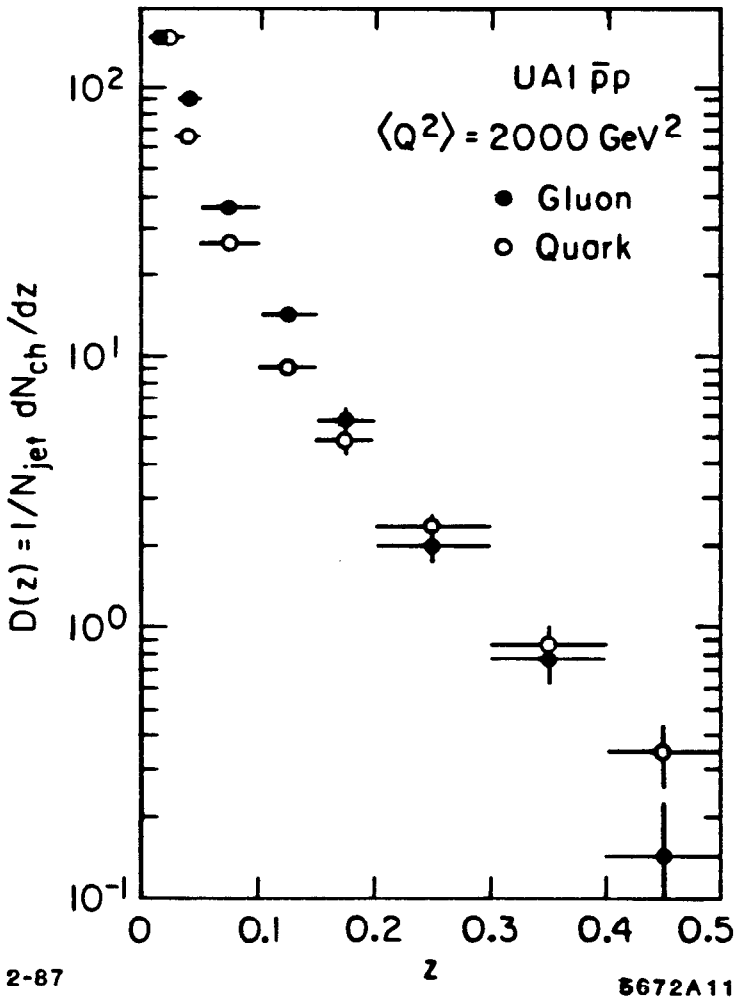

Fig. 30. Fragmentation functions for the quark-jets and the gluon jets as measured by UA1.

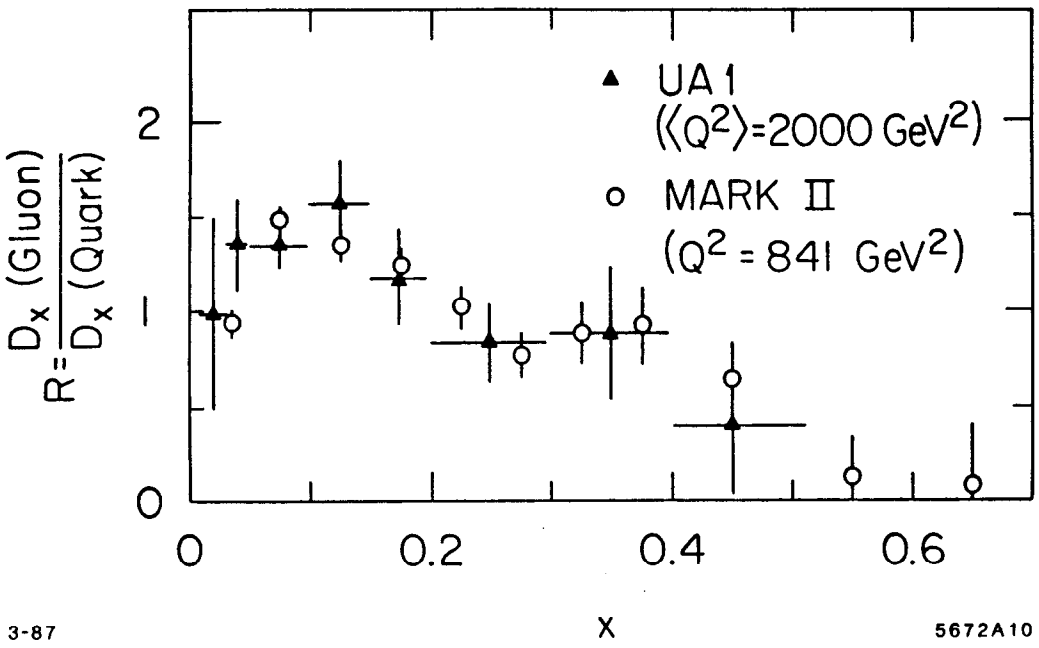

Fig. 31. The ratio of the gluon and quark fragmentation functions as a function of x, the fraction of momentum carried by the parton, are shown as measured by the Mark II and UA1.

2.5 Studies of Particle Flow in 3-Jet Events

Particle flow in 3-jet events has been studied by several groups.[80] These studies give support to the string type models (LUND) and exemplify the clearest evidence that independent fragmentation models do not fully represent the e^+e^- hadronic events at high ($\gtrsim$ 29 GeV) energies. Three-jet events are isolated as discussed in Section 2.2, each group using their own prescription. The conclusions of all three groups is the same and there is little reason to suspect that the 3-jet selection criteria produce any bias. Having formed the 3-jet axes, the particle or energy flow is plotted as a function of azimuthal angle with the ϕ=0 axis aligned along the fastest jet (jet 1). The data from TPC and JADE are shown in Figs. 32 and 33. The curves shown superimposed on the data are the predictions of the various Monte Carlo models as indicated on the figures. The feature of interest in these particle flow plots is the inability of the independent fragmentation (IF) model to account for the particle density in the region between jet 1 and jet 2 which are most frequently the quark and anti-quark. There is a depletion in this region relative to the expectations of the IF model. This depletion can be enhanced by selecting heavy particles (Fig. 32(b)) or equivalently particles with significantly large momentum normal to the event plane (Fig. 33(b)). The LUND model accounts for this depletion (in fact predicted it would be there) via the "Lorentz boost" effect. In the LUND picture, the quark and antiquark can be considered to be joined by a string. As the q and $\bar{q}$ move apart, the string stretches. The emission of a gluon can be visualized as a transverse "plucking" of the string, the direction of "pluck" being the direction of the gluon. The string breaks forming two substrings. The hadronization of these $q\bar{q}$ substrings occurs in their rest frame. The Lorentz boost required to bring the hadrons into the laboratory frame results in a depletion of hadrons in the region between the q and $\bar{q}$. This is shown graphically in Fig. 34(a) where the dashed line represents the string. It is clear that if the q, $\bar{q}$ and g fragment independently (and symmetrically as they do), so asymmetry relative to the parton directions will occur (Fig. 34(b)). These data are considered important verification of the

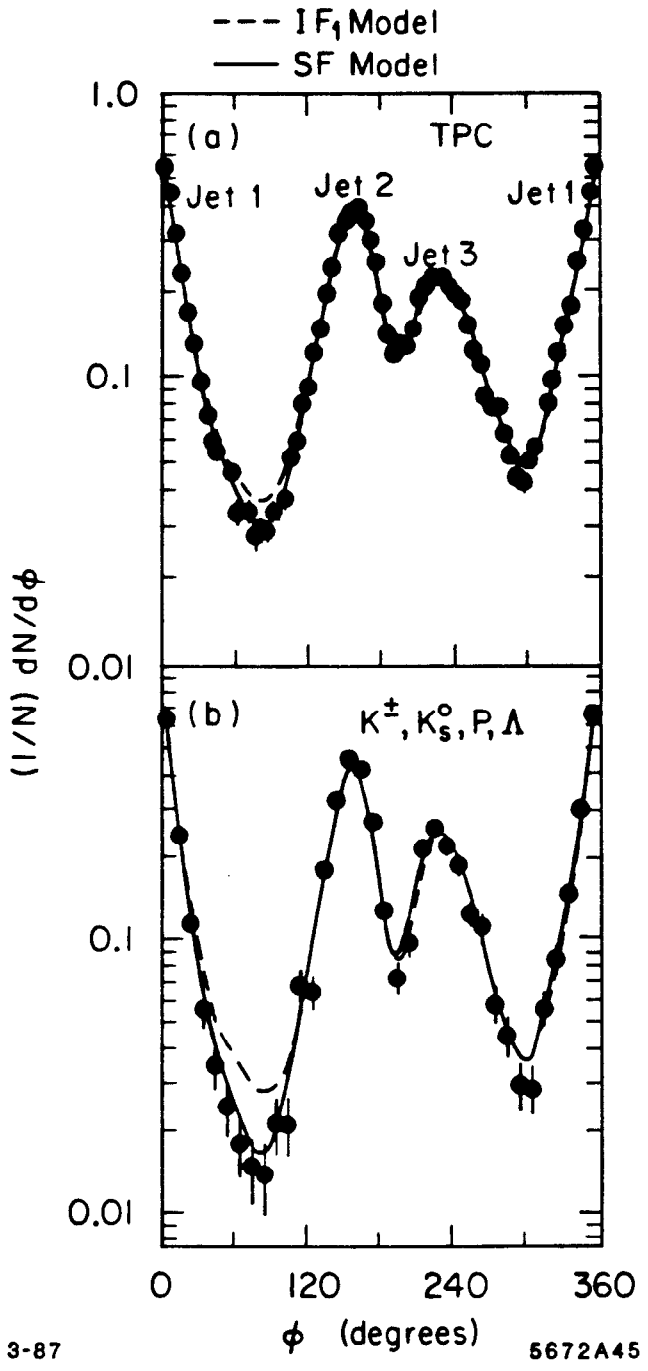

Fig. 32. The density of particles in 3-jet events as a function of the angle ϕ, where ϕ is measured in the event plane and ϕ=0 corresponds to the direction of the fastest jet. The TPC data are shown in (a) for all particles and in (b) for heavy particles. The predictions of the string and independent fragmentation models are shown.

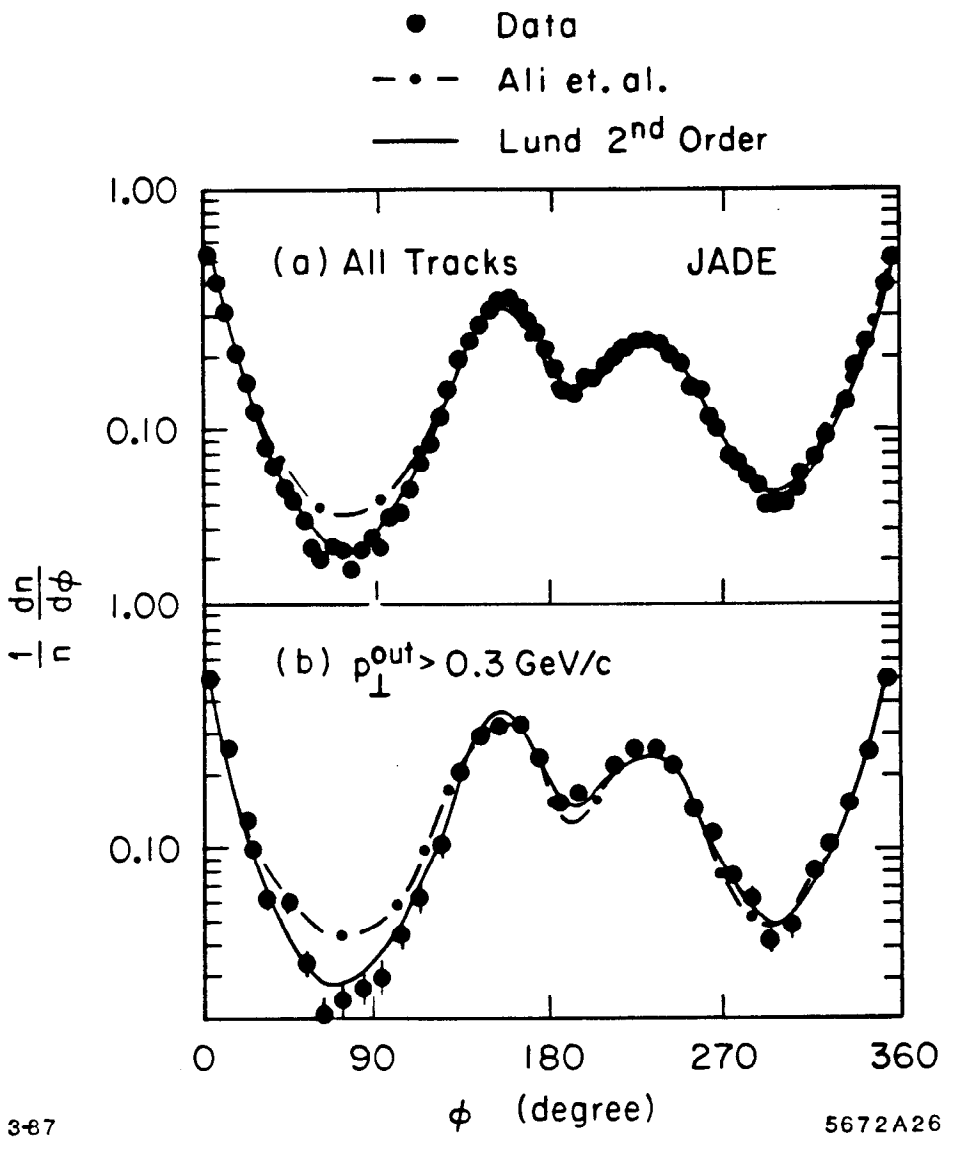

Fig. 33. The same plot as 32 except for the JADE data where (a) is for all particles and (b) is for particles with large momentum components out of the event plane.

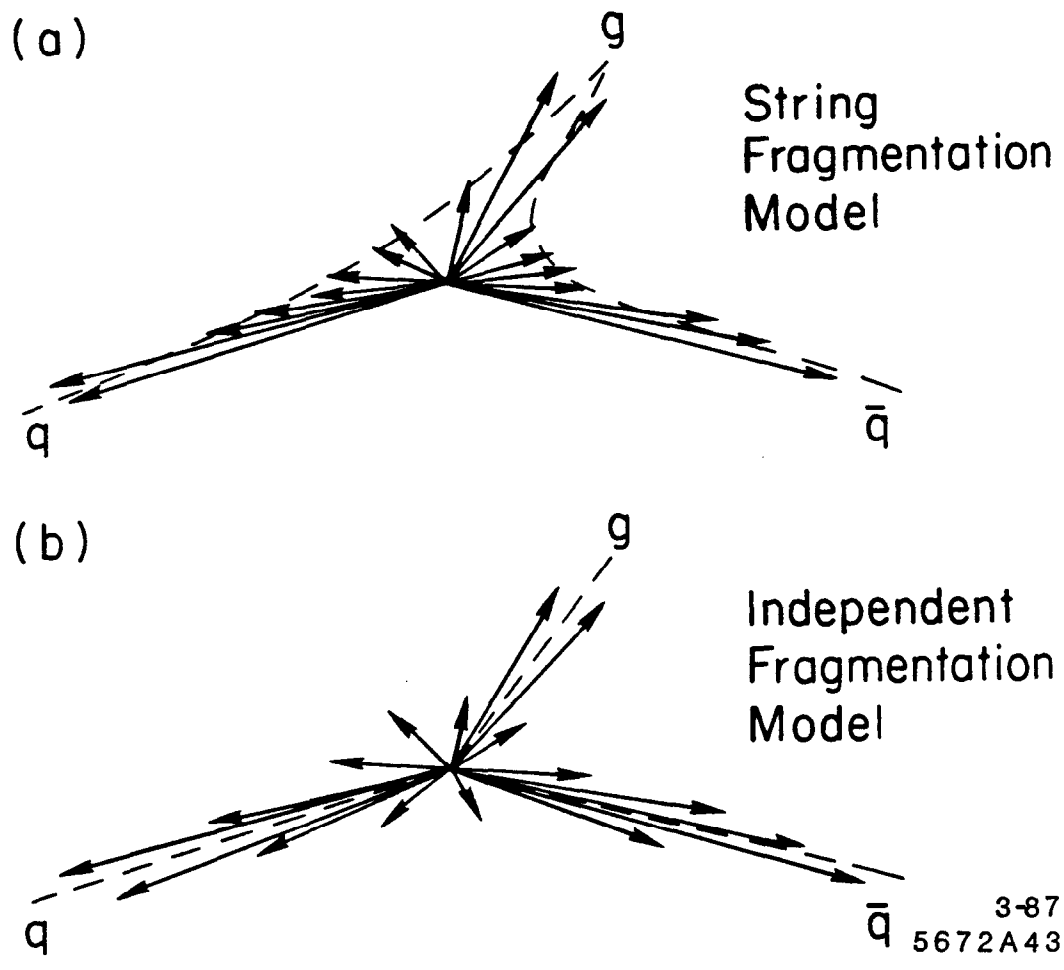

Fig. 34. Cartoon depicting the difference between the particle densities in 3-jet events as expected in the string picture (a) and the independent fragmentation picture (b).

LUND string-like description.

How does this relate to testing QCD? In a recent paper[31] Azimov et al., calculate the radiative pattern of soft gluons in $q\bar{q}g$ events arising from the three color sources q, $\bar{q}$ and g. QCD predicts that in 3-jet events of the kind we have been considering, the production of soft gluons in the region between the quark and antiquark is reduced because of negative interference between the radiation emitted by the $q\bar{q}$ system and the gluon. The authors further postulate a duality between the soft gluon flow and hadron flow, implying that the destructive interference will be seen in the hadrons.

As outlined in Ref. 31, this QCD calculation explains the features of the data shown in Figs. 32 and 33; namely QCD can explain the string effect. These theoretical ideas have been tested further by comparing the hadron "radiation patterns" in $q\bar{q}g$ and $q\bar{q}\gamma$ events. Since the photon carries no color, there will be no interference with the $q\bar{q}$ dipole radiation pattern and no depletion should be seen in $q\bar{q}\gamma$ events. The directivity diagram for soft gluon radiation in $q\bar{q}g$ (solid lines) and $q\bar{q}\gamma$ (dashed lines) events is shown in Fig. 35. The distance from the origin represents the soft gluon density at an angle ϕ measured relative to the quark jet. (The radial scale is logarithmic in this figure.) To reiterate, we see from this figure that $q\bar{q}\gamma$ events will have more hadrons in the region opposite the photon than the $q\bar{q}g$ events will have opposite the gluon jet. Again, we have assumed a duality between soft gluon flow and hadron flow.

The comparison of $q\bar{q}\gamma$ and $q\bar{q}g$ events has been studied by the TPC[32] and the Mark II.[33] The analyses strongly support the QCD calculation of Azimov et al. Both groups chose 3-jet events ($q\bar{q}g$) using a cluster algorithm and select $q\bar{q}\gamma$ events by requiring two hadronic jets plus an isolated high energy ($< E_\gamma > \sim 6$ GeV) photon. The jets and photon are required to be coplanar. Because TPC was using a smaller data set than Mark II, they increased their $q\bar{q}\gamma$ sample with events containing two non-collinear hadron jets and a missing photon. Both groups make additional cuts to purify the event samples. The energies of the three

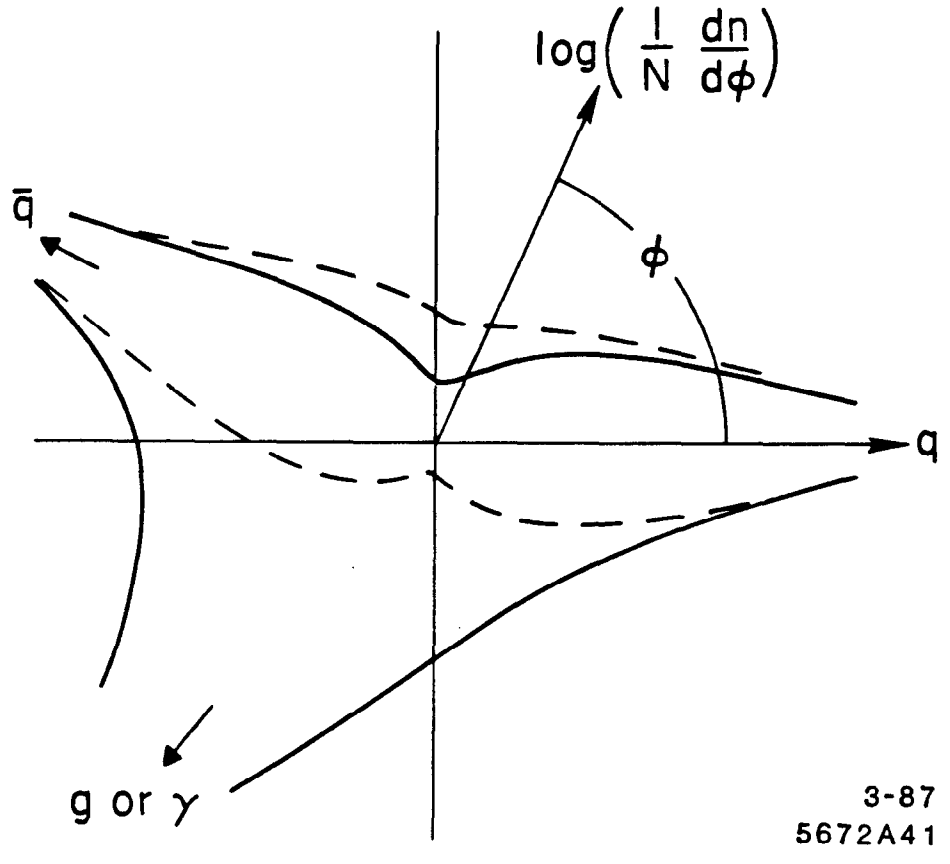

Fig. 35. Directivity diagram of soft gluon radiation in $q\bar{q}g$ (solid) and $q\bar{q}\gamma$ (dashed) events. The radial distance from the origin measures the density of soft gluons emitted at the azimuthal angle ϕ with respect to the quark jet. The radial scale is logarithmic.

jets (or γ) are calculated from the jet (γ) angles. What makes the comparison of the $q\bar{q}\gamma$ and $q\bar{q}g$ events meaningful is the similarity of the kinematics of the two event types. Table V demonstrates this is the case of the TPC analysis, where $< E_i >, < \phi_i >$ refer to the average jet energy and angle. Similar agreement is obtained by the Mark II. Table VI summarizes the number of candidate events and the probability that the lowest energy jet is a photon or a gluon.

Table V
(TPC Data)

	$q\bar{q}g$	$q\bar{q}\gamma$	qq(γ)
$< E_1 >$ GeV	12.7	12.7	12.2
$< E_2 >$ GeV	10.2	10.0	9.9
$< E_3 >$ GeV	6.1	6.3	6.9
$< \phi_1 >$	$\equiv 0$	$\equiv 0$	$\equiv 0$
$< \phi_2 >$	153^o	152^o	145^o
$< \phi_3 >$	231^o	229^o	235^o

Table VI

	TPC	Mark II	Prob. JET 3=g,γ
$q\bar{q}g$	2537	6585	60-65%
$q\bar{q}\gamma$	117	320	75-85%
$q\bar{q}(\gamma)$	1564		70%

The data is shown in Fig. 36 (TPC) and Fig. 37 (Mark II). In both analyses one sees clearly the effect predicted by QCD – namely the region opposite the gluon has a lower particle density than that opposite the photon ($\phi \simeq 80^o$ in Figs. 36 and 37). (The difference in hadron flow at $\phi \simeq 230^o$ is, of course, trivial

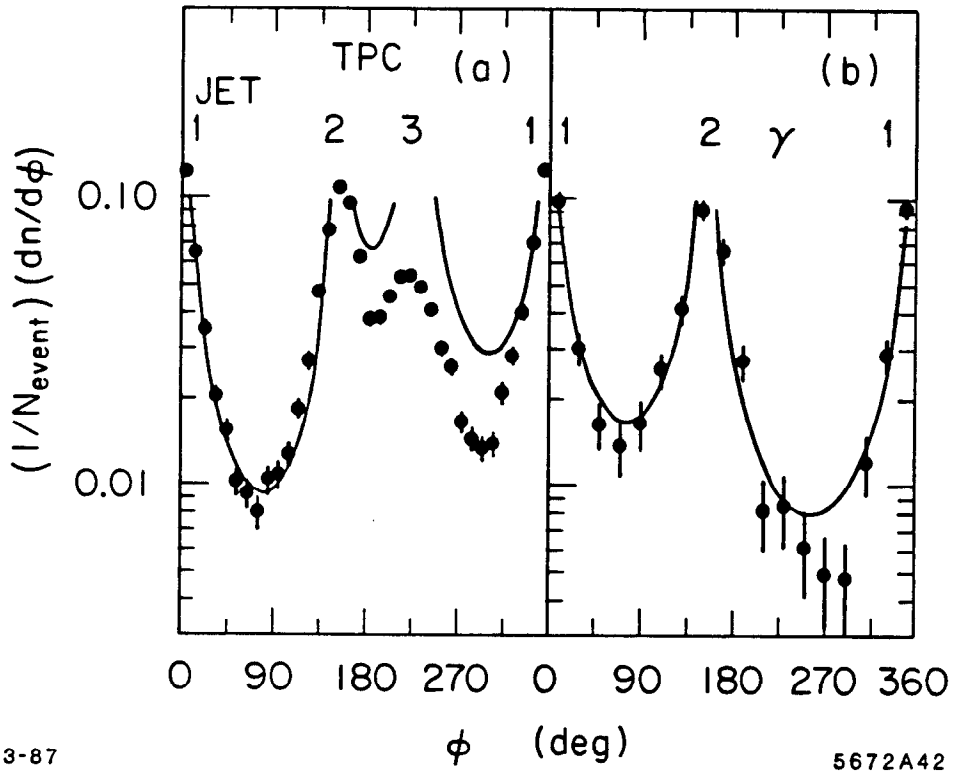

Fig. 36. TPC data showing the density of hadrons in the $q\bar{q}g$ events (a) and the $q\bar{q}\gamma$ events (b). Jet 1 and jet 2 are typically the q and $\bar{q}$. The lines are the predictions of asymptotic QCD for the flow of soft gluons.

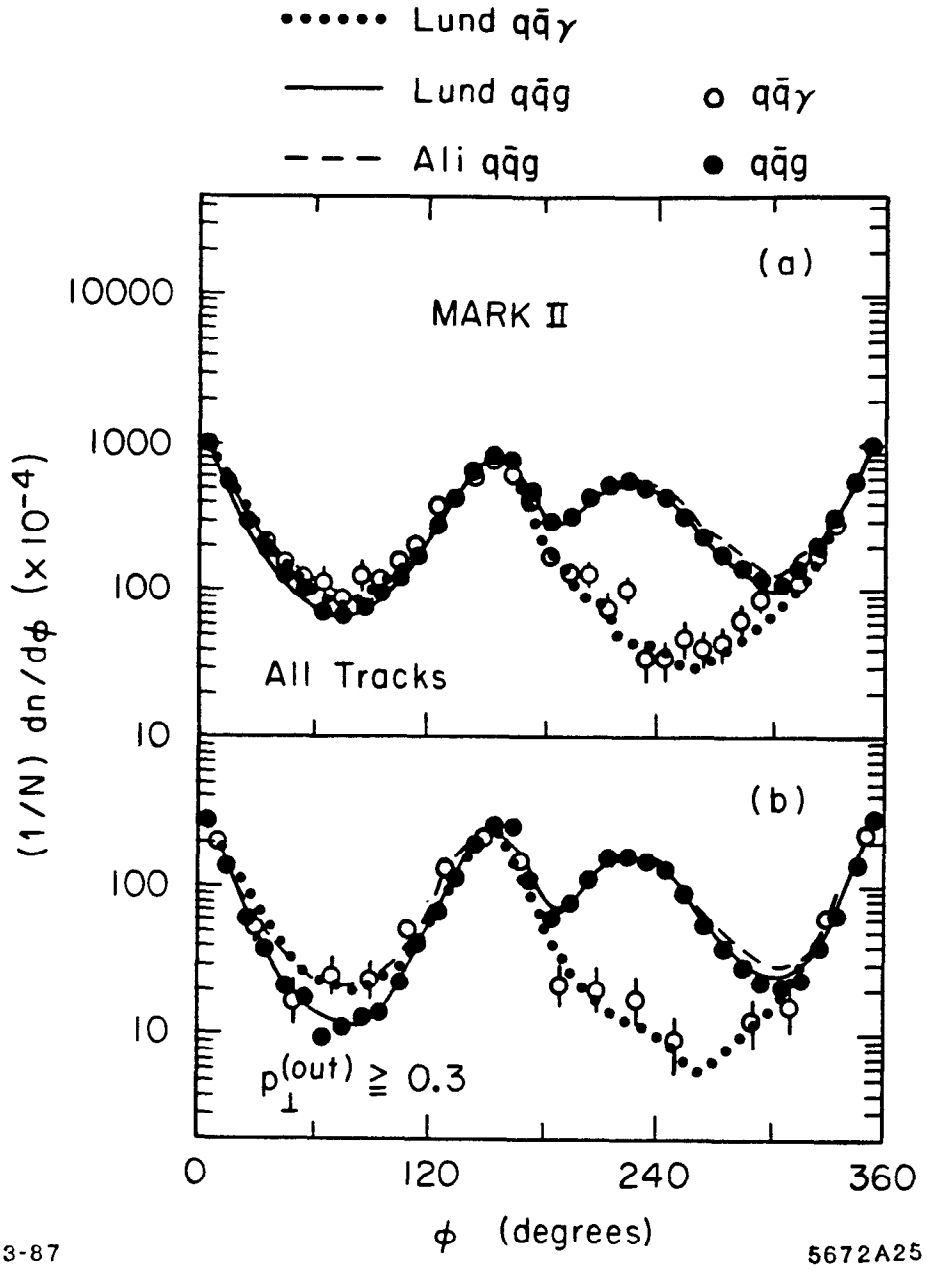

Fig. 37. Mark II data showing the density of hadrons in the $q\bar{q}g$ events (solid points) and the $q\bar{q}\gamma$ events (open points) for all tracks (a) and for tracks with large momentum out of the event plane (b). $\phi = 0$ corresponds to the direction of the fastest jet increasing to jet two and jet three, respectively. The predictions of the LUND and ALI models are indicated on the figure.

since this is the g, γ direction). The two groups display different curves. The TPC show the QCD prediction with $\phi_q = 0, \phi_{\bar{q}} = 153^o$ and $\phi_{g,\gamma} = 231^o$. In the region of expected validity – namely not too close to the parton directions – the QCD predictions agree quite well with the hadron distributions, except in the region close to the gluon jet. This disagreement in the area of the gluon jet is not a new revelation, but presumably relates to the fact that at PEP energies we have not yet approached the asymptotic region assumed in the QCD calculations. Asymptotic QCD would predict a ratio of 9/4 for the soft gluon multiplicity in gluon versus quark jets. What is observed at these pre-asymptotic energies is more like 1.3. The Mark II shows the predictions of the LUND model and the Ali et al. independent fragmentation model. One draws the same conclusions discussed above namely the "string effect" accounts well for the data while the independent fragmentation model does not. In addition we see excellent agreement between the LUND model and the data for the $q\bar{q}\gamma$ events. To display the interference effect more quantitatively, the data can be plotted (Fig. 38) as a ratio of the particle yield for $q\bar{q}g$ versus $q\bar{q}\gamma$ using a normalized valued of ϕ, namely $x = \phi/\phi_{12}$ where ϕ is the measured azimuthal angle of the particle and ϕ_{12} is the angle between jets 1 and 2. The coherent interference effect in the $q\bar{q}g$ parton geometry is clearly demonstrated. The solid line in the TPC plot is the QCD prediction assuming that jet 3 is always the gluon or photon. The dashed line allows for the fact that, in reality, the third jet is not always a gluon or photon. Hence, the solid and dashed line gives the range of the QCD predictions which is clearly in good agreement with the data. The dashed line in the Mark II data is the expected result for a model with independent fragmentation.

It is worth noting that the depletion effects seen using the hadrons in 3-jet events as discussed earlier in this section (Figs. 32 and 33) were seen in the context of comparisons with models, i.e., they were model dependent results. Comparison of $q\bar{q}g$ and $q\bar{q}\gamma$ events provides the same conclusion in a model independent manner. In addition one obtains a powerful test of the predictions of QCD for soft gluons and verification of the soft gluon/hadron duality. It

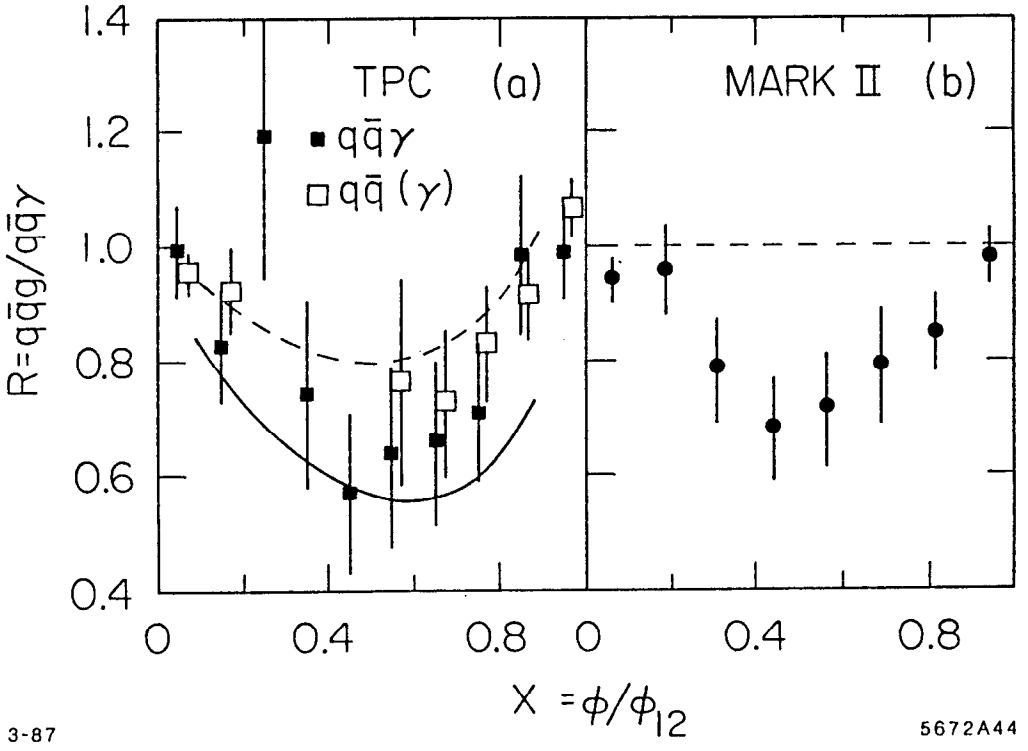

Fig. 38. The ratio of the hadron production in $q\bar{q}g$ and $q\bar{q}\gamma$ events as a function of the normalized angle $x = \phi/\phi_{12}$ where ϕ_{12} is the angle between jets 1 and 2. Both TPC and Mark II data are shown. The expected range of the QCD prediction for soft gluon flow is shown in the TPC data as solid and dashed lines; the dashed line accompanying the Mark II data is the prediction of the independent fragmentation model.

appears then that the LUND string model provides an excellent mechanism for mimicking the effects predicted by QCD.

3. TESTING QCD USING pp and $\bar{p}p$ COLLISIONS

Studying QCD in pp and $\bar{p}p$ collisions is considerably more difficult than in e^+e^- collisions. In the latter we produce the basic constituent quarks and gluons in a relatively "clean" environment. In pp (I will often use pp to imply both pp and $\bar{p}p$) collisions one is interested in the hard scattering process between either two constituent quarks (see Fig. 39) or a radiated gluon and a constituent quark or two radiated gluons. These processes are masked by the debris associated with the constituents which do not participate in the hard collision which makes the environment a lot less "clean" than in e^+e^- collisions. However, one is able to reach significantly higher Q^2 scales with $\bar{p}p$ collisions at the CERN S$\bar{p}p$S collider than at PETRA and QCD studies at $\bar{p}p$ and pp machines (ISR) are now making significant input to the information we have to test QCD. As we will see there are still experimental and theoretical problems. But these studies are still in their infancy and, as with e^+e^- tests, they will improve as these problems are confronted.

What do we need to know to untangle the QCD physics in a pp collision? We need to describe the subprocesses of parton-parton scattering (ab$\rightarrow$ cd), as depicted in Fig. 40. Hence we need to know the nucleon structure functions, the matrix element describing the scattering process ab$\rightarrow$ cd and the fragmentation functions of the final state particles. Typical lowest order QCD subprocesses are shown in Fig. 41(a) , where the λ_{ij} represent the relative probabilities of each subprocess. Life is not as simple as shown in Figs. 39 and 41(a) and we know it is going to be important to add the higher order (second and above) QCD effects. Some typical second order diagrams are shown in Fig. 41(b).

We would like to set up a program similar to that in e^+e^- collisions where one sees first the hard, lowest order scattering process (2-jet events), higher order

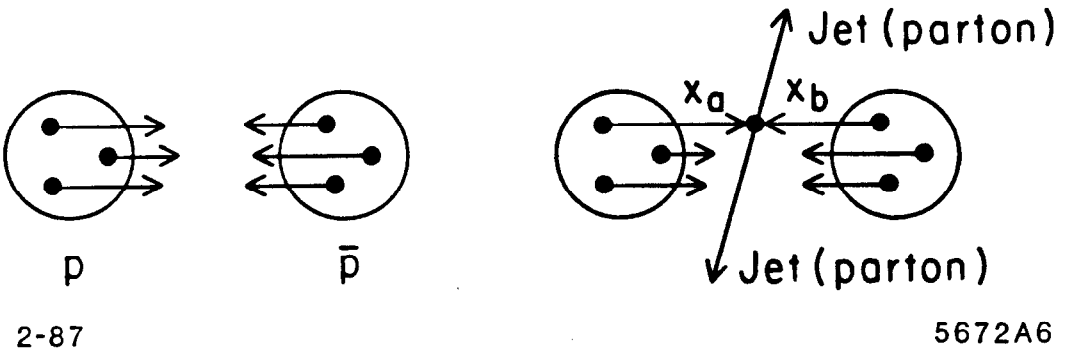

Fig. 39. Diagram of a hard scattering process in pp or $\bar{p}p$ collisions.

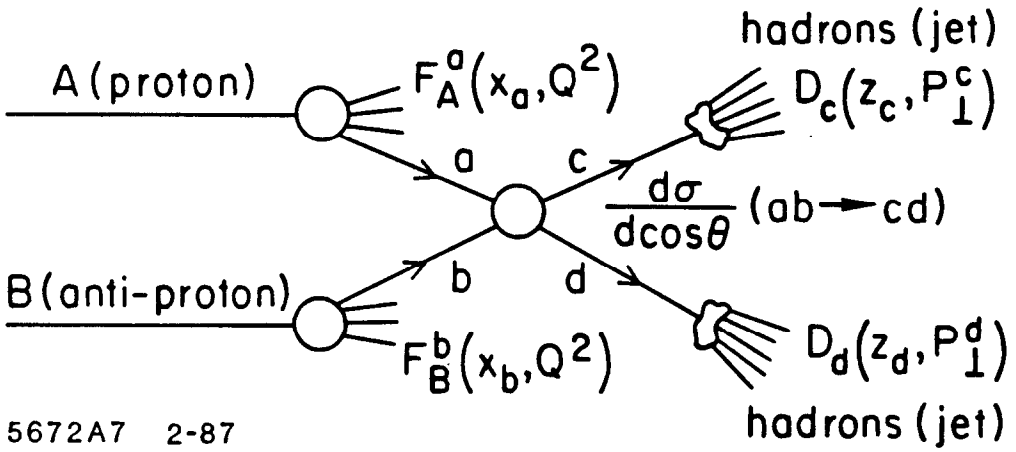

Fig. 40. Diagrams of a typical 2→2 parton scattering process. F is the structure function, $\cos\theta$ is the center-of-mass scattering angle, x is the fractional momentum carried by the parton and D is the parton fragmentation function defined by the parallel and perpendicular parton momenta z and P_T.

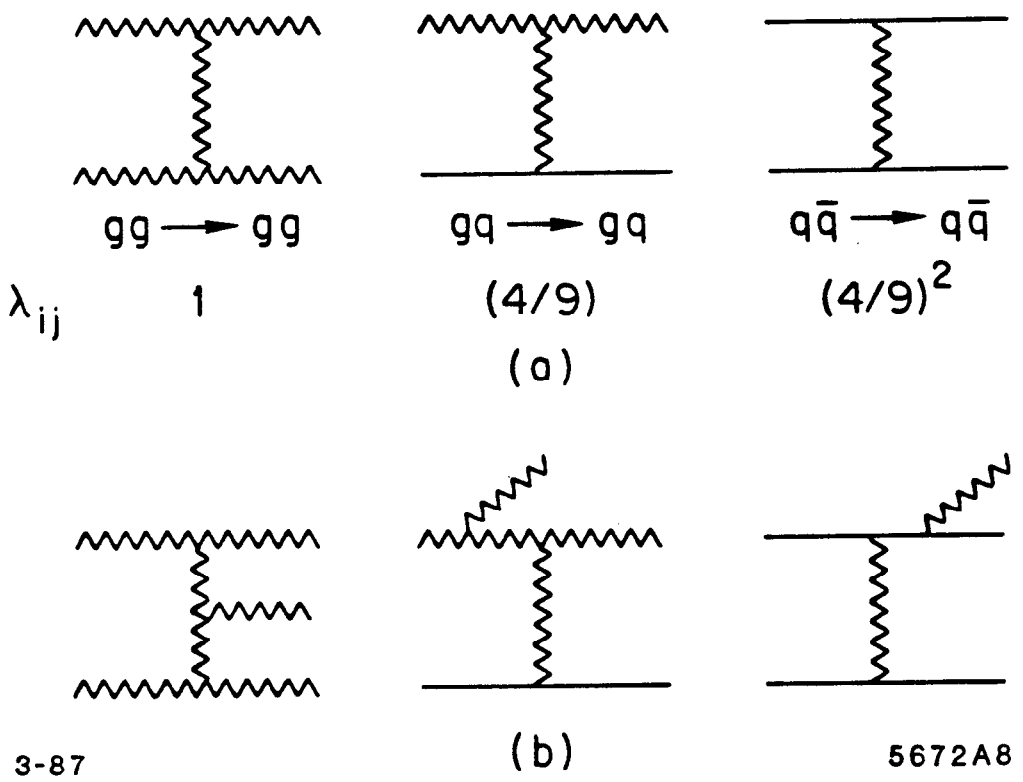

Fig. 41. (a)Typical 2→2 parton processes which lead to 2-jet events and (b) some of the higher order corrections to (a). The diagrams in (b) lead to 3-jet events when the radiated gluons are sufficiently energetic.

processes (3-, 4-jet events), measure α_s, etc. As noted before, the problems are numerous and we list below the most pressing. Firstly there are the theoretical issues:

1. How does one evaluate the cross sections, for example, for observing 2-jet events? To lowest order and neglecting non-scaling effects, the cross section for each subprocess ij factorizes:

$$\frac{d^3\sigma}{dx_1 dx_2 cos\theta} = \frac{F_A(x_1)}{x_1}\frac{d\sigma_{ij}}{dcos\theta}\frac{F_B(x_2)}{x_2} \tag{4}$$

   where $cos\theta$ is the center-of-mass scattering angle. As discussed by Combridge et al.[34] one obtains to good approximation a subprocess independent kinematic factor

$$\frac{d\sigma_{ij}}{dcos\theta} \approx \lambda_{ij}\frac{\alpha_s(Q^2)}{\hat{s}}(1-cos)^{-2} \tag{5}$$

   where $\hat{s}$ is the effective center-of-mass energy squared.

2. Since we are calculating the process to finite order, we are left with the dilemma about what scale (Q^2) the subprocess is occurring at.

3. One needs the quark and gluon structure functions for the proton. Combinations of theoretical and experimental input are used with the assumption

$$F(x) = g(x) + 4/9(q(x) + \bar{q}(x)).$$

4. Higher orders and the non-scaling effects in the behavior of α_s and the structure functions must also be included to extract meaningful conclusions.

Some of the experimental issues are:

1. The jets must be observed in a large background of hadrons coming from the partons which do not participate in the subprocess of interest. The experimental approach has been to concentrate on high P_T jets. However there remain problems of the assignment of particles to the jets, the jet energy scale....

2. How does one measure Q^2?

3. There are the usual problems of modelling the non-perturbative physics. The simulations are in general less advanced than those used in e^+e^- collisions and one is more dependent on the unknown gluon fragmentation function.

How do the experiments isolate jets? I will present data from the AFS collaboration at ISR, UA1 and UA2 at the CERN $\bar{p}p$ collider. Each group uses a slightly different technique, the details of which can be found in the experimental references given below. Typically, large energy deposits are sought in a grid defined by ϕ and θ (or η, the pseudo-rapidity). A window centered on these large deposits is used to associate smaller deposits with the primary initiator. Refinements are made to these cluster energies so that between the algorithm and the Monte Carlo simulation of the data, a robust procedure for extracting and correcting the jet energies is obtained. Striking multijet events are seen by all three groups, an example of which is shown in Fig. 42. By looking at this picture one can imagine how the jet finding algorithm works.

3.1 Inclusive Jet and Direct Photon Cross Sections

We now turn to the experimental data. Figure 43(a) shows the inclusive jet cross section as a function of jet P_T from the UA1 group.[85] What is plotted is $< d^2\sigma/dP_T d\eta >$ averaged over the rapidity region $\mid \eta \mid$<0.7. Both data from $\sqrt{s}$= 546 GeV and 630 GeV are shown. The QCD lowest order predictions shown in the figure agree quite well with the data. Higher order QCD will affect the normalization but probably to a lesser extent the P_T dependence. The major limitation in the inclusive jet cross section as a test of QCD is the ≈10% uncertainty in the jet energy scale which will almost certainly wipe out any sensitivity to higher order effects. Figure 43(b) shows the dimensionless (scaling) cross section $P_T^4 E d^3\sigma/dp^3$ as a function of $x_T = 2P_T/\sqrt{s}$. The data at the two energies overlap; however the lever arm in $\sqrt{s}$ is much too small to expect to

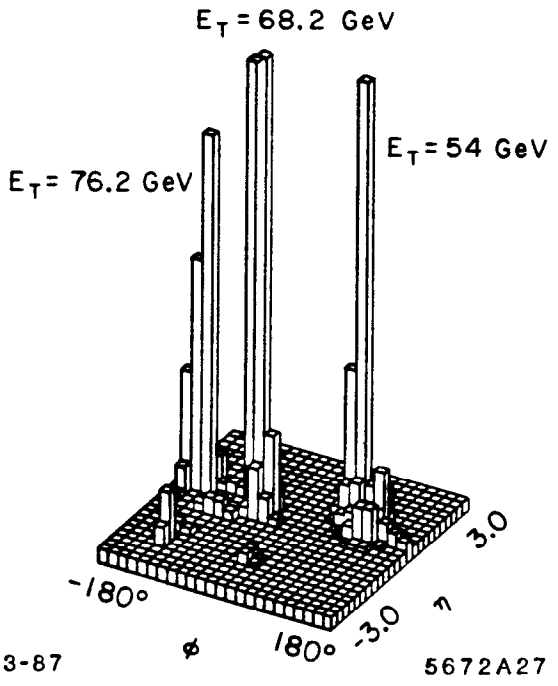

Fig. 42. A 3-jet event taken from the UA1 data. The event is shown in ϕ, η space with the vertical axis representing the energy contained in the particular ϕ, η cell. The jet transverse energies are indicated in the figure.

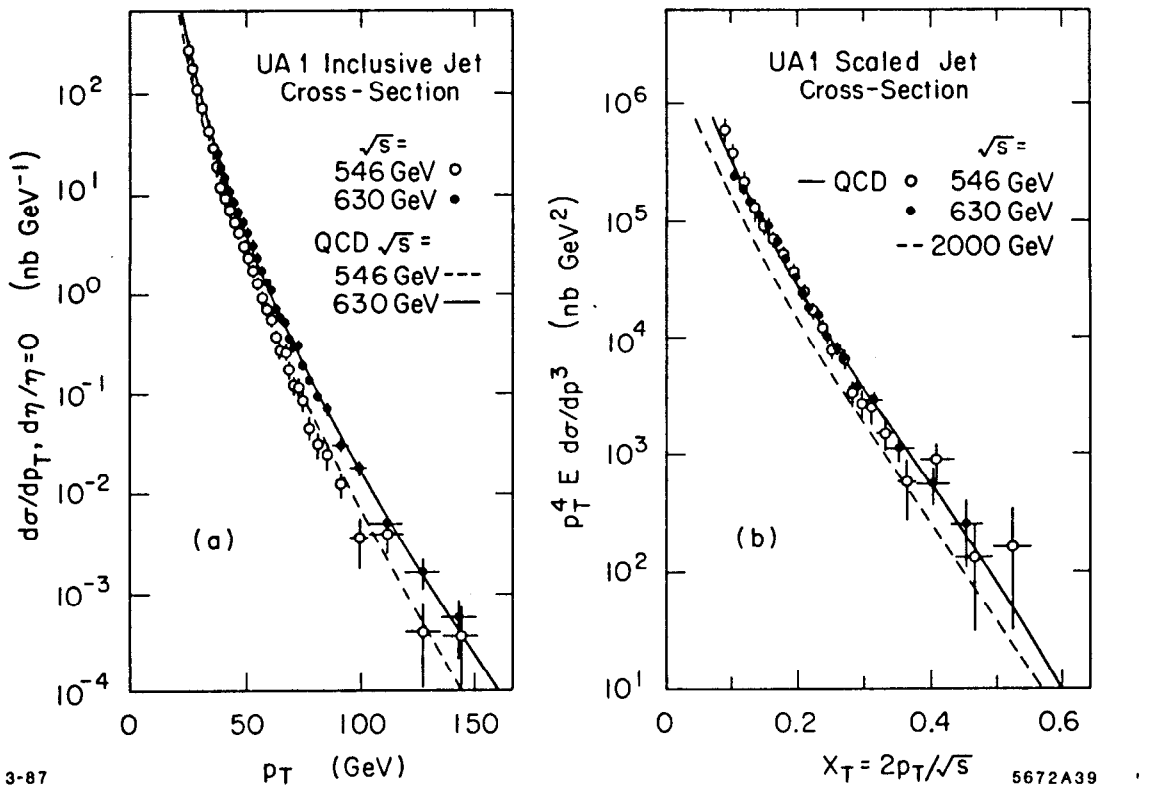

Fig. 43. (a) The inclusive jet cross section as a function of jet P_T and (b) the scaled jet cross section as measured by UA1. The data come from $\sqrt{s}$= 546 GeV and 630 GeV. Also shown are the predictions of QCD.

see the effects of non-scaling. Similar data have been published by the UA2 collaboration[36] and the AFS collaboration.[37]

One possible way to overcome the problems associated with measuring the inclusive jet cross section is to measure the inclusive direct photon cross section. The advantages are the absence of fragmentation effects, the good energy determination for high energy photons ($\approx 1\%$ for UA2) and the presence of $0(\alpha_s^2)$ predictions from theory. The clear disadvantage is that one has $\approx 10^4$ less cross section than for inclusive jet production and hence, the range of P_T with reasonable statistical weight is small. There is data available from the ISR experiments and UA2. I will show the UA2 data because it has an $< P_T > \approx 4$ times larger than the ISR experiments.[38]

The extraction of the direct photons from those coming from π^o's and η's is difficult. UA2[39] requires firstly that the photon be well isolated assuming that photons from π^o and η decays would be accompanied by other nearby hadrons. Further cuts are made using the pre-shower detection to distinguish single isolated photons from π^o and η decays where the two decay photons have coalesced in the calorimeters. Residual background contributions are estimated and removed for each P_T bin. The corrected cross section for $\bar{p}p \rightarrow \gamma +$ anything is shown in Fig. 44 along with the $0(\alpha_s^2)$ QCD prediction. The errors in the figure are dominantly statistical. In addition there is also a 20% normalization systematic error. The QCD curves are from the calculation of Aurenche et al.[40] When comparing the data with QCD, care must be taken to include the effects of bremsstrahlung from the final state quarks. These bremsstrahlung processes are sensitive to the isolation cuts. The two lower QCD curves shown in Fig. 44 exclude bremsstrahlung photons with the angle of the photon relative to the quark of less than 20^o and 45^o, respectively. The difference between these two curves represents the level of uncertainty caused by the isolation cuts. The overall agreement between QCD and the data is good and with more data in the future, these tests will become more compelling. But already they provide significant qualitative tests of $0(\alpha_s^2)$ QCD.

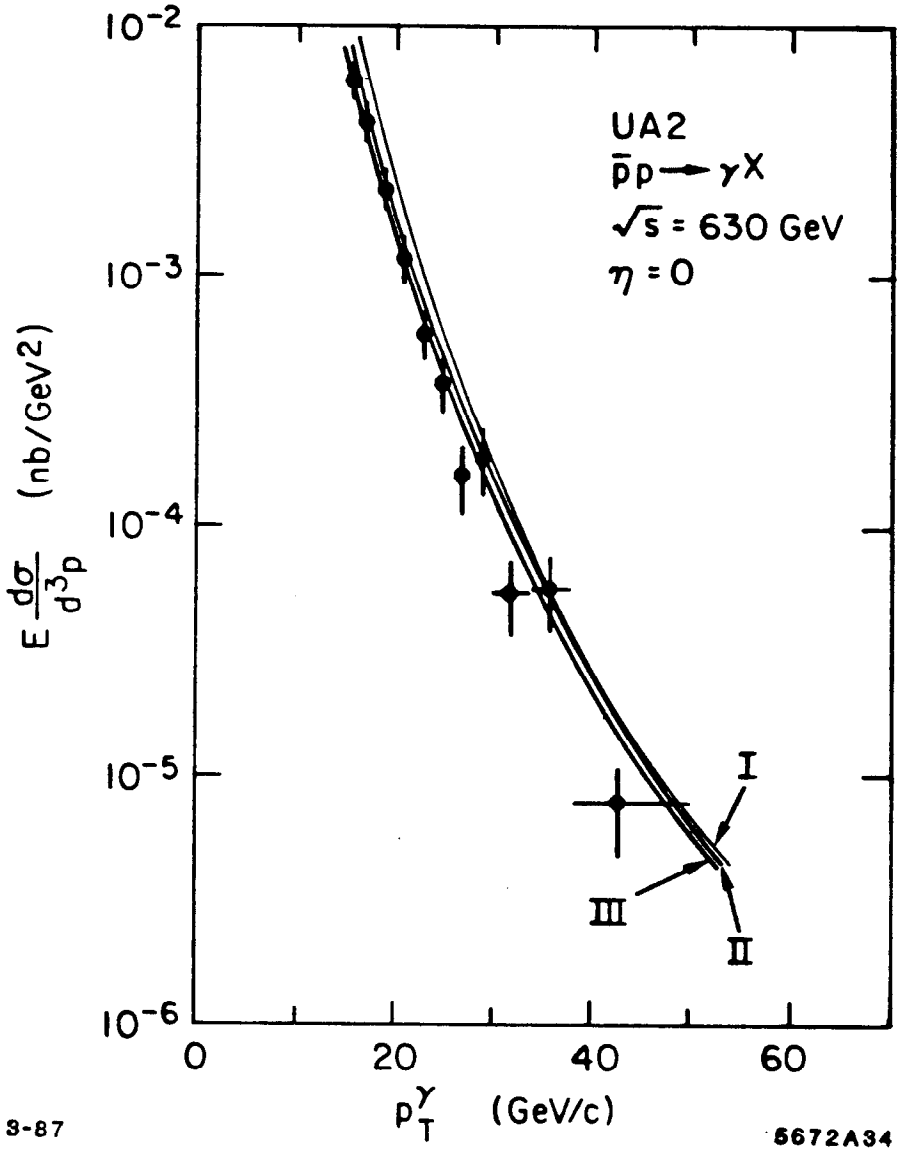

Fig. 44. The direct photon inclusive cross section as a function of P_T^γ from UA2. The curves correspond to the predictions of $0(\alpha_s^2)$ QCD. In II(III) QED bremsstrahlung from the quarks is omitted if the angle between the quark and photon is less than 20^o (45^o).

The NA14 group at CERN have examined direct photon production in γN scattering.[41] One expects a contribution from QED Compton scattering but in addition a substantial contribution from QCD processes. As with the direct photons in hadro-production, an $0(\alpha_s^2)$ calculation is available for comparison. The NA14 direct photon spectrum is shown in Fig. 45. Both statistical and systematic errors (arising mainly from the background subtraction) are shown. The dashed-dot line is QED Compton scattering while the solid line adds the $0(\alpha_s^2)$ QCD prediction.[42] The data are clearly not in agreement with the pure QED production and the addition of the QCD contributions gives good agreement.

3.2 Qualitative Tests Using 2- and 3-jet Events

There is copious 2-jet production at the CERN $\bar{p}p$ collider. What do studies of these events tell us? From these events effective proton structure functions have been extracted by both UA1[43] and UA2.[44] These data are largely consistent with each other and with QCD. Intrinsically the structure function is of fundamental importance. However with respect to providing a precise quantitative test of QCD the $\bar{p}p$ structure function measurements are limited by the large systematic error on the jet energy scale. This problem can be eliminated by studying the jet production angular distribution discussed earlier in this section. We show here data from UA1.[45] UA1 isolates events which have $\geq$ two jets, and select the two highest P_T jets ignoring the others. The subprocess center-of-mass energy is assumed to be the di-jet mass ($\sqrt{\hat{s}} = M_2$jet) computed using corrected jet four vectors. The center-of-mass 2$\rightarrow$2 scattering angle θ is defined relative to the average beam direction evaluated in the di-jet rest frame. The distribution in cosθ is shown for the selected 2-jet events in Fig. 46(a). In Fig 46(b) the same data are plotted as a function of x = $(1 + \cos\theta)/(1 - \cos\theta)$. Also shown in Fig. 46 are the expectations of leading order QCD (solid lines) and leading order QCD modified to account for the dependance of α_s and the structure functions on Q^2, i.e., non-scaling effects. To obtain the theoretical predictions required assigning relative weights to the competing subprocesses. However, since all the subpro-

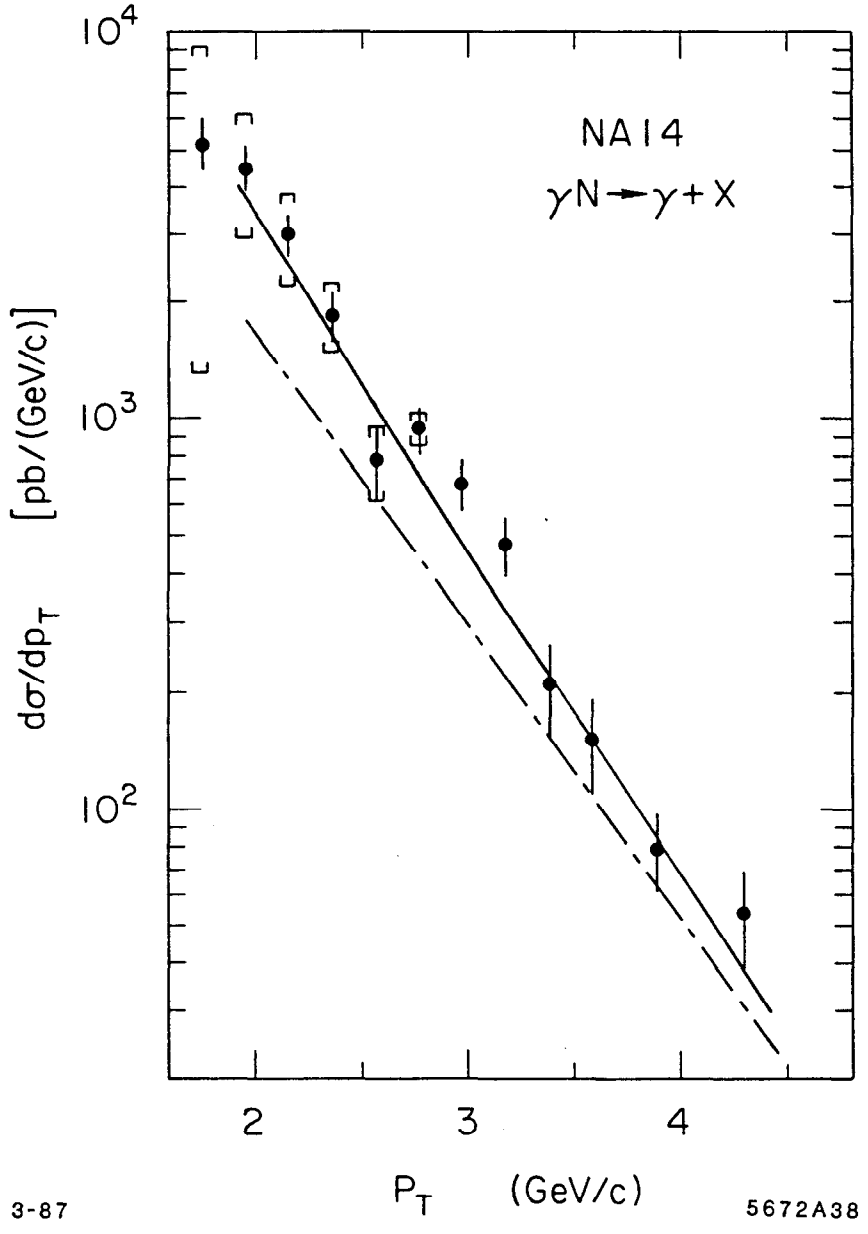

Fig. 45. The direct photon inclusive cross section as a function of P_T^γ as measured by NA14 at CERN in a photoproduction experiment. The dashed curve is the prediction for QED Compton scattering. The solid curve adds to this the effects of $0(\alpha_s^2)$ QCD corrections.

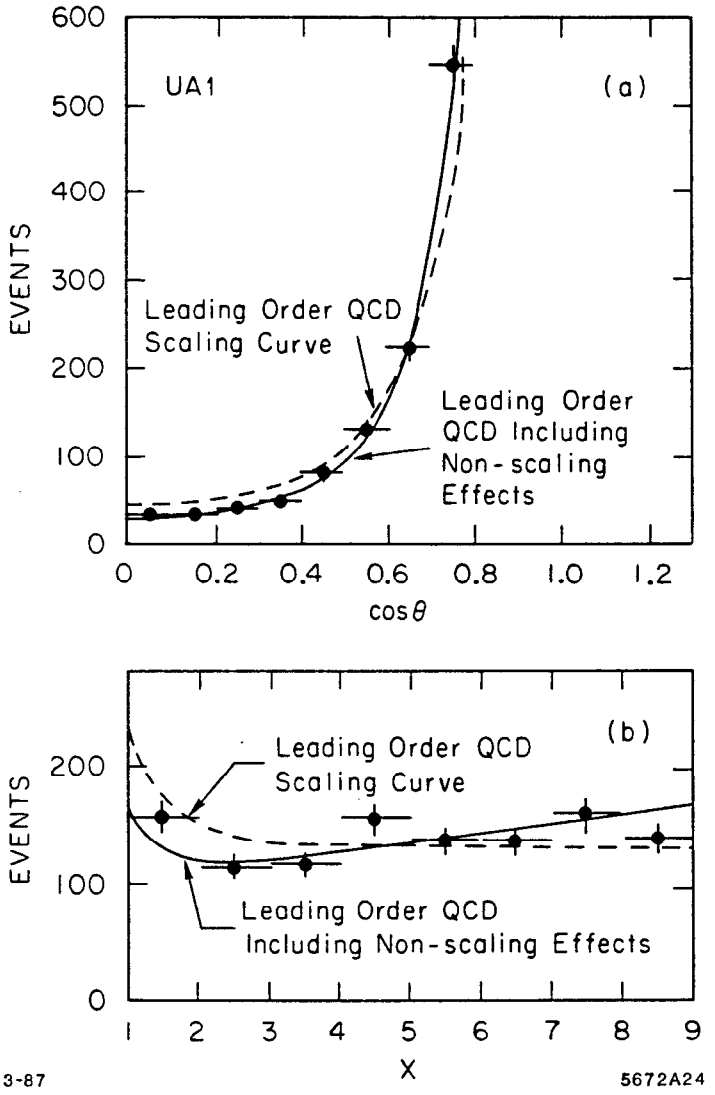

Fig. 46. (a) The 2-jet angular distribution as a function of $\cos\theta$ and (b) as a function of $x = (1 + cos\theta)/(1 - cos\theta)$. The dashed curves show the leading order QCD prediction, the solid line the leading order QCD prediction including the non-scaling effects.

cesses have a very similar angular distribution (see Equation 5), the result is not very sensitive to the relative subprocess weights. The data are clearly incompatible with the scaling curve, whereas the leading order QCD, including non-scaling effects, gives excellent qualitative agreement with the data. One can imagine that with time this could be fashioned into a quantitative test by measuring α_s as it enters through (5).

Data on 3-jet events is available from AFS,[46] UA1[47] and UA2.[48] For three final state, massless partons at fixed subprocess $\sqrt{\hat{s}}$, the parton configuration is specified by four independent variables. The leading order QCD prediction for a subprocess cross section is given by

$$\frac{d^4\sigma}{dx_1 dx_2 dcos\theta_1 d\psi} = (\frac{1}{32\pi^2}) \mid M \mid^2$$

with

$$\mid M \mid^2 \approx (\alpha_s^2/\hat{s})\{x_{T_1}^2 x_{T_2}^2 x_{T_3}^2 (1-x_1)(1-x_2)(1-x_3)\}^{-1}. \qquad (6)$$

The kinematics are defined in Fig. 47 where x_i are the energies of the three outgoing partons (with $x_1 > x_2 > x_3$) scaled to $\sqrt{\hat{s}}$, $x_{T_i} = x_i sin\theta_i$, and the angle θ_1 and ψ are most easily understood by looking at Fig. 47. Because of the singular nature of $\mid M^2 \mid$ as $x_i \to 1$ or $x_{T_i} \to 0$, experimental cuts must be made to ensure well separated 3-jet events. We will omit here a discussion of the cuts made by the three groups to isolate the 3-jet events. The interested reader is encouraged to consult Ref. 46. As is typical, each group uses somewhat different cuts and variables to display their data. For our purpose, which is to establish that leading order QCD can account for the qualitative features of the data, this is not significant.

The UA1 data are shown in Figs. 48 and 49. Figure 48 shows the 3-jet Dalitz plot variables x_1 and x_2 which are sensitive to the final state gluon radiation (see Fig. 41(b)). The solid lines are the prediction of leading order QCD (suitably weighted for each subprocess), while the dashed lines are for a phase space model.

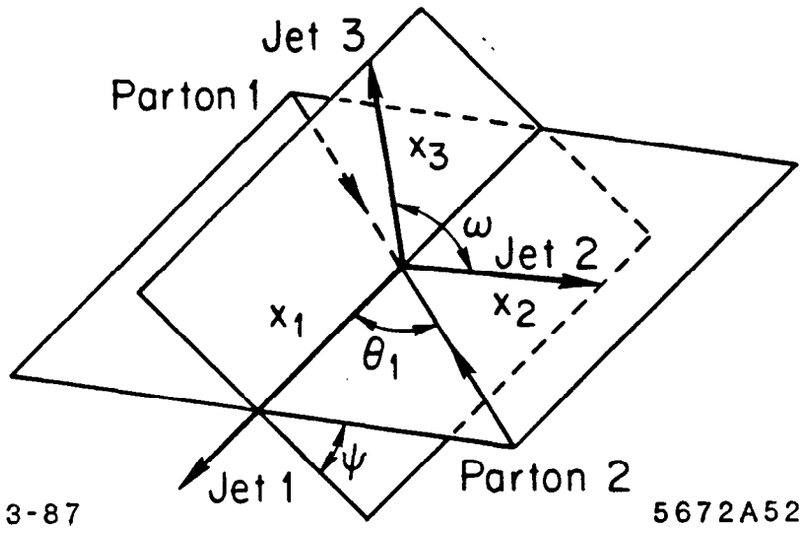

Fig. 47. The 3-jet variables as defined in the 2→3 subprocess rest frame.

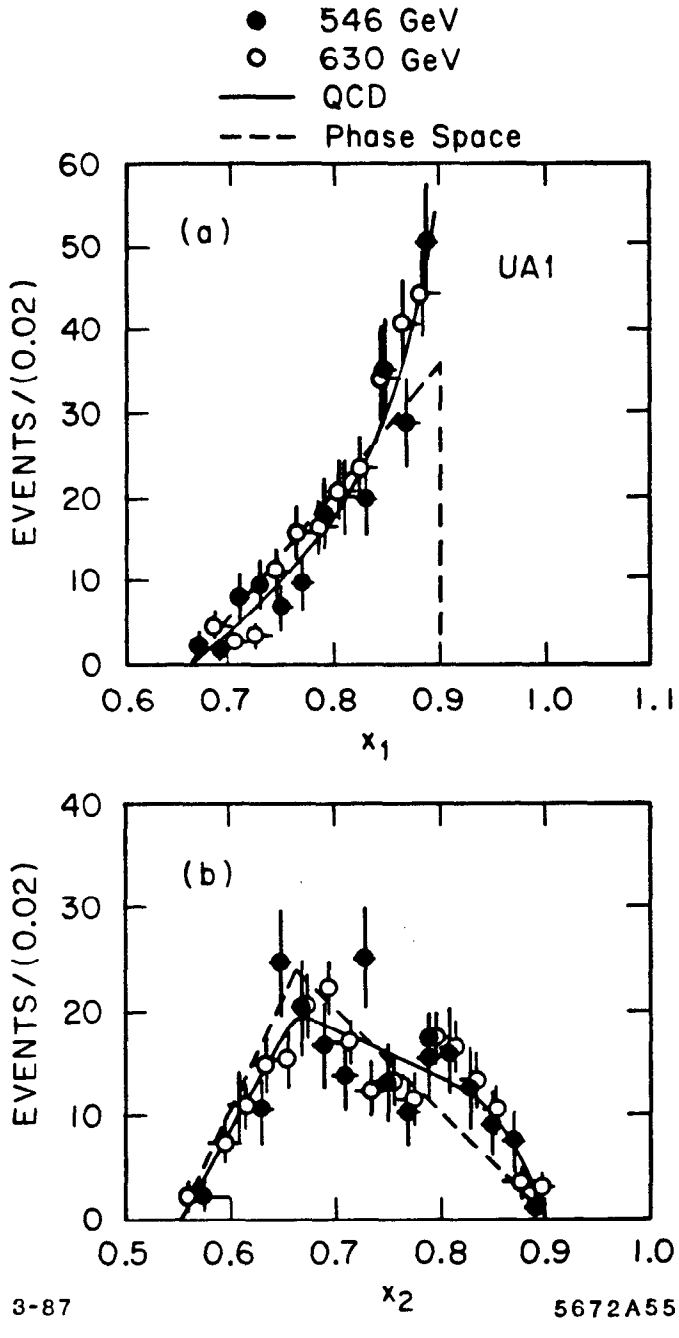

Fig. 48. UA1 3-jet Dalitz plot distributions. The solid lines are the prediction of leading order QCD, the dashed lines a phase space model.

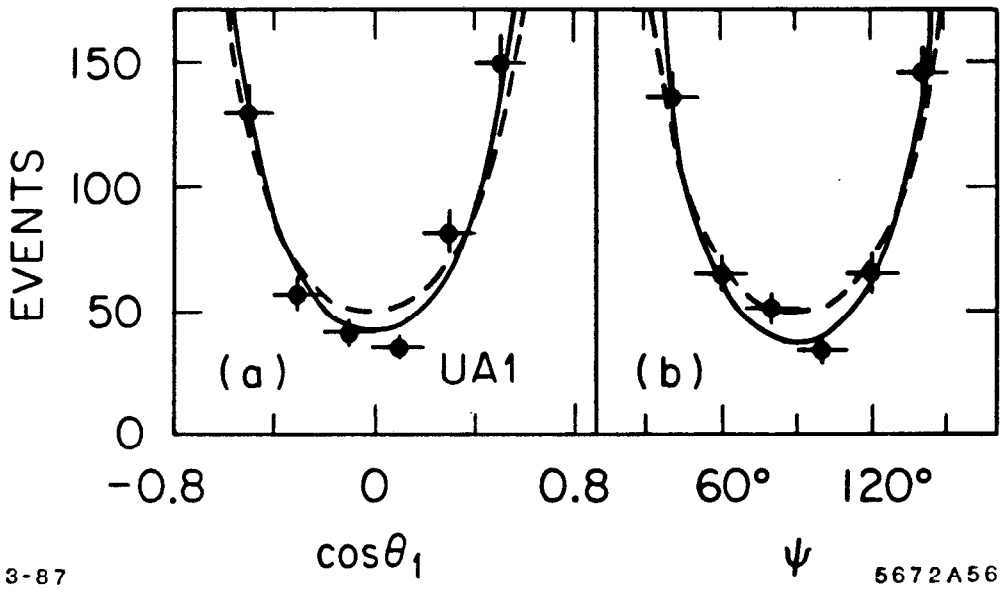

Fig. 49. UA1 3-jet angular distributions. The solid (dashed) line is the QCD prediction including (not including) scale breaking effects.

Figure 49 shows the 3-jet angular distributions which are especially sensitive to initial state gluon radiation. The curves are the prediction of leading order QCD with and without the non-scaling effects. The qualitative agreement between the predictions of leading order QCD and the data are good.

The UA2 data are shown in Figs. 50 and 51. Figure 50 shows the distribution of the angle w which is the angle between jets 2 and 3 as defined in Fig. 47. The predictions of leading order QCD and a phase-space model are shown. Figure 51 shows the Dalitz plot variables x_{23} and x_{12} where x_{ij} is the square of the invariant mass of jets i and j normalized to $\sqrt{\hat{s}}$. The solid (dashed) curve is the prediction of leading order QCD (phase-space model). As with the UA1 data leading order QCD does a good job of describing the qualitative features of the 3-jet events; a phase-space model fails to reproduce the data.

Three-jet events are also observed at the ISR as discussed in Ref. 46 by the AFS group. Figure 52 shows the Dalitz plot variables for the 3-jet events, normalized to the yield of 2-jet events. Appropriate ω and x_3 cuts are made to ensure well separated 3-jet events. The data are corrected for the finite size of the rapidity interval for the jets, namely the ratio of cross sections is evaluated at $\eta = 0$. The actual quantity plotted in Fig. 52(a) is

$$\frac{dN^{3jets}}{dw d\eta_1 d\eta_2 d\eta_3/\eta_{i=0}} \Big/ \frac{dN^{2jets}}{d\eta_1 d\eta_2/\eta_{i=0}}$$

and in Fig. 52(b) the variable ω is replaced by x_3. Also shown on the figure are the parton level lowest order QCD predictions (solid lines), the Monte Carlo predictions (shaded bands) and the Monte Carlo with the multi-jet events removed. One sees good qualitative agreement with QCD and a clear need for multi-jet production. The AFS group uses the events with $x_3 > 0.4$ and $w > 60^\circ$ for quantitative studies and, as discussed in the next section, to extract α_s. For these events the energy flow is shown in Fig. 53 where the data is compared with the Monte Carlo (modified ISAJET). The agreement is rather impressive indicating that the QCD lowest order simulation accounts well for the AFS data.

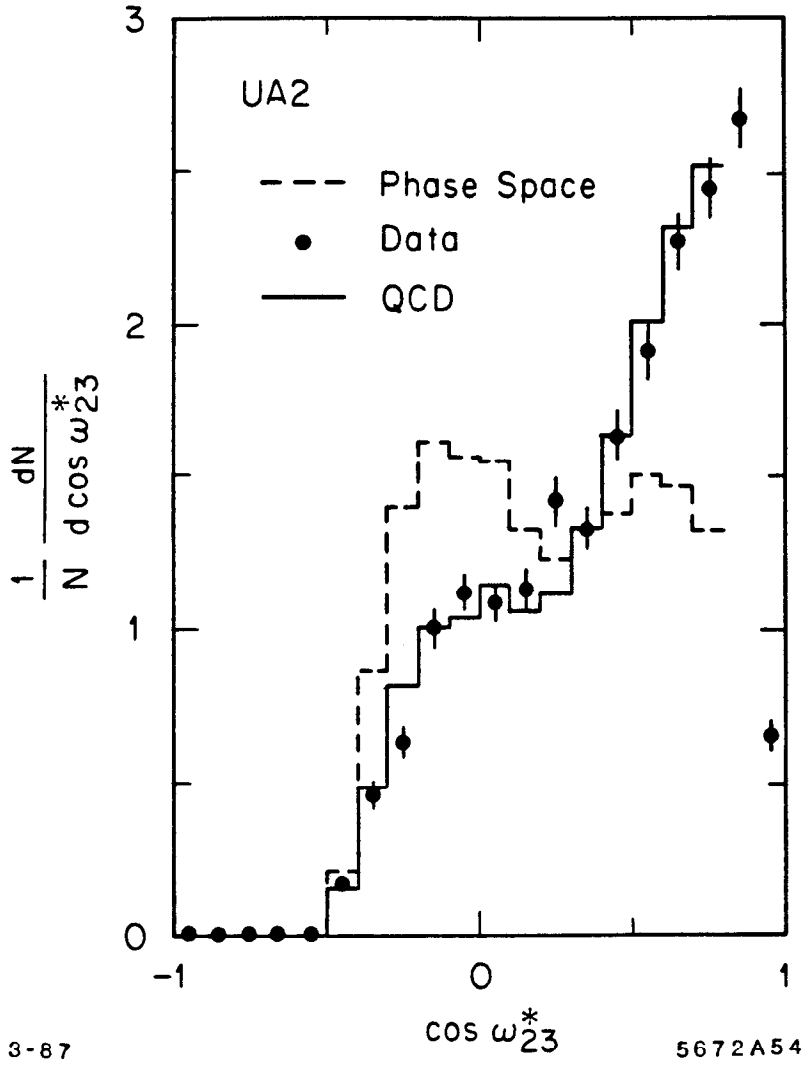

Fig. 50. UA2 data on the angle between the two least energetic jets in 3-jet events. The predictions of leading order QCD and a phase space model are shown.

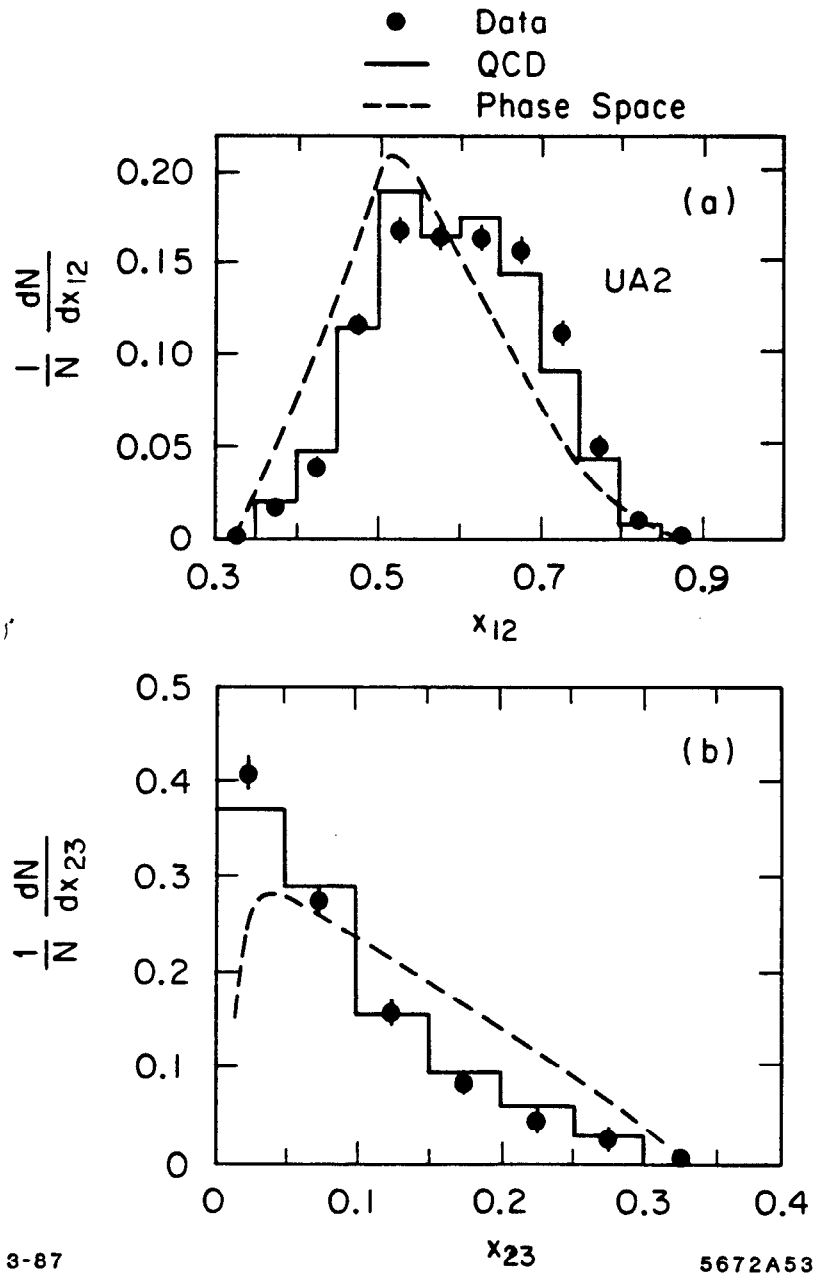

Fig. 51. UA2 3-jet Dalitz plot distributions. The curves are for leading order QCD (solid) and a phase space model (dashed).

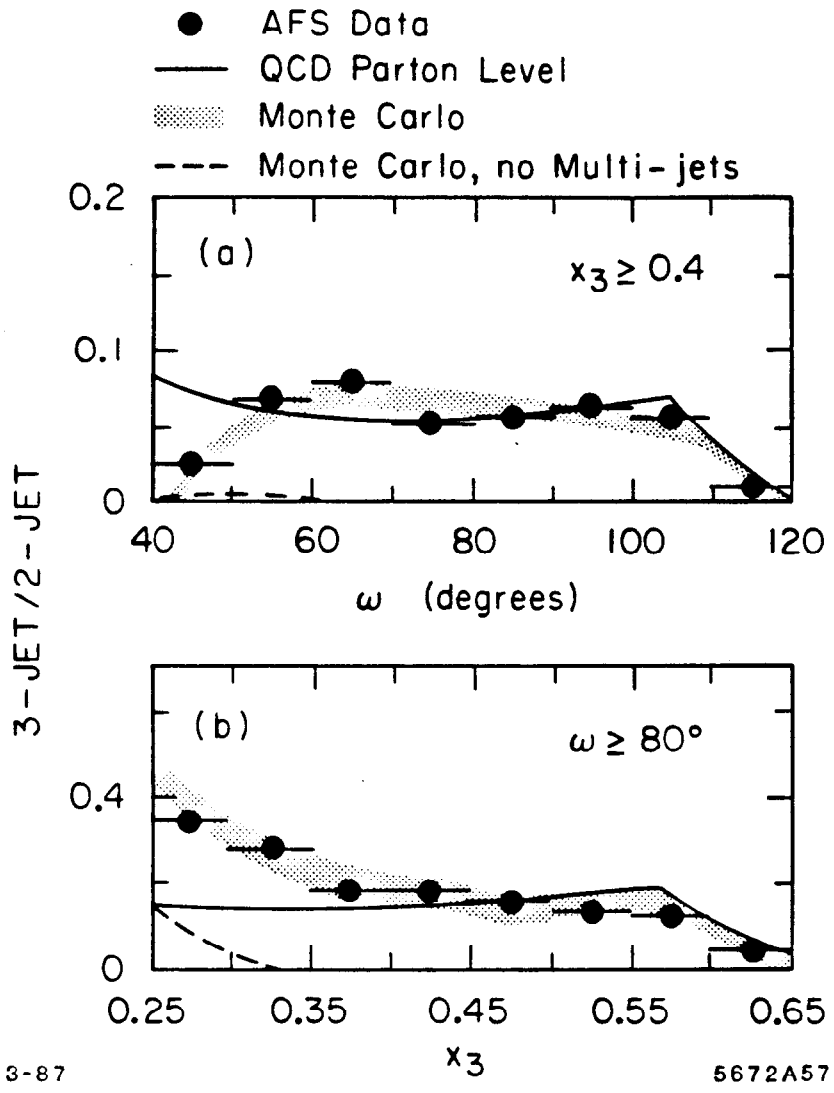

Fig. 52. The distribution of Dalitz plot variables ω and x_3 in 3-jet events. The data are corrected for trigger and filter inefficiencies and for the finite size of the rapidity gap. The yield of 3-jet events is shown normalized to 2-jet yield as described in the text. The solid line gives the lowest order QCD prediction at the parton level, the shaded bands are the Monte Carlo predictions and the dashed line the Monte Carlo with the multi-jets removed.

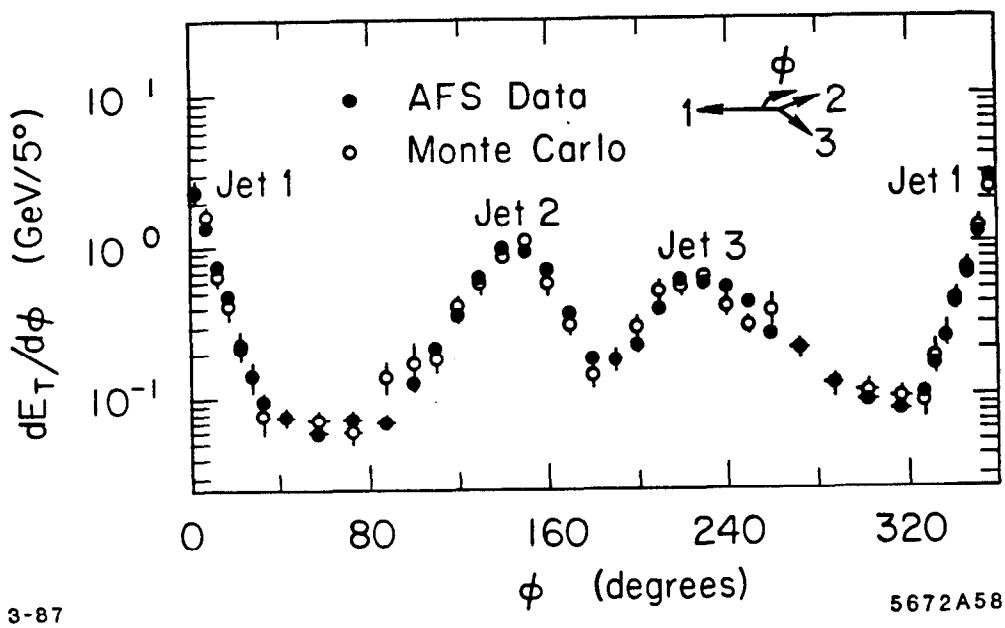

Fig. 53. The energy flow in 3-jet events as a function of the angle relative to the fastest jet. Only jets with $|\eta| < 0.7$ are included. The predictions of the Monte Carlo simulation are shown, where the data and simulation are subject to the same detector biases.

3.3 QUANTITATIVE TESTS OF QCD; MEASUREMENT OF α_s

From Equations (5) and (6) we see that if scaling holds, the 2- and 3-jet cross sections at fixed subprocess energy are given by energy-independent, dimensionless variables. In this limit, the 2- and 3-jet cross sections have the same energy dependence and the ratio will yield a number proportional to α_s:

$$\sigma_{2J} = C_{2J}\alpha_s^2 \qquad \sigma_{3J} = C_{3J}\alpha_s^3$$

where C_{2J}, C_{3J} are calculable numbers which depend on the detector cuts and the relative subprocess abundances. Just as for 2-jet subprocesses, the 3-jet subprocess C_{3J} values for gg, qg and qq vary approximately as $1{:}4/9{:}(4/9)^2$. This means that to reasonably good approximation C_{3J}/C_{2J} is a constant roughly (within 20%) independent of the combination of interacting partons. Of course, life is not so simple (as we have already seen, scaling does not hold) and in reality to lowest order in QCD

$$\sigma_{3J}/\sigma_{2J} = [\alpha_s^3(Q_{3J}^2)/\alpha_s^2(Q_{2J}^2)]$$

$$[F(x_1,Q_{3J}^2)F(x_2,Q_{3J}^2)/F(x_1,Q_{2J}^2)F(x_2,Q_{2J}^2)][C_{3J}/C_{2J}]. \qquad (7)$$

A priori, the Q^2 scale for the 3-jet and 2-jet events is unknown which makes the α_s determination from (7) yet more difficult. Figure 54(a) shows the measured ratio of 3-jet and 2-jet cross sections as a function of $\hat{s}$ (from UA1). The solid line is the lowest order QCD prediction for $Q_{3J}^2 = Q_{3J}^2$ the dashed line the (intuitive ?) choice of $Q_{3J}^2 = \frac{2}{3}Q_{2J}^2$. The latter choice appears to fit the data better. Figure 54(b) shows the variation of the 3- to 2-jet ratio as a function of the multijet mass (UA2). The solid curve is the prediction of QCD and the dashed lines indicate the systematic plus statistical errors. Notice in both Figs. 54(a) and 54(b) the data are consistent with the "running" of α_s predicted by the lowest order QCD. However, the data are also consistent with no "running."

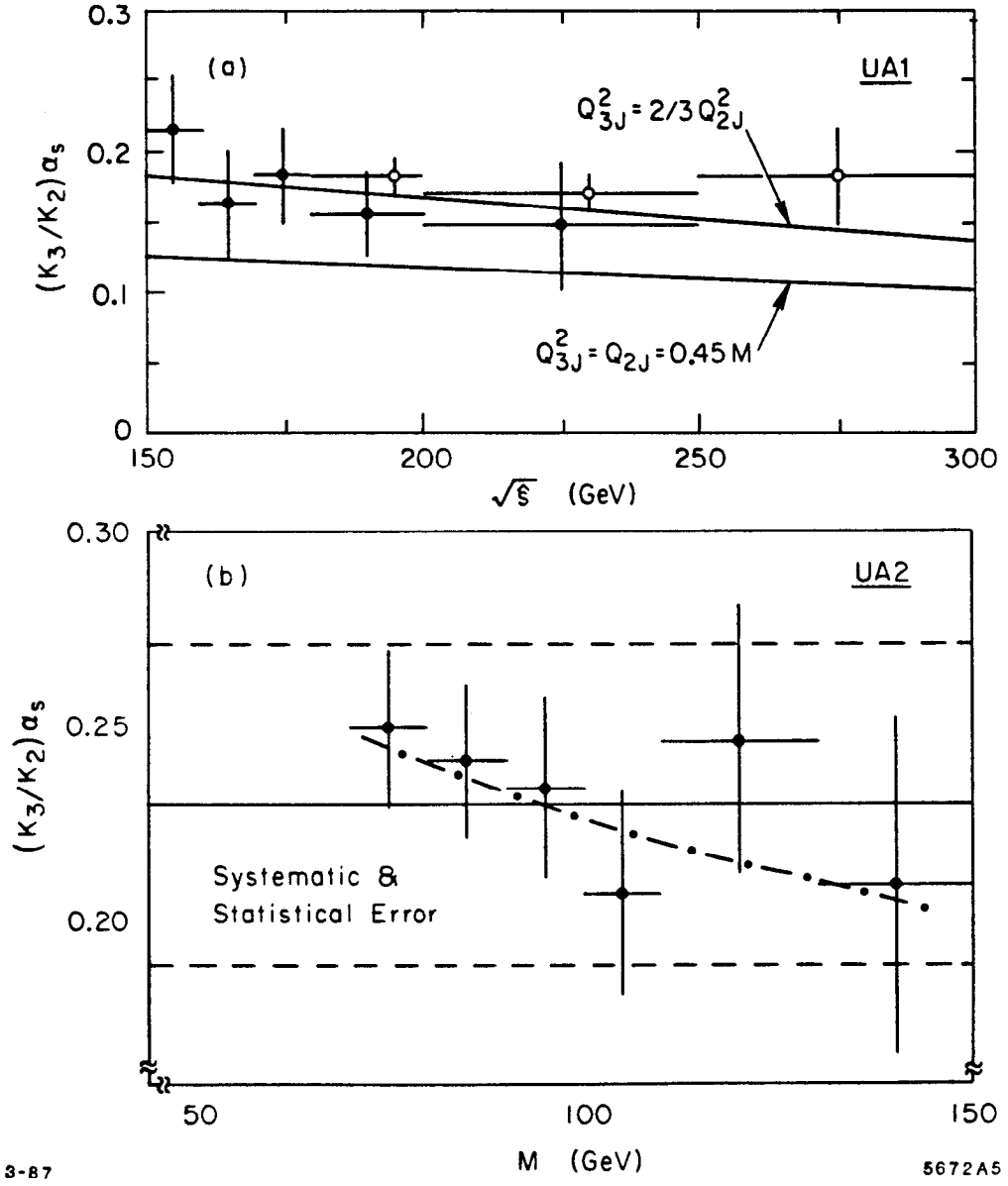

Fig. 54. a) Ratio of the 3-jet to 2-jet cross sections as a function of subprocess center- of-mass energy (UA1). The lines correspond to the QCD prediction for different choices of Q^2. b) $\alpha_s(K_3/K_2)$ as a function of multi-jet mass from UA2. The prediction of QCD is shown along with the range of the errors.

So we see that the measurement of α_s in $\bar{p}p$ collisions is plagued by problems, mostly theoretical in nature. We bury these theoretical uncertainties in K factors and quote results for $\alpha_s(K_3/K_2)$ where K_3/K_2 accounts for the differences in the Q^2 scales for the 2- and 3-jet events and the non-scaling effects. The results from UA1 and UA2 are (see Refs. 47 and 48)

$$UA1: \quad \alpha_s(K_3/K_2) = 0.23 \pm 0.01 \pm 0.04 \qquad < Q^2 > \approx 4000\ GeV^2$$

$$UA2: \quad \alpha_s(K_3/K_2) = 0.23 \pm 0.01 \pm 0.04 \qquad < Q^2 > \approx 1700\ GeV^2$$

That the numbers are identical is not a careless error, but indeed true. However this is an accident and in fact the two numbers do not measure the same quantity. The main difference arises from the fact that the Q^2 definitions differ. UA1 uses an average Q^2 identical for the 2-jet and 3-jet samples, namely $< Q_{2J}/M_{2J} > = < Q_{3J}/M_{3J} > = 0.45$, whereas UA2 uses a definition which leads to a softer 3-jet Q^2 namely $< Q_{2J}/M_{2J} > = 0.48$ and $< Q_{3J}/M_{3J} > = 0.41$. In an attempt to measure the effect of the ambiguity of the Q^2 scale in the measurement of $(K_3/K_2)\alpha_s$, UA1 has made a jet selection which would satisfy the criteria $< Q_{3J} > \approx \frac{2}{3} < Q_{2J} >$ and find

$$\alpha_s(K_3/K_2) = 0.16 \pm 0.02 \pm 0.03.$$

The implication here is that for such a choice, (K_3/K_2) better approximates unity. This reminds us then that the ambiguity in the choice of Q^2 scale cannot be resolved until the higher order QCD corrections are calculated.

The AFS collaboration (see Ref. 46) have also extracted a value for α_s and find

$$AFS: \quad \alpha_s(K_3/K_2) = 0.18 \pm 0.03 \pm 0.04 \qquad < Q^2 > \approx 300\ GeV^2$$

in relatively good agreement with the $\bar{p}p$ results. Intrinsic differences in the three measurements are discussed at length in Ref. 46.

It is clear that the quantitative measurement of α_s in $p\bar{p}$ and pp collisions is in its infancy. We should remember the lessons of e^+e^- experiments, where both the experimental and theoretical environments are simpler, and where it has taken about six years of work to extract reliable measurements of α_s. I find the progress in the hadron collider measurements impressive and look forward to improvements in the future.

4. Measurements of α_s from Υ Decays

The decays of heavy quarkonium states provide tests of QCD. The dominant decay mode is into three gluons as shown in Fig. 55. In principle one could measure α_s from this decay, for example from $\Upsilon \rightarrow$ Hadrons. However in practice such a measurement has limited precision because of an incomplete understanding of the non-perturbative contribution involving the quark wave functions. To remove this uncertainty one evaluates rather the ratio of the two similar processes $\Upsilon \rightarrow ggg$ and $\Upsilon \rightarrow \gamma gg$. This ratio is calculable in first order QCD, and as is pointed out by Brodsky, LePage and MacKenzie,[49] a natural choice of $Q^2 = 0.157 M_\Upsilon$ leads to small higher order corrections and the prediction

$$B_\gamma = \frac{\Gamma(\Upsilon \rightarrow \gamma gg)}{\Gamma(\Upsilon \rightarrow ggg)} = \frac{36 q_b^2}{5} \frac{\alpha}{\alpha_s(\overline{MS})} \{1 + (2.2 \pm 0.6) \frac{\alpha_s(\overline{MS})}{\pi}\}$$

where α is the fine structure constant and q_b is the charge of the b quark $(-\frac{1}{3})$. This prediction for the measurement of α_s at $Q^2 = 0.157 M_\Upsilon$ is considered to be on a sound theoretical footing. The measurement has been done by two groups, CLEO[50] and CUSB,[51] both running at CESR. The measurement is by no means simple since there is a large background from non-direct photons coming from decays of π^0's and η's. At small photon energies, $x \lesssim 0.5$ (where $x = 2E_\gamma / M_\Upsilon$) the photon spectrum is dominated by this source. For $x \gtrsim 0.5$ the dominant background is from continuum processes (i.e., non-resonant production) and the decay $\Upsilon \rightarrow q\bar{q}$. The QCD spectrum in contrast is expected to

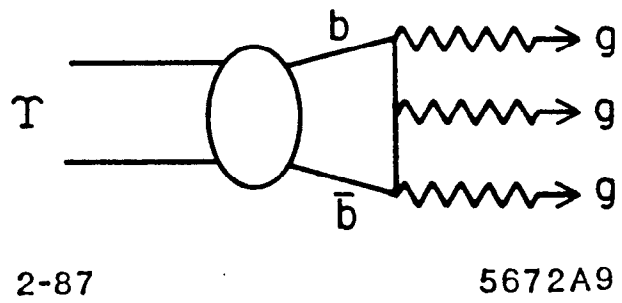

Fig. 55. The decay $\Upsilon \rightarrow ggg$.

rise linearly from $x = 0$ to $x = 1$, although radiative corrections will provide a smooth turnover as $x \to 1$.

The two groups use very different techniques for obtaining the direct photon spectrum. In addition to the Υ decay, CUSB also measures the rate for $\Upsilon' \to \gamma gg$. The CLEO group makes a measurement of the photon spectrum using their shower counters and makes the subtraction for π^o's using the measured $\pi^{\pm}(= 2\pi^o)$ and π^o x distributions. CUSB on the other hand obtains the direct photon yield from a statistical separation relying on the difference of the conversion probability of π^o's (i.e., two photons) and direct photons. The ingredients for the algorithm are checked directly using annihilation events of the type $e^+e^- \to \gamma\gamma$. Both groups remove contributions from the continuum using data taken below the Υ and also a contribution from $\Upsilon \to q\bar{q}$. Figure 56(a) shows the CLEO observed photon spectrum and the background contributions discussed above. Figure 56(b) shows the background subtracted direct photon signal, where the errors are statistical only. Below x of 0.5, large backgrounds preclude a meaningful measurement. Also shown in Fig. 56(b) are the fits to three theoretical spectra; the solid line for lowest order QCD, the dotted line for a calculation of Photiadis[52] accounting for higher order QCD effects, and the dashed line a cluster model Monte Carlo simulation due to Field[53] which accounts for hadronization effects. The χ^2 for the three fits are 14.2, 10.8 and 8.1, respectively, for 11 degrees of freedom. Comparison of the three model predictions points out a major systematic problem with this measurement, namely estimating the magnitude of the unseen portion of the photon spectrum. This problem shows up quite dramatically in the extracted branching fractions as seen in Table VII.

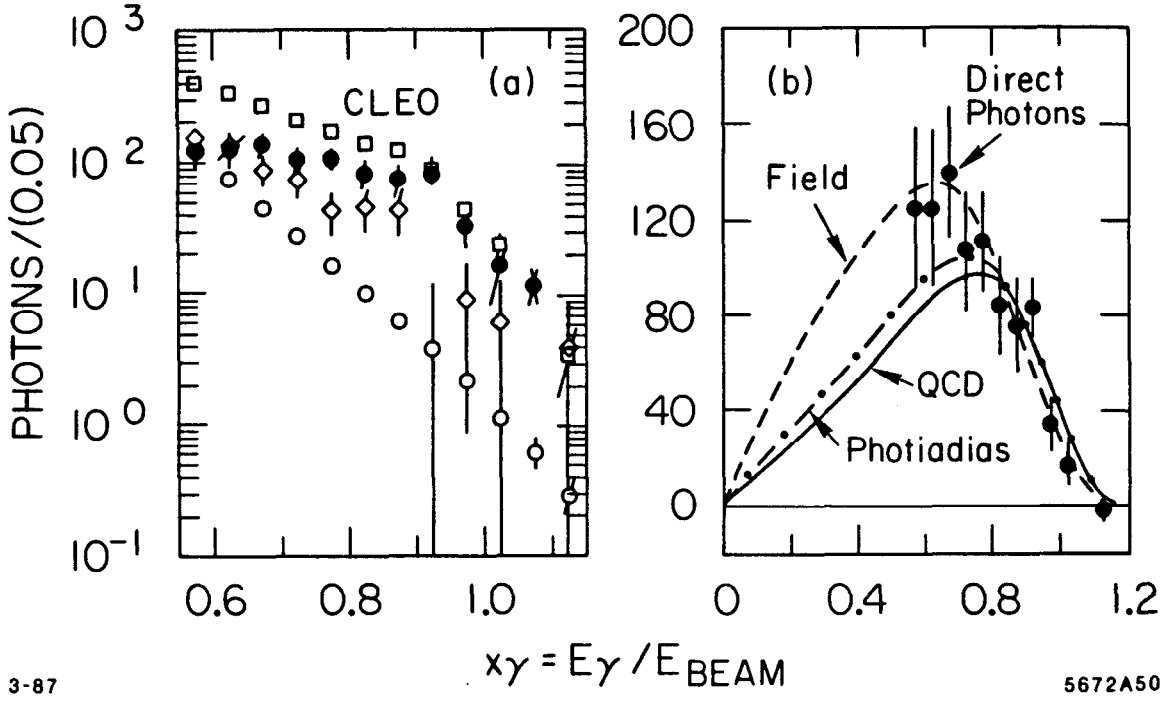

Fig. 56. a)The CLEO measured photon spectrum (open squares) and the contributions from the various background sources: continuum and $\gamma \rightarrow qq$ (open diamonds) and π^o and η^o (open circles). The solid points are the background subtracted direct photon spectrum also shown in b) along with fits to the indicated models. The errors are statistical only.

Table VII

EXPT	Model	$B_\gamma(\%)$	$\alpha_s(Q = .157M_\Upsilon)$	$\Lambda_{\overline{MS}}$(GeV)
CLEO (Υ)	QCD	1.88±0.14±0.17	$0.40^{+0.04+0.06}_{-0.03-0.05}$	$0.37^{+0.05+0.07}_{-0.05-0.06}$
CLEO (Υ)	Photiadis	2.03±0.15±0.16	$0.36^{+0.04+0.04}_{-0.03-0.04}$	$0.32^{+0.05+0.06}_{-0.04-0.05}$
CLEO (Υ)	Field	2.54±0.18±0.14	$0.27^{+0.03+0.03}_{-0.02-0.02}$	$0.19^{+0.04+0.04}_{-0.03-0.03}$
CUSB(Υ)	QCD	2.99±0.59	$0.226^{+0.067}_{-0.042}$	$0.116^{+0.105}_{-0.057}$
CUSB(Υ)	QCD	3.37±1.14	$0.197^{+0.123}_{-0.055}$	$0.080^{+0.195}_{-0.059}$

The CUSB direct photon spectra for the Υ and Υ' are shown in Fig. 57 along with a fit to the spectrum $x(1-x)^a$, where a is found to be 0.17±0.05. Normalizing to the number of resonant hadronic events yields the numbers given in Table VII.

We began this chapter by noting that we had a solid QCD prediction for $B_\gamma = \Gamma(\Upsilon \to \gamma gg)/\Gamma(\Upsilon \to ggg)$. Unfortunately the results coming from the two experiments are in poor agreement indicating that there are still some unresolved experimental problems. Possibly the Crystal Ball and/or ARGUS groups at DESY could shed some light on this situation in the future.

5. Testing QCD in Deep Inelastic Lepton Scattering

Leptons being pointlike, structureless particles make excellent probes of nucleon structure (see Fig. 58). We have gained enormous insight into nucleon structure from the wealth of beautiful data from e, μ, and νN scattering experiments. I will do this magnificent experimental effort poor justice by the shortness of my remarks, the simplification of the problems and their solutions and my selective choice of data. However, this format does not permit much more than is presented with the main emphasis being placed on demonstrating the ability of QCD to explain the non-scaling behavior (i.e., departure for QPM) and the

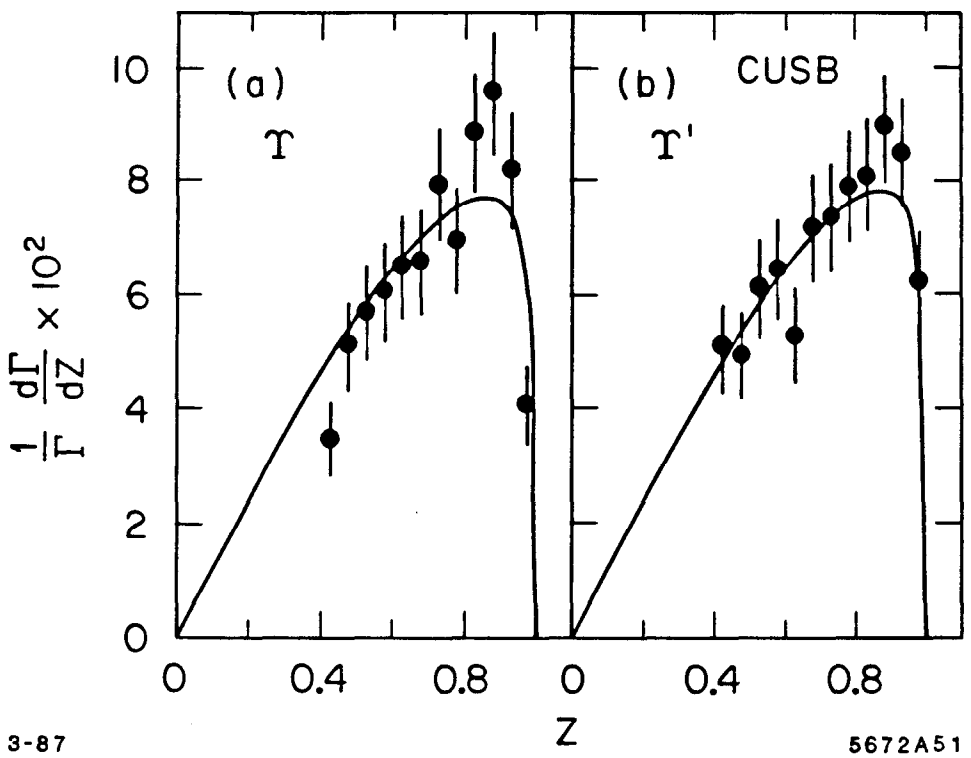

Fig. 57. Acceptance corrected direct photon spectrum from CUSB for $\Upsilon(a)$ and $\Upsilon'(b)$. The errors are statistical only. The curve is a fit to the function $x(1-x)^a$.

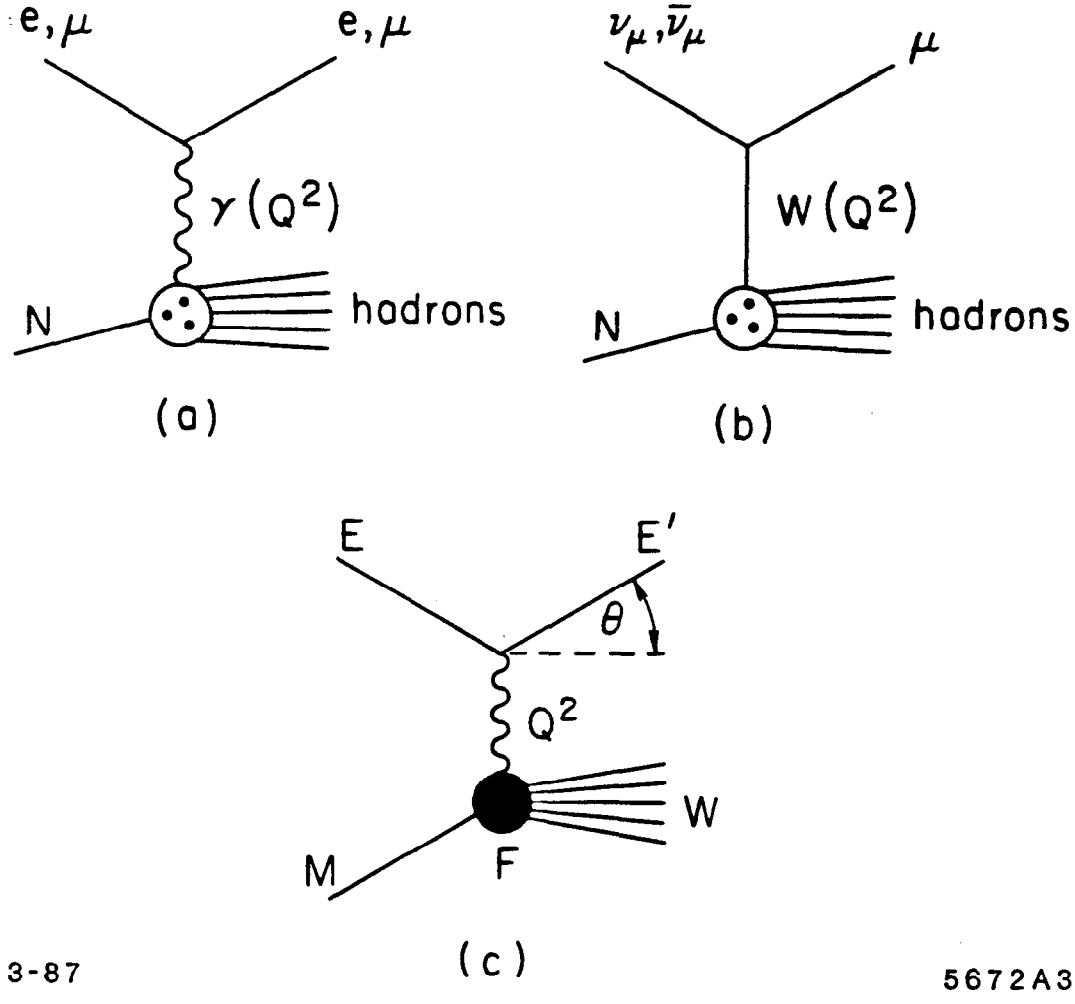

Fig. 58. Probing the nucleon structure using pointlike leptons via the electromagnetic and weak interactions.

extraction of Λ. For completeness a few (among many) references,[54] far more complete than this discussion, are given.

One is able to achieve an impressive Q^2 range with lepton probes. Figure 59 illustrates the various regimes in which increasingly more sensitive tests become possible. At the lowest $Q^2 \approx 0.1\text{GeV}^2$ one studies elastic eN scattering and the gross nucleon structure is sensed. Raising Q^2 to ≈ 1 GeV^2 permits a "deep" enough probe that partons are discerned within the nucleon and scaling behavior of the structure functions is observed. At this level the data can be accommodated by a QPM picture. However, with increasing magnification the gluonic component of the nucleon is more readily seen and departures from the QPM picture are measurable. Scaling breaks down and QCD does a very good job of qualitatively explaining the data. As with all the previous discussions, a quantitative extraction of Λ turns out to be difficult, but a relatively narrow range of $\Lambda = (200 \pm 100)$ MeV encompasses the most reliable measurements.

The kinematics of deep inelastic lepton scattering are shown in Fig. 58(c) where E, E$'$ are the energy of the incoming and outgoing lepton, θ is the lepton scattering angle, Q^2 the four momentum transfer, W the mass of the nucleon fragments and the structure function F contains our a priori ignorance about the structure of the nucleon. For the case of eN or μN scattering there are two-structure functions F_1, F_2 and the differential cross section is given by

$$\frac{d^2\sigma}{dxdy} = \frac{4\pi\alpha^2}{Q^4}[F_2(Q^2,\nu)(1-y) + F_1(Q^2,\nu)xy^2]$$

where $Q^2 = 2EE'(1-cos\theta)$, $\nu = E - E'$, $y = \nu/E$ and $x = Q^2/2m\nu$.
The simplest example of evaluating the structure functions is in the QPM where we envisage the nucleon to contain electrically charged, spin$\frac{1}{2}$ objects and we ignore the parton/parton interactions in the scattering process (i.e., impulse approximation, quasi-free constituents). We also assume that the partons have no intrinsic transverse momentum. One obtains then the result that, if $f_i(x_i)$ is

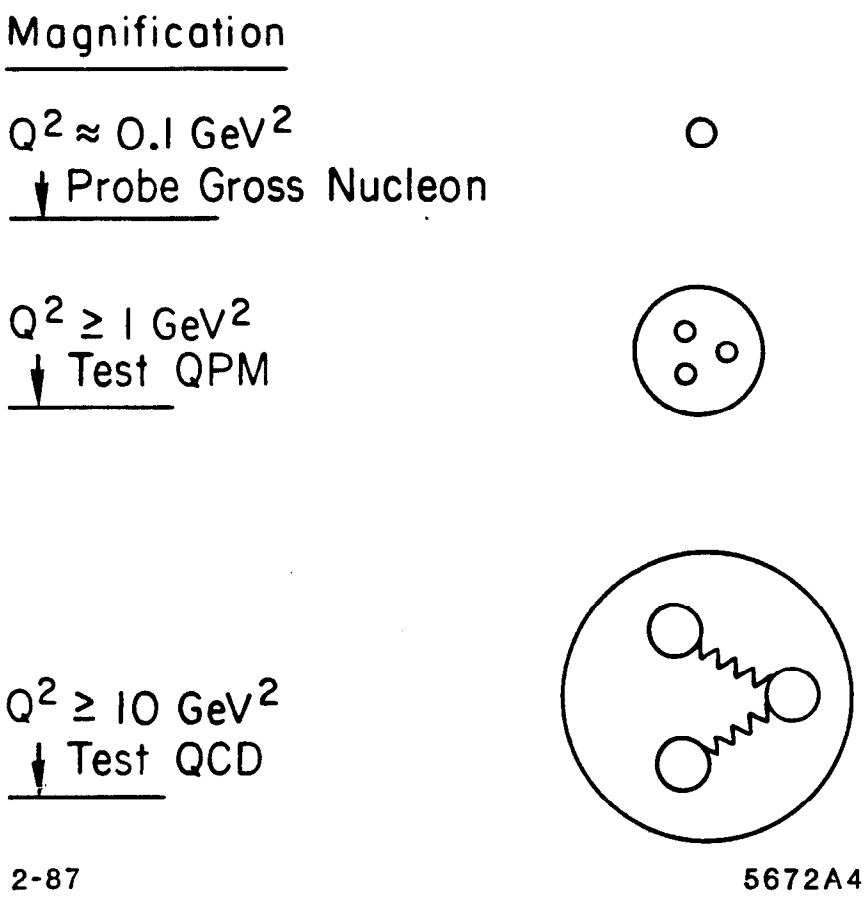

Fig. 59. Cartoon depicting the increased sensitivity to nucleon structure as the magnification (Q^2) of the probe is increased.

the probability for finding parton i with fractional momentum x_i the structure functions are given by

$$F_2(x) = \sum_i e_i^2 f_i(x) x$$

$$2xF_1(x) = F_2(x).$$

In the parton model then as $Q^2, \nu \rightarrow \infty$,"magically" the structure functions become independent of Q^2 at fixed x. This is the mathematical statement of scaling.

The notion of constituent scattering is demonstrated in simplified terms (see Atwood, Ref. 53) in Fig. 60. Low Q^2 elastic ep scattering shows a normalized structure function which peaks at $< x >= 1$ corresponding to one constituent, the gross nucleon. Quasi elastic ed (d=deuterium) scattering (two constituents) has $< x > \approx \frac{1}{2}$ and shows some broadening due to Fermi motion. Finally with large Q^2 one achieves large magnification and the $< x > \approx \frac{1}{3}$ indicative of three charged constituents. The scaling behavior at lowish Q^2 is seen in Fig. 61 which shows the F_2 structure function from SLAC-MIT group ep scattering for data from Q^2 of 2 GeV^2 to 18 GeV^2. In this range the scaling predicted by the OPM holds rather well.

When probing nucleon structure with $\nu(\bar{\nu})$ one gets a third structure function due to the parity violating nature of the $W^{\pm}$ and the cross section can be written as

$$\frac{d^2\sigma^{\nu,\bar{\nu}}}{dxdy} = \frac{G_F^2 ME}{\pi}[F_1(x)xy^2 + F_2(x)(1-y) \pm F_3(x)xy(1-y/2)]$$

where the +(-) is for the $\nu(\bar{\nu})$ probe, and W propagator effects are ignored as they are small ($\lesssim 10\%$ at highest Q^2). For the QPM:

$$2xF_1 = F_2, \qquad xF_3 = \pm F_2$$

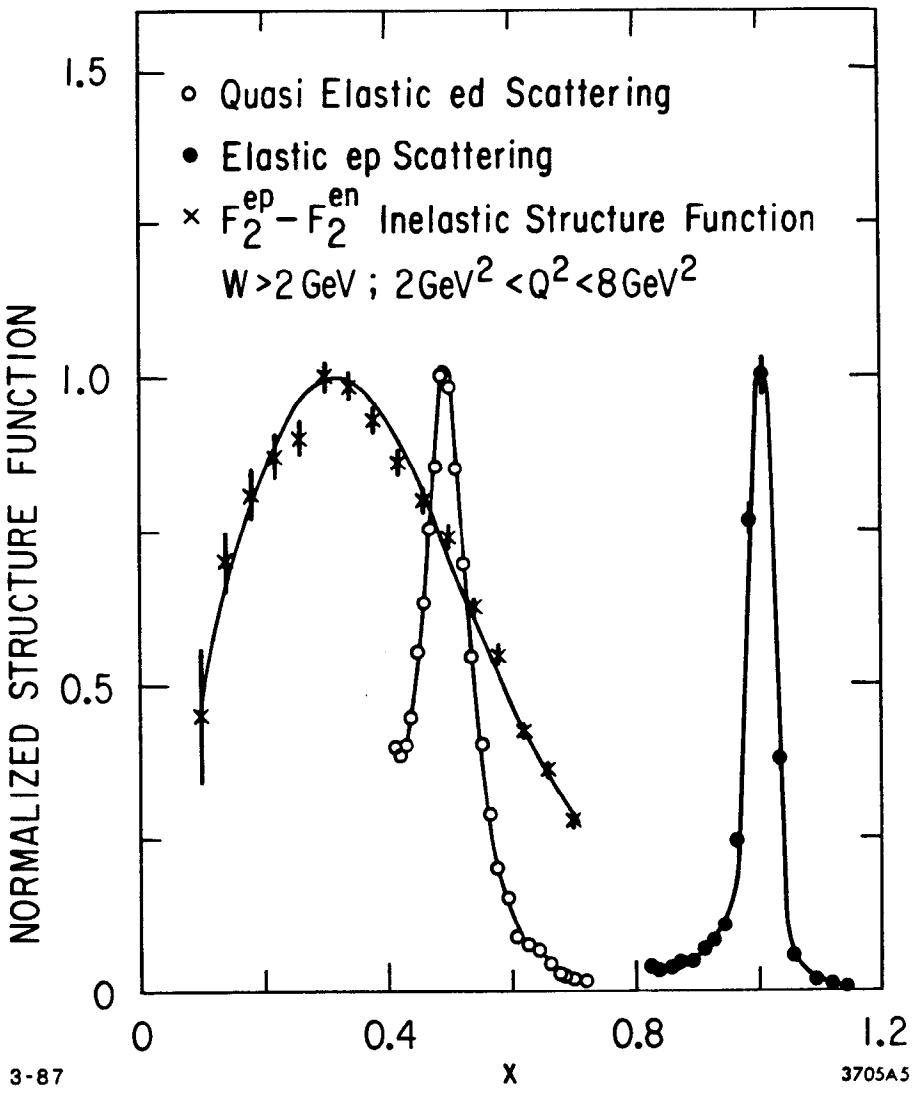

Fig. 60. Examples of the structure function as it relates to the constituent nature of the target being probed.

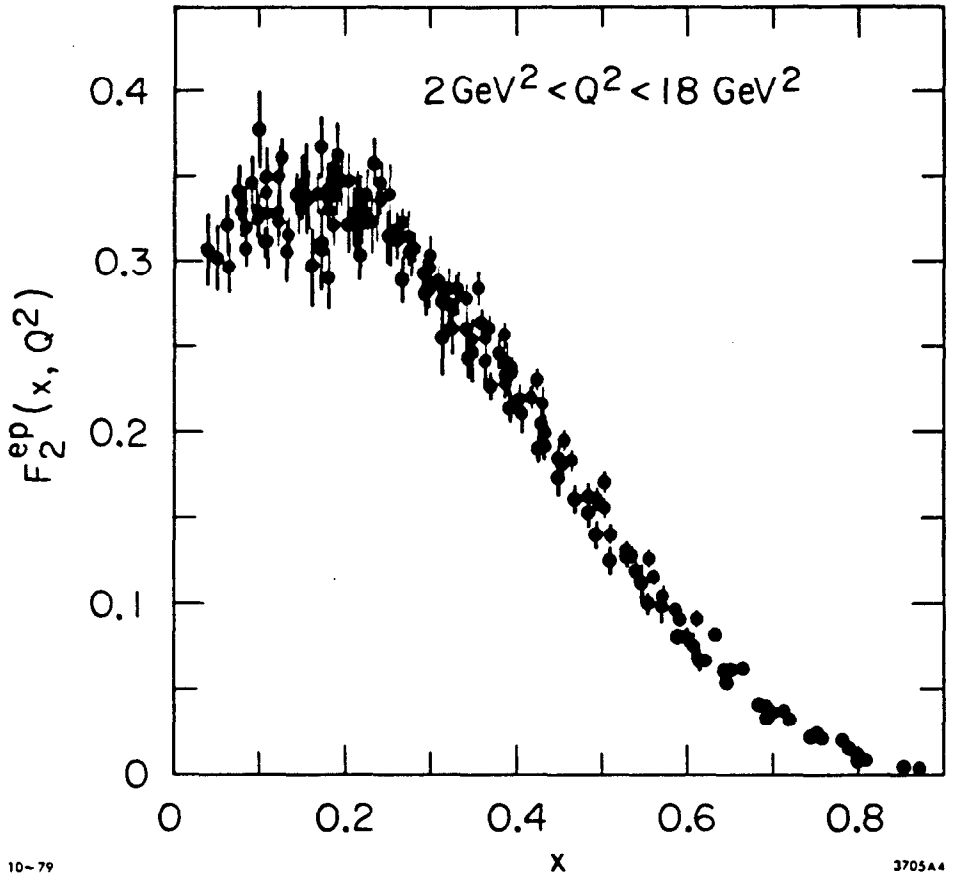

Fig. 61. F_2 structure function as a function of x as measured in ep scattering by the SLAC-MIT group. Over the range of Q^2 indicated in the figure, scaling holds rather well.

and hence,

$$\frac{d^2\sigma}{dxdy}(\nu q) = \frac{G^2ME}{\pi}F_2(x)\{1\}$$

$$\frac{d^2\sigma}{dxdy}(\bar{\nu} q) = \frac{G^2ME}{\pi}F_2(x)\{(1-y)^2\}.$$

We see this qualitative QPM behavior of the scattering from the valence quarks in CDHS νFe and $\bar{\nu}Fe$ data in Fig. 62. One also sees a clear indication of the presence of $q - \bar{q}$ sea quarks. To proceed further and extract meaningful qualitative and quantitative tests of QCD requires loosening the constraints of the QPM model and pushing towards higher Q^2 experiments. It is presumably well known to the reader that simple scaling does not hold and that for sufficiently high Q^2, the structure functions are seen to depend on Q^2 for fixed x. This is illustrated in Fig. 63 for ep, μp, ed and νN scattering. Also if one measures the total momentum carried by the partons, it comprises only half of the nucleon momentum. Hence there must be partons in the nucleon which the electroweak current does not probe. In QCD the presence of gluons can qualitatively account for these effects. They are the unseen "stuff" and the emission of gluons generates transverse momentum for the quarks. This is in direct contrast to the assumption of zero transverse momentum made in the QPM. The presence of gluon emission, visible at sufficiently high Q^2, results in a Q^2 evolution of the structure functions which shows up as scaling violations. In the spirit of Fig. 59, when we raise Q^2 we have an ever-increasing chance of "catching" a quark emitting a gluon and we go from a situation where only the quarks are visible to where the gluons emitted by the quarks are resolvable.

When a gluon is emitted from a quark inside a nucleon the fractional energy, x, of the quark is lowered and it therefore changes the distribution of quark probabilities $f(x)$. As Q^2 increases the $< f(x) >$ of quarks will shift to lower values of x and F_2 will no longer exhibit scaling. This effect is clearly seen in Fig. 63. The evolution of the structure functions with Q^2 is predicted by QCD, and hence QCD can predict the pattern of scale breaking. This is discussed in

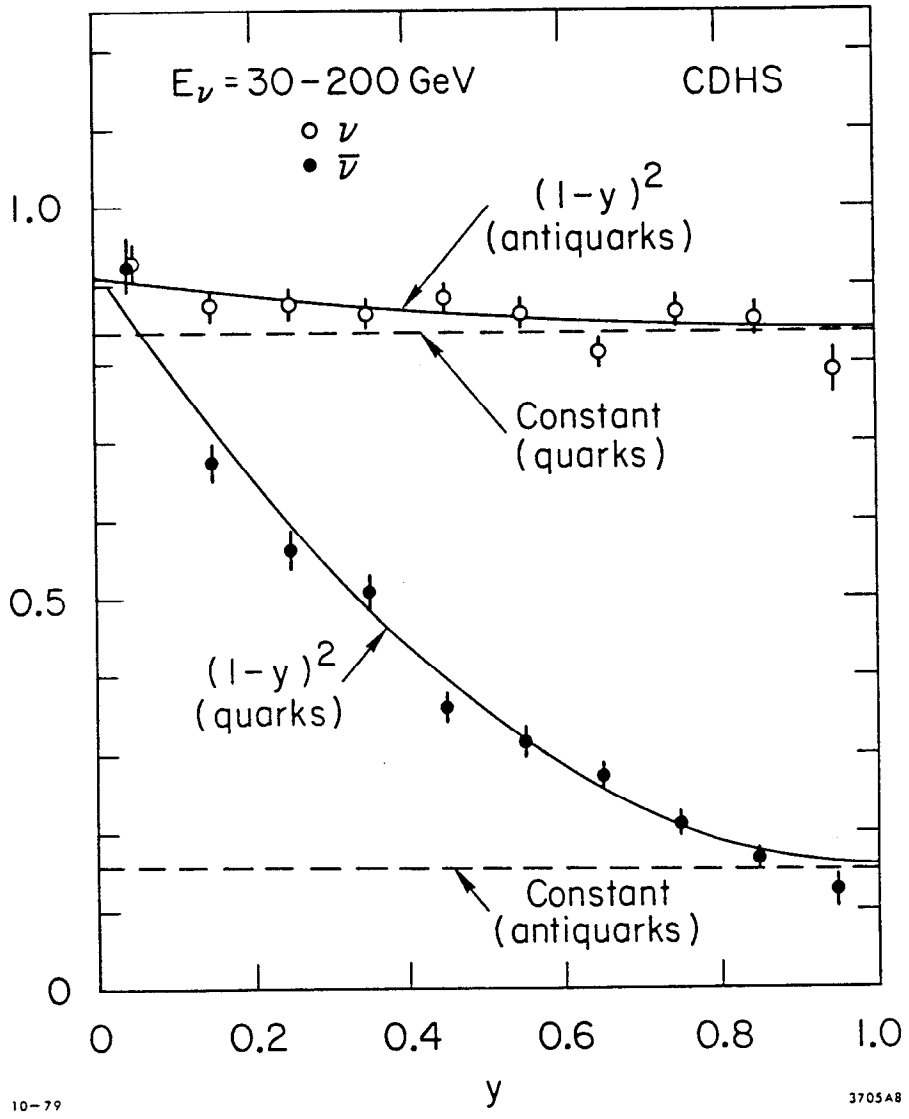

Fig. 62. The cross section for νFe and $\bar{\nu}$Fe collisions as a function of y as measured by the CDHS group. The expected QPM functional form is seen for the scattering from the valence quarks; one sees also contributions from the sea.

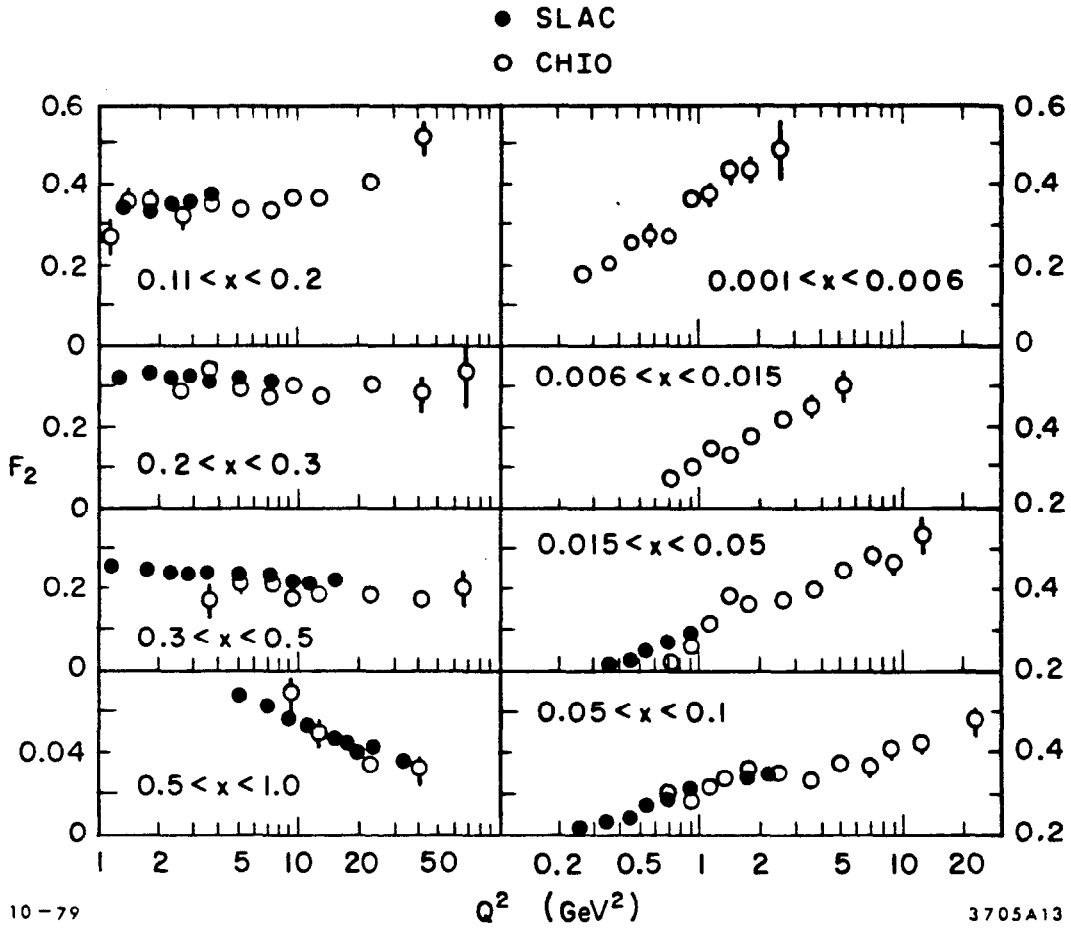

Fig. 63. The change of F_2 with Q^2 in fixed x bins. Clear scaling violations are seen.

detail in the companion lectures of Field and briefly outlined here with reference to Fig. 64. Figure 64(a) depicts the simplest situation involving the evolution of the valence quarks where the only contribution comes from gluon emission from the valence quark. The process whereby the quark with fractional momentum y evolves via the emission of a gluon to a value x is specified by the splitting function P_{qq}. QCD predicts the evolution of q:

$$Q^2 \frac{d}{dQ^2} q^v(x,Q^2) = \frac{\alpha_s(Q^2)}{2\pi} \int_x^1 \frac{dy}{y} q^v(y,Q^2) P_{qq}(x/y)$$

where the splitting function is given by QCD (see Field). The situation with the sea and gluon is somewhat more complicated because there are more than one contributing process (see Fig. 64). But similar expressions can be obtained for the evolution of q^s and g. More germain to our discussion is how this translates into the structure function evolution which is given in terms of the splitting functions P_{qq}, P_{qg} and P_{gg} (all given by QCD) as follows:

$$\frac{dxF_3(x,Q^2)}{d\ell nQ^2} = \frac{\alpha_s(Q^2)}{2\pi} \int_x^1 [P_{qq}(x/z) z F_3(z,Q^2)] \frac{xdz}{z^2}$$

$$\frac{dF_2(x,Q^2)}{d\ell nQ^2} = \frac{\alpha_s(Q^2)}{2\pi} \int_x^1 [P_{qq}(x/z) F_2(z,Q^2) + 2N_f P_{gq}(x/z) G(z,Q^2)] \frac{xdz}{z^2}$$

$$\frac{d\bar{q}^{\bar{p}}(x,Q^2)}{d\ell nQ^2} = \frac{\alpha_s(Q^2)}{2\pi} \int_x^1 [P_{qg}(x/z) \bar{q}^{\bar{p}}(z,Q^2) + N_f P_{gq}(x/z) G(z,Q^2)] \frac{xdz}{z^2}$$

where G is the gluon structure function and N_f is the number of active flavors which will depend on the Q^2 range. The lower Q^2 experiments can safely ignore charm, but this is not true at higher Q^2 and the inclusion of the charm threshold is yet another detail which must be included in the analyses.

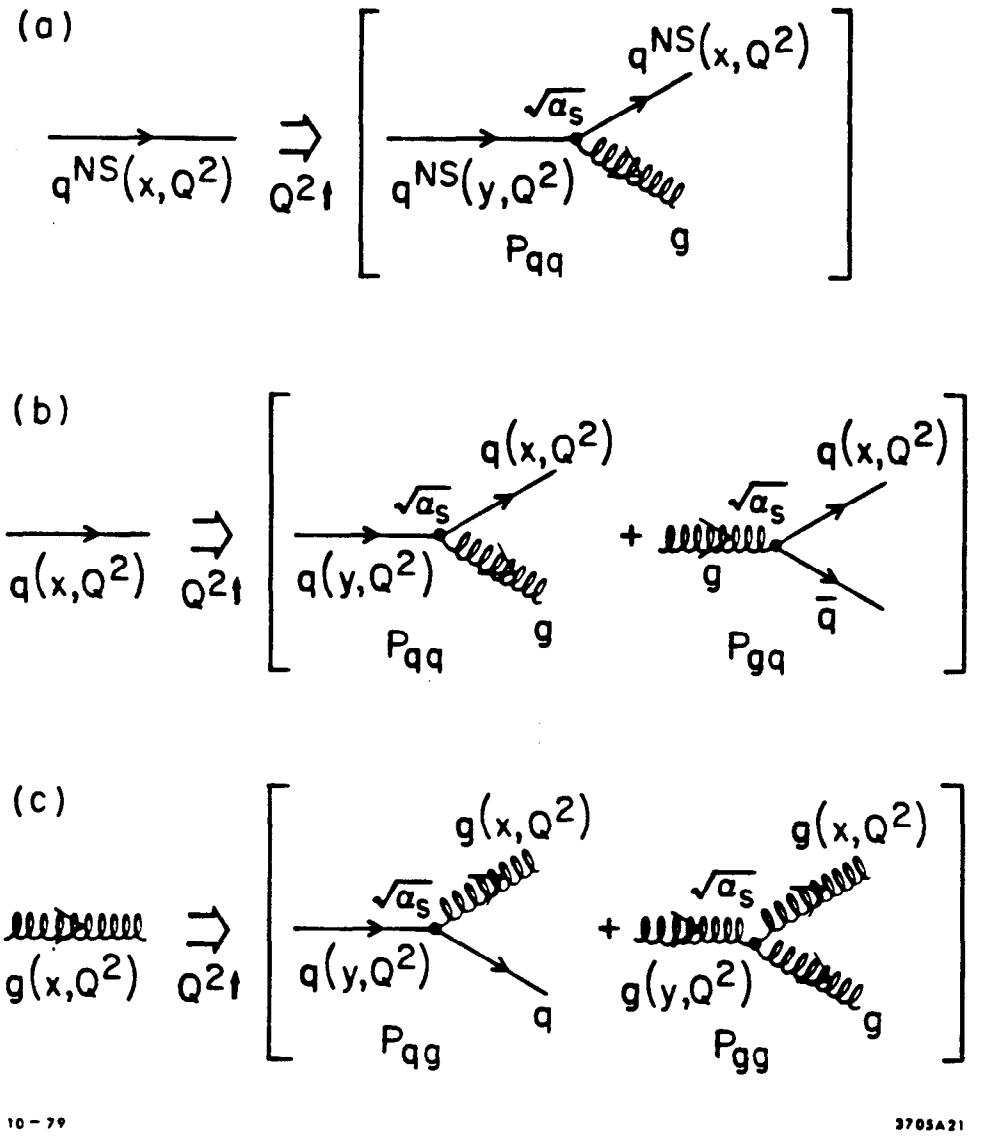

Fig. 64. The evolution of parton structure functions as described in the text for the valence quarks, the sea and the gluons.

Hence from the evolution of the structure functions one is able to measure α_s (Λ). In principle, the most straight-forward method is to use xF_3 in ν interactions since it involves the least input. It is independent of the gluon distribution, uncertainties in R, the amount of the strange sea or charm threshold effects. However it has the largest statistical error. Measurements of F_2 are the most commonly used and have the best statistical accuracy, the major problem being the unknown gluon structure function. One can go to large $x(\gtrsim 0.25)$ to minimize the contribution from the gluon structure function. This also reduces the sensitivity to the sea and charm threshold effects. Or, one can use F_2 and $\bar{q}^{\bar{\nu}}$ to simultaneously extract Λ and G. These methods and variations thereof are used by the experimental groups. The different procedures leads to a wide range of Λ values each subject to its own particular problems. I have chosen values indicative of the work of these groups to indicate the range and accuracy obtained for Λ.

So we see that we obtain measurements of Λ from the evolution of the structure functions. How are the structure functions measured? They are obtained from appropriate combinations of the measured differential cross sections taking into account the complications arising from the sea, charm threshold, quark transverse momentum and mass effects and the W propogator effect.

From ν and $\bar{\nu}N$ scattering one obtains

$$F_2 = \{\frac{\pi}{G_F^2 ME}[\frac{d^2\sigma^\nu}{dxdy} + \frac{d^2\sigma^{\bar{\nu}}}{dxdy}] - 2x(s-c)[1-(1-y)^2]\}$$

$$/[1+(1-y)^2 - y^2 R/(1+R)]$$

$$2xF_1 = F_2/(1+R)$$

$$xF_3 = \frac{\pi}{G_F^2 ME}[\frac{d^2\sigma^\nu}{dxdy} - \frac{d^2\sigma^{\bar{\nu}}}{dxdy}]/\{1-(1-y)^2\}$$

where $R(x,Q^2) = \frac{\sigma_L}{\sigma_T} = \frac{F_L}{2xF_1}$ (F_L accounts for the effects of transverse momentum of the quarks) and (s-c) accounts for the contributions from the strange and

charm quarks inside the nucleon. We expect R to be small for $x \gtrsim 0.3$. Typically experiments use fixed values of R(0–0.2) or QCD predictions. Measurements of R are given at the end of this section.

From eN and μN scattering one obtains

$$F_2 = \frac{Q^4}{8\alpha^2\pi ME}\left(\frac{d^2\sigma}{dxdy}\right)/\{1 - y + \frac{y^2}{2(1+R)}\}.$$

Now to the data. Figure 65 shows the evolution of the F_2 structure function measured by CDHS.[55] The solid line is the leading order QCD prediction, the dashed line the prediction of an Abelian vector gluon model and the dashed-dot the prediction of a scalar gluon model. The data are in good agreement with the leading order QCD but in poor agreement with the non-QCD gauge structures. Figure 66 shows the same measurement from the EMC group using a muon probe (see Ref. 60). Again leading order QCD accounts well for the scaling violations. Table VIII summarizes the Λ measurements from CDHS, CCFRR,[56] CHARM,[57] BPF,[58] BCDMS,[59] and EMC[60] collaborations. The typical range of Q^2 covered by these experiments is 5-200 GeV^2, and Λ is measured using lowest order QCD for all experiments except CDHS where the $\overline{MS}$ scheme is used. These results are shown graphically in Figure 67 where the systematic and statistical errors have been added in quadrature. We may conclude that $\Lambda = 200 \pm 100 MeV$ suitably covers the range of the experimental measurements.

Measurements of R from νN scattering are shown in Fig. 68 where particular attention should be paid to the CDHS data which span a meaningful range of x. One sees that the data are in good agreement with the prediction of QCD and with the assumption of $R \approx 0$ for $x \gtrsim 0.3$ used to extract Λ from F_2, as discussed above.

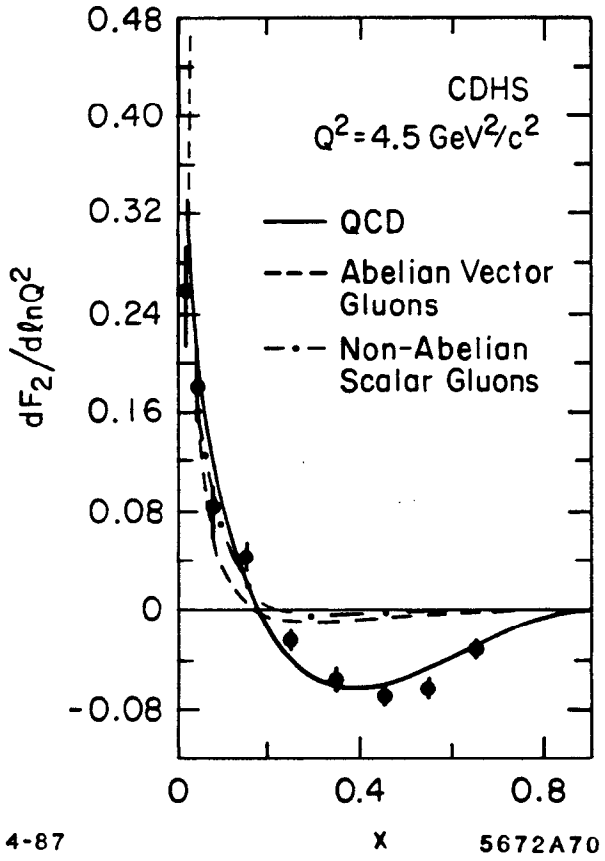

Fig. 65. The slopes of the F_2 structure function $dF_2/d\ell nQ^2$ as a function of x as obtained by CDHS in νN scattering. The solid line is from a leading order QCD fit to F_2 and $\bar{q}$. The dashed lines correspond to non-asymptotically free theories of the strong interactions with scalar and vector gluons.

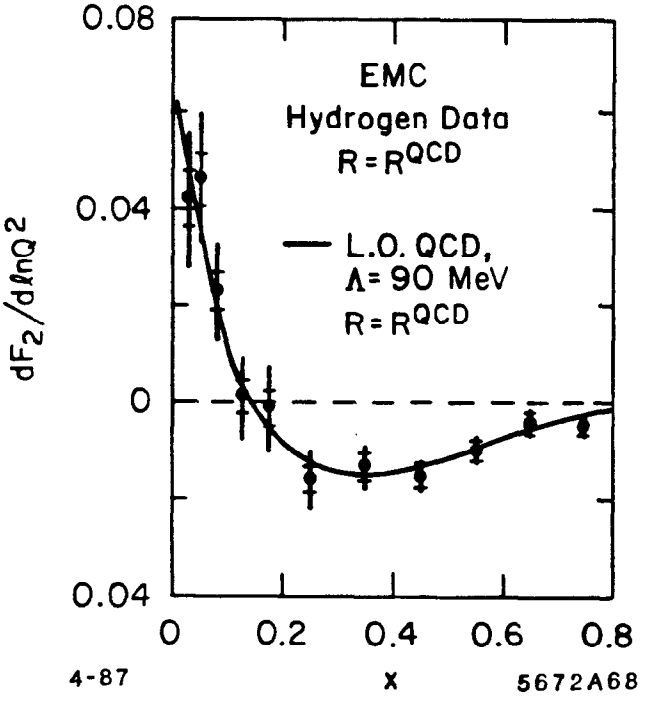

Fig. 66. The slopes of the F_2 structure function as a function of x as obtained by EMC in μN scattering. The inner error bars are statistical the outer ones systematic; a) R = 0.0 and b) R = R_{QCD}. The solid line is the leading order QCD prediction with Λ = 90 MeV.

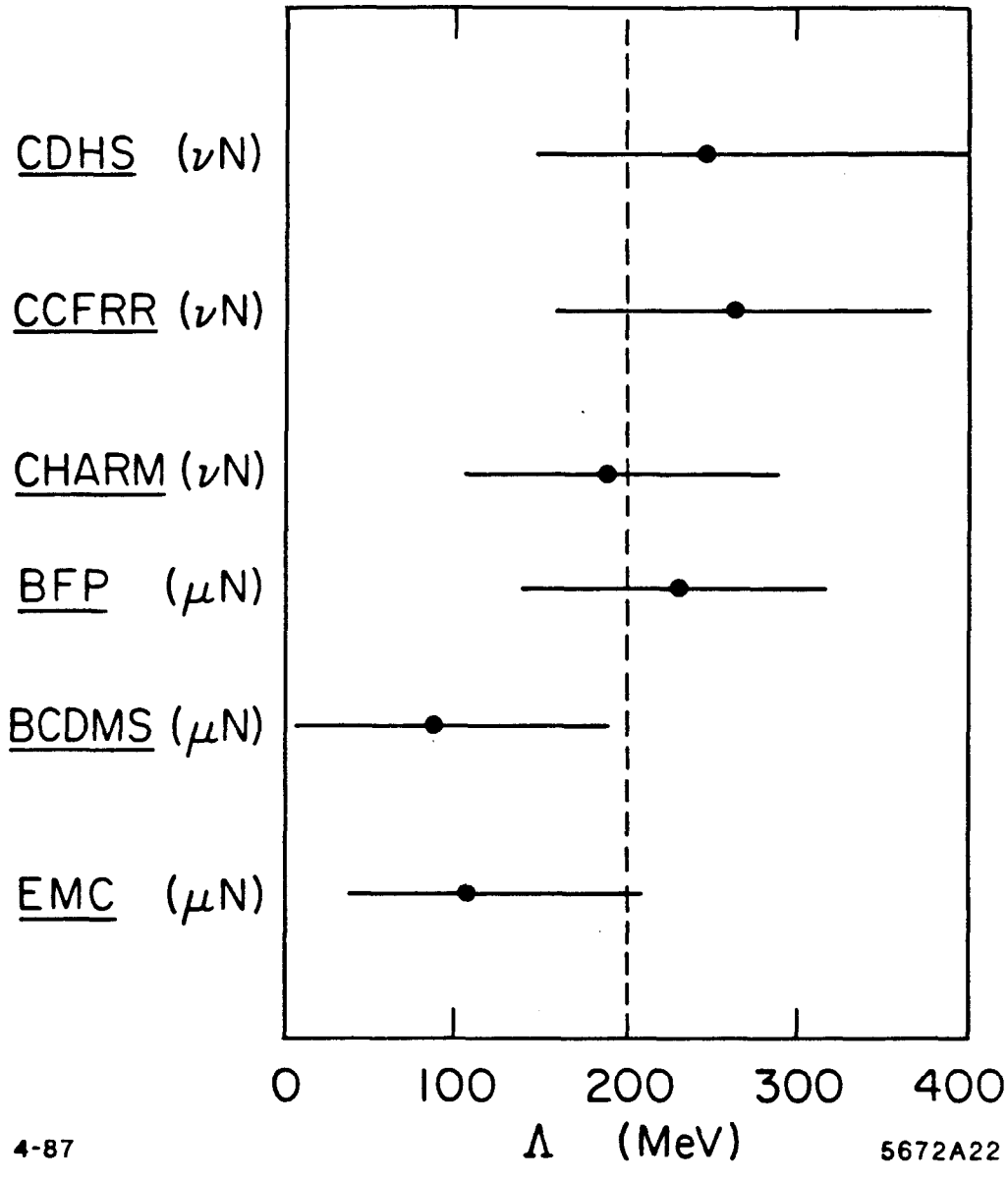

Fig. 67. Summary of the Λ_{LO} measurements of the experiments indicated. $\Lambda = 200 \pm 100$ MeV provides a reasonable summary of these data.

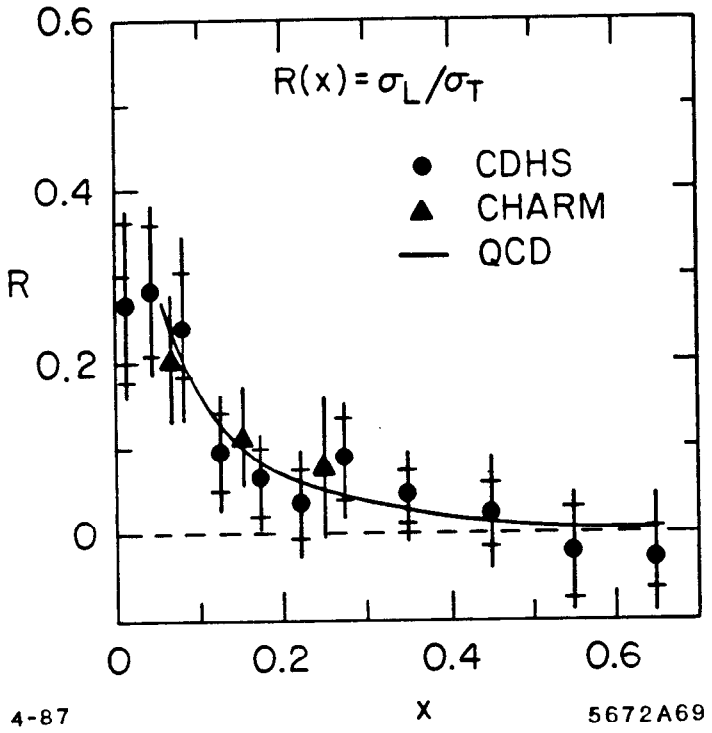

Fig. 68. Measurements of R(x) from the CDHS and CHARM groups.

Table VIII

Group	REF	PROBE	Λ(MeV)
CDHS	55	ν	250^{+150}_{-100}
CCFRR	56	ν	266^{+114}_{-104}
CHARM	57	ν	$190^{+70}_{-40} + 70$
BPF	58	μ	$230 \pm 40 \pm 80$
BCDMS	59	μ	85^{+60+90}_{-40-70}
EMC	60	μ	105^{+55+85}_{-45-45}

6. Measurement of the Photon Structure Function

The two-photon process in high energy e^+e^- collisions has been used to measure the photon structure function, F_2, and extract from it Λ. The process is shown in Fig. 69 where hadrons are produced by the two-photon mechanism with one almost real photon ($P^2 \approx 0$) and one virtual photon ($Q^2 \neq 0$). One can envisage three rather distinct processes as shown in Fig. 70. In Fig. 70(a) at low Q^2, both photons can turn into vector mesons (ρ's) in which case one imagines $\rho\rho$ scattering which has a cross section which falls off like $\frac{1}{Q^4}$ for $Q^2 > M_\rho^2$. As the probing photon becomes more virtual (Fig. 70(b)), it will begin to couple directly to the partons in the target photon thereby sensing the structure of the photon. If scaling holds, the cross section would follow a $1/Q^2$ behavior in this regime. Finally the hadronic part of the photon (Fig. 70(c)) has a pointlike component which is predicted to dominate at large Q^2. In this region the structure function F_2 is expected to rise with Q^2 and show large scaling violations:

$$F_2 \sim \ell n Q^2 \quad and \quad \sigma \sim \frac{1}{Q^2} \ell n Q^2.$$

Using the variables outlined in the previous chapter we can write the differential

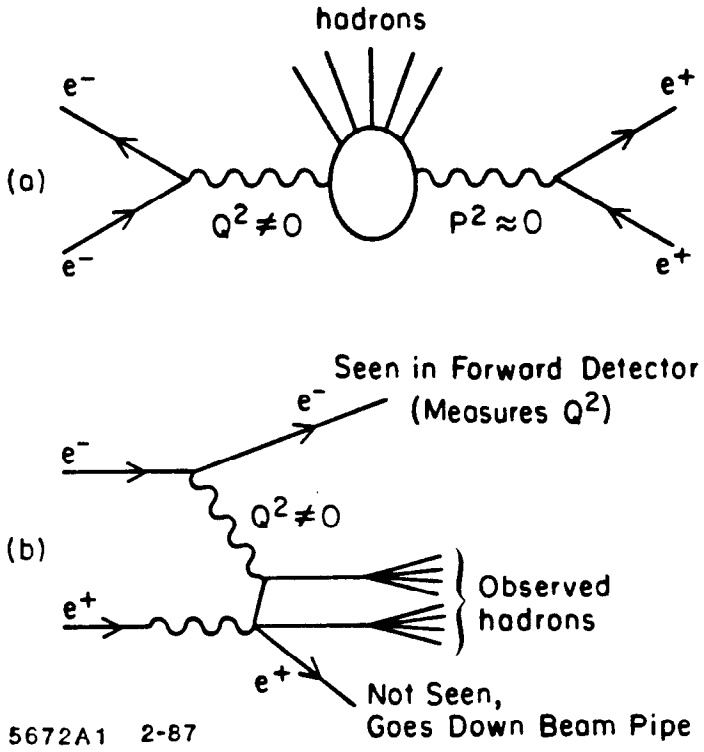

Fig. 69. a) The production of hadrons via the two-photon process in e^+e^- interactions. b) Definition of the kinematics and observables.

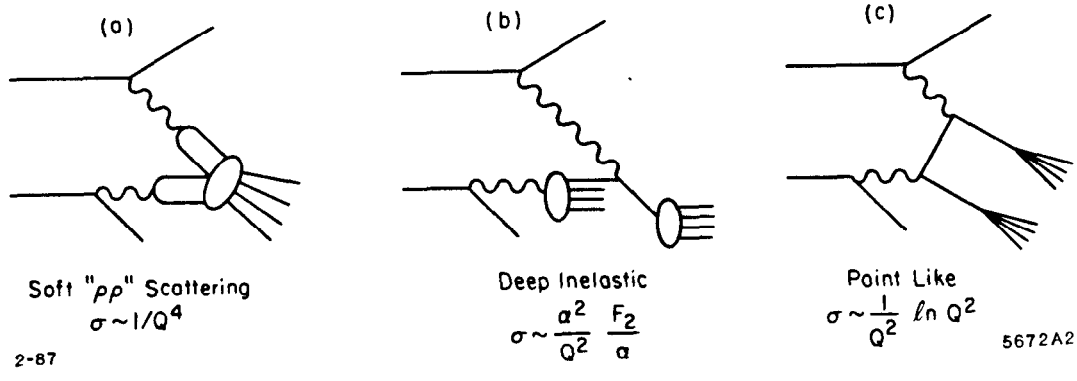

Fig. 70. Three levels of inelasticity in two-photon hadroproduciton.

cross section for $e^+e^- \to e^+e^-$+ hadrons as

$$\frac{d^2\sigma}{dxdy} \propto \frac{1}{Q^4}\{(1-y)F_2 + xy^2F_1\}.$$

Since for the physics to be discussed here xy^2 is small ($\approx$0.01), we can safely ignore the F_1 term. As discussed above, F_2 contains a pointlike piece which has the properties of being absolutely calculable in QCD, $F_2 \propto \frac{1}{\alpha_s(Q^2)} \sim \ell nQ^2/\Lambda^2$ and unlike other F_2 structure functions, F_2^γ rises with x. To counterbalance this rosy picture, the hadronic part of F_2 is not absolutely calculable in QCD and so in reality to extract Λ we need a model for F_2^{HAD}.

The experimental setup is to use a high energy, forward going, $e^\pm$ to tag the two-photon event as indicated in Fig. 69. This tagged $e^\pm$ provides the Q^2 (the $e^\mp$ having proceeded undeviated down the beam line) from $Q^2 = 2EE'$ (1-cosθ) where cosθ is the $e^\pm$ scattering angle, E = E_{beam} and E' is the measured $e^\pm$ energy. The hadronic energy, W, is obtained from the detected hadrons: $W^2_{vis} = \sum P_i^2 < W^2_{true}$. Since $x_{vis} = \frac{Q^2}{Q^2+W^2_{vis}} > x_{true}$. One needs a model to correct x for the unseen hadrons. This introduces a model dependence into the determination of F_2.

How do we confront the measured data? We can calculate the QPM prediction for F_2:

$$F_2^{QPM} = 3(\alpha/\pi)\sum_{q,\bar{q}} e_q^2\{x(1-x)^2)\ell n\frac{W^2}{M_q^2} + 8x^2(1-x) - x\}$$

where M_q, the effective quark mass, is a parameter. One can add a VDM part to this to account for the hadronic piece via

$$F_2^{VDM} = 0.2\alpha(1-x).$$

The leading order QCD calculation gives for the pointlike part

$$F_2^{LO} = 3(\frac{\alpha}{\pi})\sum e_q^2 f(x)\ell n\frac{Q^2}{\Lambda_2}.$$

Higher order, regularized QCD calculations lead to

$$F_2^{H0} = F_2^R(\Lambda_{\overline{MS}}) + \Delta(x,t) + hF^{VDM}, \tag{8}$$

where $\Delta(x,t)$ is the regularization term which has been calculated by Antoniadis and Grunberg[61] in terms of the parameter t. One must be careful to avoid double counting between the Δ and F_2^{VDM} terms, which is typically handled by introducing another parameter, h.

Does the data from tagged two-photon events support the qualitative picture outlined above? (For a comprehensive review see Ch. Berger and W. Wagner.)[62] Figure 71 shows the cross section as a function of Q^2 for $Q^2 < 10\ GeV^2/c^2$. One sees very clearly the transition from $\rho\rho$ scattering to deep inelastic scattering as depicted in Fig. 70. The cross section flattens out markedly for $Q^2 > M_\rho^2$. Can we measure mass scales via the $\ell n\ W^2/M^2$ term which occurs in the formulae for the structure function? To study this the TPC/2γ group have made a measurement of $e^+e^- \rightarrow e^+e^-\mu^+\mu^-$ which can be envisaged as Fig. 70(c) with the quark lines replaced by muons. According to our QED calculation, F_2 for this process should be proportional to $\ell n\ W^2/M_\mu^2$. The data are shown in Fig. 72 with predictions of the QED assuming M_μ= 50, 105 and 200 MeV/c^2. With this method, M_μ is measured to $\pm 5\%$ which clearly indicates that a measurement of F_2 has considerable sensitivity to a mass scale.

Does one see the point-like structure of the photon, i.e., does F_2 increase with increasing Q^2? Again the answer is yes as seen in Figs. 73 and 74. Figure 73 shows the PLUTO data for F_2 as a function of x for three Q^2 bins. Figure 74 shows a compilation of data for $< F_2/\alpha >$ as a function of Q^2. One sees quite clearly that the structure function grows with increasing Q^2. The growth is consistent with the QCD prediction of a+b $\ell nQ^2/\Lambda^2$ but would equally well be fit with the QPM form $a' + b'\ell nQ^2/M_{eff}^2$. We can see this same trend in Fig. 75 which shows F_2/α as a function of x from the PLUTO collaboration. The predictions of QCD (both lowest order and higher order, Λ= 200 MeV) and QPM

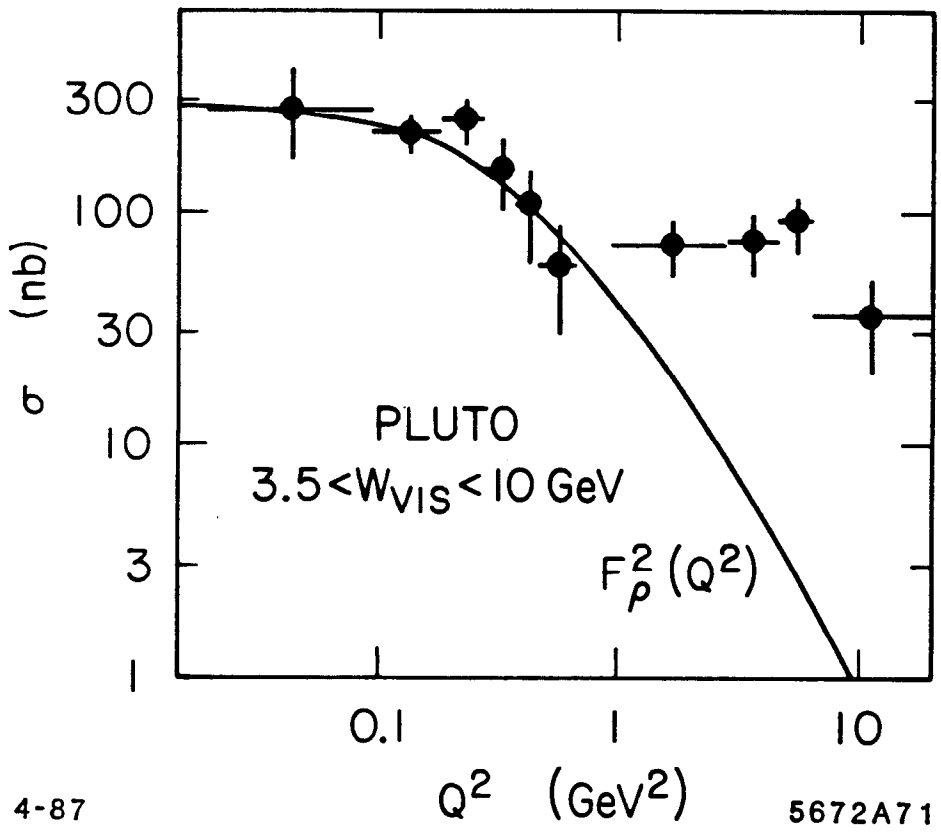

Fig. 71. The two-photon cross section as a function of Q^2 from the PLUTO group. The curve is the contribution for $\rho\rho$ scattering.

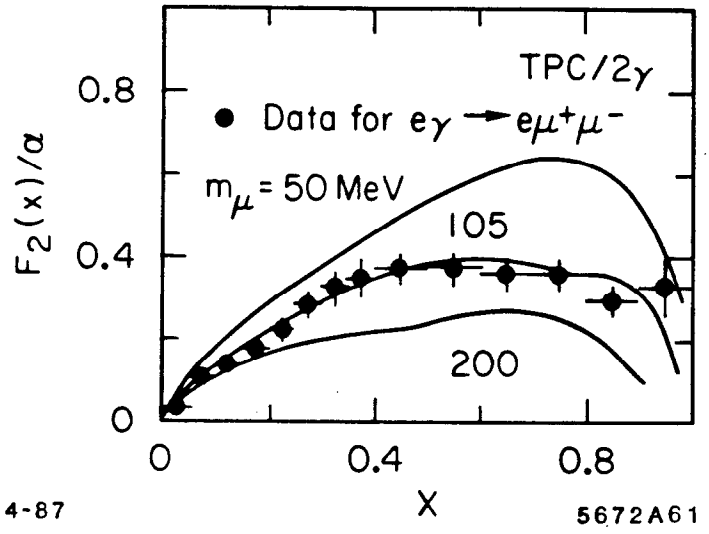

Fig. 72. The structure function for $e\gamma \to e\mu^+\mu^-$ from the TPC/2γ group. The curves are predictions of the QPM with the muon mass as indicated.

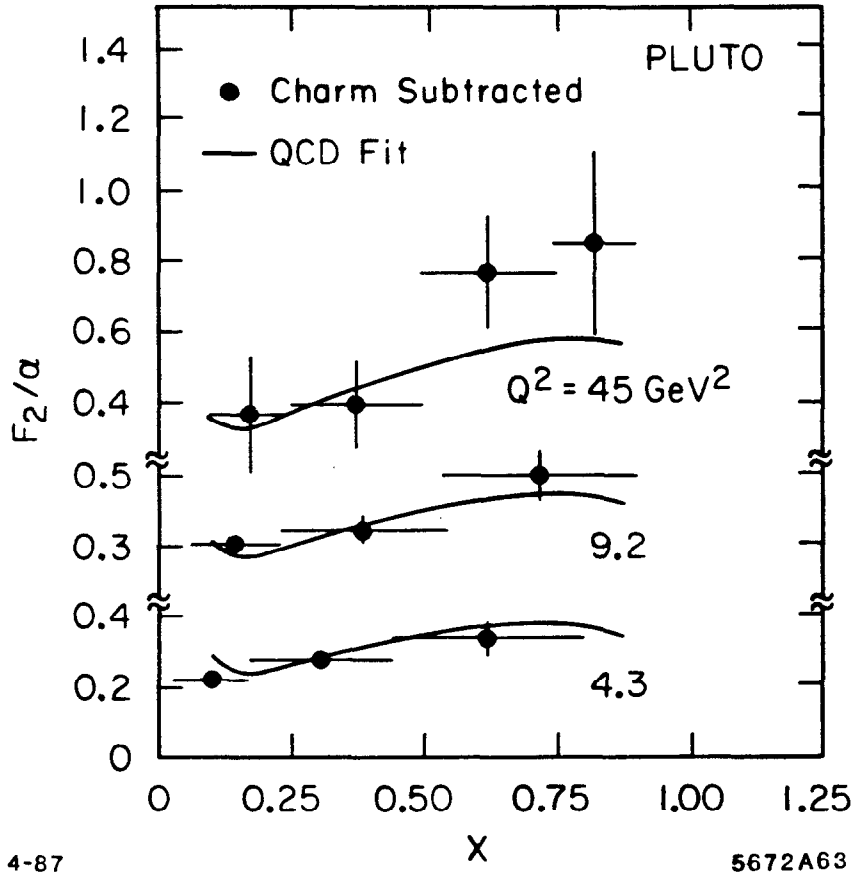

Fig. 73. The structure function for $e\gamma \rightarrow e+$ hadrons as measured by PLUTO for three Q^2 bins. The solid lines are the fits to QCD with $\Lambda = 183$ MeV.

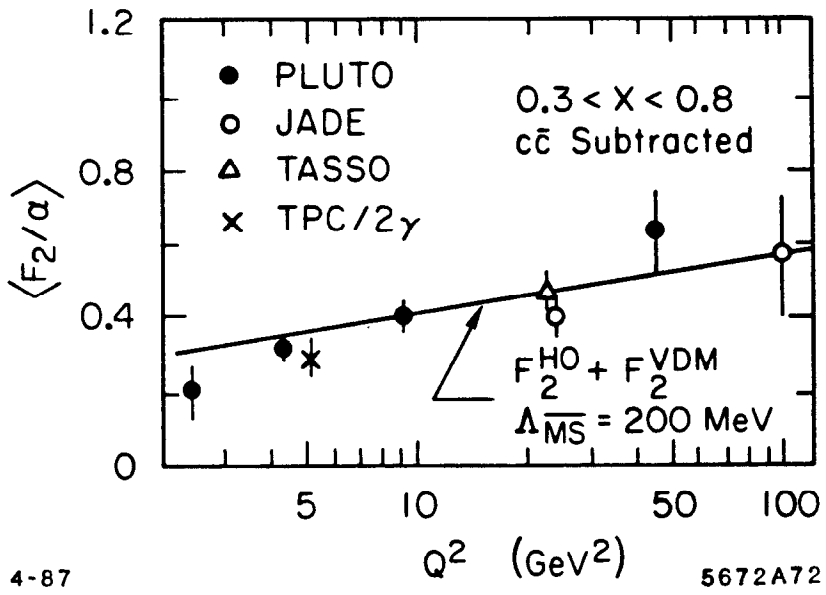

Fig. 74. Compilation of data for $< F_2/\alpha >$ as a function of Q^2. The clear growth of F_2 with Q^2 is seen.

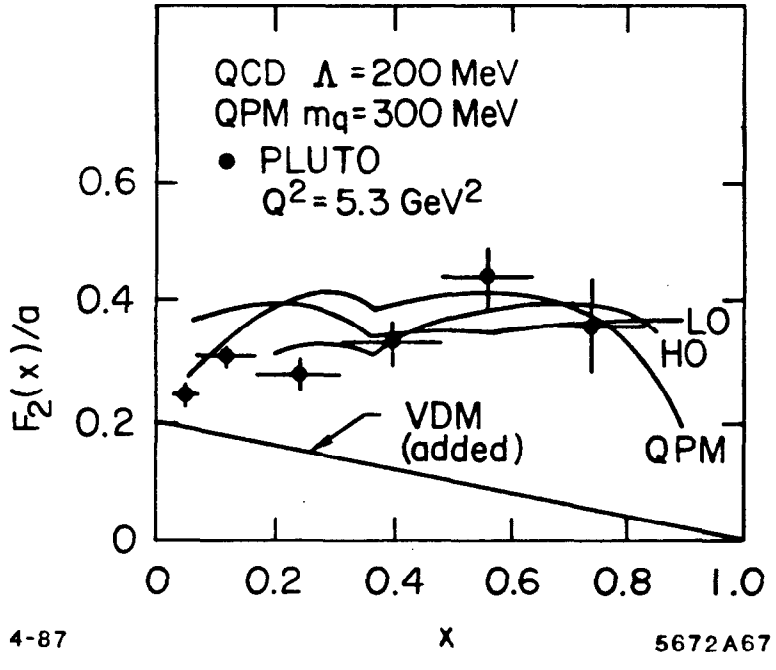

Fig. 75. The structure function for $e\gamma \rightarrow e+$ hadrons as a function of x as measured by PLUTO. The curves show the contribution from VDM which is added to the predictions of QPM and QCD with $\Lambda = 200$ MeV. Both lowest order and higher order QCD cures are shown.

are shown where the VDM piece has been added in to account for the hadronic contribution. One sees that QCD and QPM do equally well at approximating the data; it would seem that the data alone do not require anything beyond QPM. This same result is achieved by many groups (see Ref. 62). However one should note that to get the QPM to fit requires assuming quark masses of 300 MeV/c^2. However under the more realistic assumption of current masses, the QPM prediction is about 2-3 times too large. One may interpret this result then by saying that one is seeing clear gluon effects which are "dressing" up bare quark masses to effective masses of $\sim$ 300 MeV/c^2. In the spirit then, that QCD can account for the data, how well can we extract Λ?

All the data presented here are analyzed using the regularization scheme of Antoniadis and Grunberg. It should be pointed out that this procedure is controversial and subject to a fair amount of criticism. (For a flavor of this see the discussion of Field et al.[63] The data of PLUTO,[64] TASSO[65] and JADE[66] are shown in Figs. 76, 77 and 78. The PLUTO data (see also Fig. 73) are fit using the form of Equation 8 with Λ, t and h as parameters. While h and t are strongly correlated, and hence are not well determined, Λ is relatively insensitive to this correlation. The value extracted is

$$\Lambda_{\overline{MS}} = 183^{+65+46}_{-40-36}\ MeV \qquad (PLUTO; Q^2 : 3 - 100\ GeV^2/c^2).$$

Both JADE and TASSO assume the hadronic piece of F_2 goes like $F_2^{HAD} = 0.2$ (1-x) and fix the value of t (= 1, 0, respectively) to obtain

$$\Lambda_{\overline{MS}} = 140^{+190}_{-65}\ MeV \qquad (TASSO; Q^2 : 7 - 70\ GeV^2/c^2)$$

$$= 250 \pm 90\ MeV \qquad (JADE; Q^2 : 10 - 220\ GeV^2/c^2)$$

The fits to the data are shown in the figures. All the experiments correct for the effects of charm quark production. Ignoring the fact that the three experiments

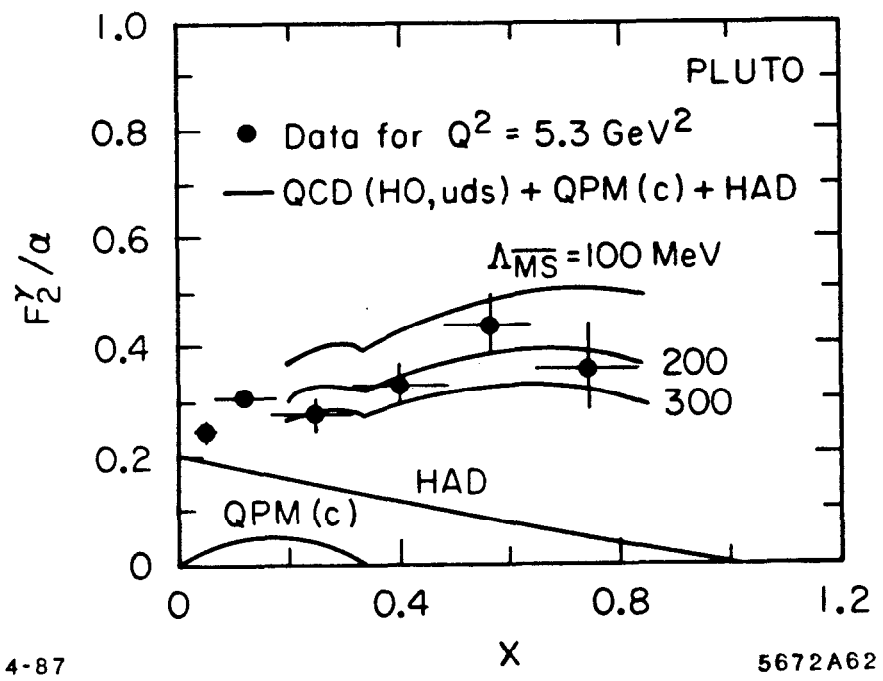

Fig. 76. PLUTO data used to extract $\Lambda_{\overline{MS}}$.

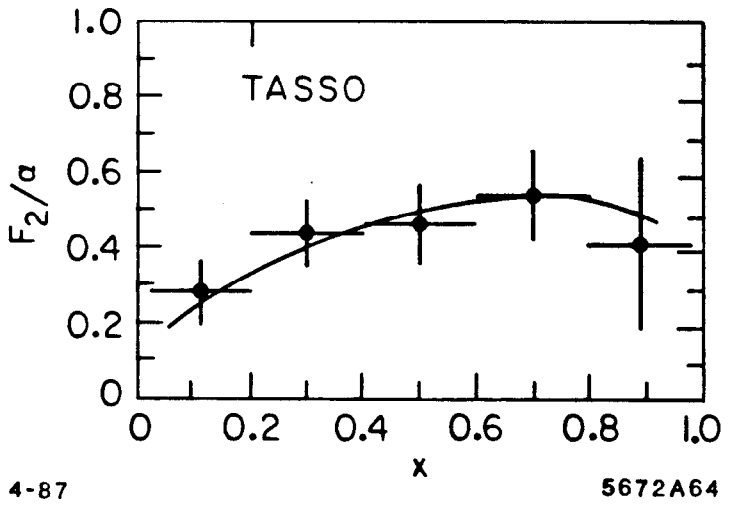

Fig. 77. TASSO data used to extract $\Lambda_{\overline{MS}}$.

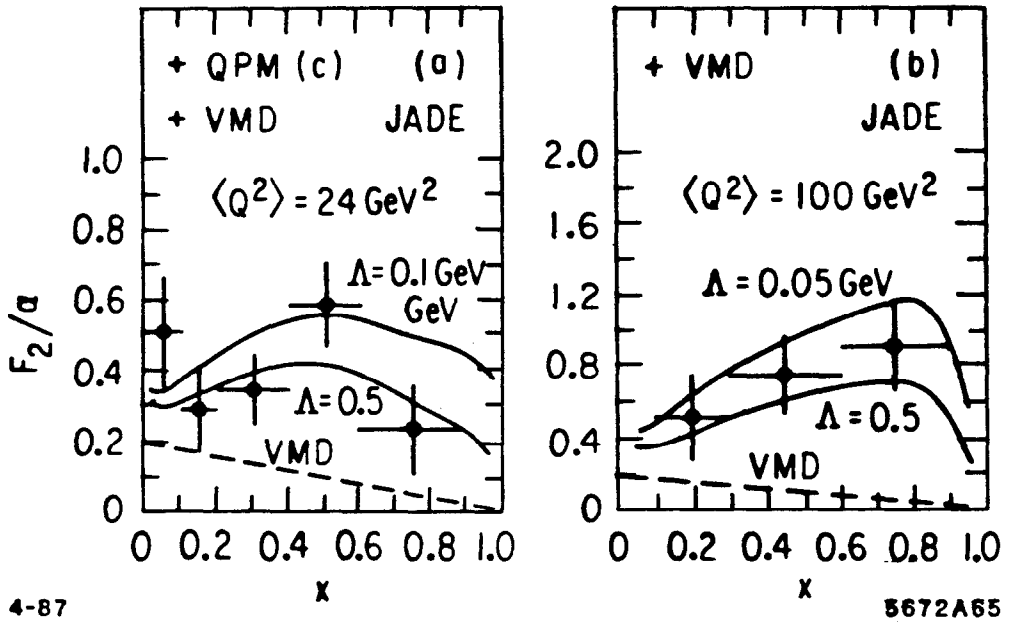

Fig. 78. JADE data used to extract $\Lambda_{\overline{MS}}$.

have different $< Q^2 >$ and correlated errors (since their procedures are very similar), one can blindly average the three measurements to obtain

$$\Lambda_{\overline{MS}} = 195^{+60}_{-40}. \qquad < Q >^2 \approx 50\ GeV^2.$$

This is an impressively precise measurement, although there still exist issues associated with the appropriateness of the regularization scheme and the use of a pion-like form factor for the hadronic component of F_2. Some light has been shed on the latter question by the TPC/2γ group who have used low Q^2 data (Q^2 <1.6 GeV^2) to measure F_2^{HAD}. Their data, shown in Fig. 79, agree with the form $F_2^{HAD} = 0.2\alpha(1-x)$ except at small x. So it seems that this may not be a large uncertainty since the sensitivity to Λ comes mainly from the higher x data.

7. Conclusions

We have reviewed a large body of data which relates to testing QCD. We see that the qualitative agreement between the data from a very wide range of processes and QCD is very impressive. This agreement is non-trivial in the sense that there exist no other theories or models which fit the data nearly as well.

Quantitatively we see that quarks have spin $\frac{1}{2}$ and come in three colors and that gluons are vector-like particles. We do not see direct experimental evidence for the triple gluon vertex; however most data are poorly fit ($\bar{p}p$ at CERN in particular) without such a contribution. Further indirect evidence comes from the fact that gluons appear to have a softer fragmentation function than quarks.

Extracting the QCD scale Λ is problematical and there exists no processes where a precise, non-controversial measurement can be made. All measurements seem entangled with either experimental or theoretical problems or both. However if we assume that all the measurements taken as a whole "average out" these problems, one is left reasonably satisfied with $\Lambda_{QCD} = 150 \pm 100$ MeV.

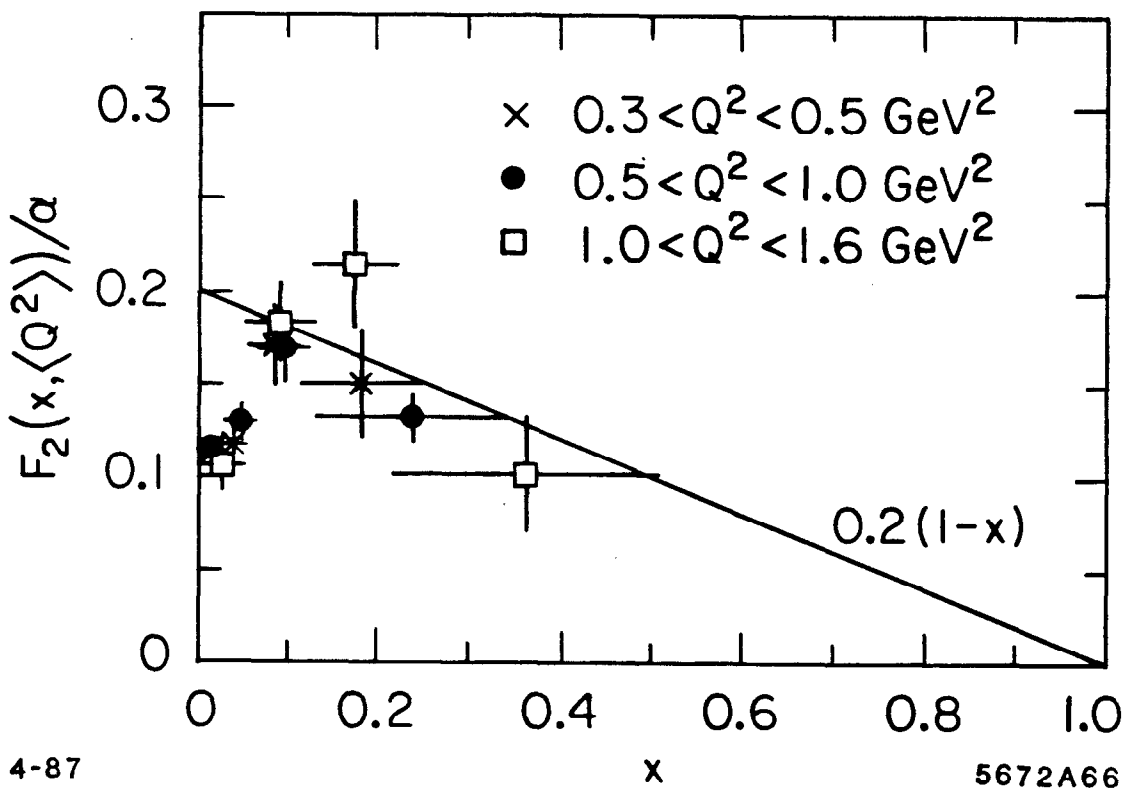

Fig. 79. The structure function as a function of x at low $< Q^2 >$ as measured by the TPC/2γ group. The curve is 0.2(1-x).

My final conclusion would be that QCD is a magnificent theoretical edifice and success. There exists no evidence from experiment to doubt its validity and, with time, I would expect the quantitative tests will be improved.

8. Acknowledgements

I wish to thank the organizers of the 1986 SLAC Summer Institute for inviting me to give these lectures and applaud them for their patience in waiting for this write-up. I wish to thank Sharron Lankford for her care and patience in the preparation of this document. Finally my thanks to the SLAC Illustrations Department for the preparation of the many figures.

References

1. M. Dine and J. Sapirstein, Phys. Rev. Lett. 43, 668 (1979); K. G. Chetyrkin et al., Phys. Lett. 85B, 277 (1979); W. Celmaster and R. J. Gonsalves, Phys. Rev. Lett. 44, 560 (1980).
2. E. Fernandez et al., Phys. Rev. D31, 1537 (1985).
3. H.-J. Behrend et al., Phys. Lett. B183, 400 (1987).
4. PLUTO: Phys. Rep. 83, 153 (1982).
   JADE: Phys. Lett. B129, 145 (1983); B160, 337 (1985); DESY Report 86-113.
   MARK J: Phys. Rev. D34, 681 (1986).
   TASSO: Phys. Lett. B113, 499 (1982); 138, 441 (1984).
5. Sau Lan Wu, Physics Reports 107, 59 (1984).
6. G. Hanson et al., Phys. Rev. Lett. 35, 1609 (1975).
7. J. Dorfan, Proceedings of the 1982 SLAC Summer Institute on Particle Physics.
8. See for instance: P. Söding, Proceedings of the EPS High Energy Conference, Brighton, 567 (1983) or J. Dorfan, Proceedings of the 1983 International Symposium on Lepton and Photon Interactions at High Energies, Cornell, 686.
9. R. K. Ellis et al., Nucl. Phys. B178, 421 (1981).
10. J. Vermasseren et al., Nucl. Phys. B187, 301 (1981).
11. K. Fabricius et al., Phys. Lett. 97B, 431 (1980).
12. F. Gutbrod et al., Z. Phys. C21, 235 (1984).
13. Ren-yuan Zhu, Proceedings of the 1985 Annual Meeting of the DPF, Oregon, 552.
14. Yu. L. Dokshister et al., Phys. Lett. 78B, 290 (1978); C. L. Basham et al., Phys. Rev. Lett. 41, 1585 (1978); Phys. Rev. D19, 2018 (1979).
15. T. Sjostrand, Comp. Sci. Comm. 27, 243 (1982); T. Sjostrand, Comp. Sci. Comm. 28, 229 (1983); B. Anderson et al., Z. Phys. C6, 235 (1980); Nucl. Phys. B197, 45 (1982).
16. A. Ali et al., Phys. Lett. 93B, 155 (1980).
17. P. Hoyer et al., Nucl. Phys. B161, 349 (1979).
18. M. Althoff et al., Z. Phys. C26, 157 (1984).
19. H. Behrend et al., Phys. Lett. 138B, 311 (1984).

20. W. Bartel et al., Z. Phys. C25, 231 (1984).

21. Ch. Berger et al., Z. Phys. C28, 365 (1985).

22. B. Adeva et al., Phys. Rev. Lett. 50, 2051 (1983).

23. E. Fernandez et al., Phys. Rev. D31, 2724 (1985).

24. T. D. Gottschalk and M. P. Shatz, Phys. Lett. 150B, 451 (1985).

25. B. Adeva et al., Phys. Rev. Lett. 54, 1750 (1985).

26. M. B. Einhorn and B. G. Weeks, Nucl. Phys. B146, 445 (1978); K. Shizuya and S. -H. H. Tye, Phys. Rev. Lett. 41 787 (1978).

27. W. Bartel et al., Phys. Lett. 123B, 460 (1983).

28. A. Petersen et al., Phys. Rev. Lett. 55, 1954 (1985).

29. G. Arnison et al., Nucl. Phys. B276, 253 (1986).

30. JADE: Z. Phys. C21, 37 (1983); Phys. Lett. 134B, 275 (1984); 157B, 340 (1985). TPC: Z. Phys. C28, 31 (1985). TASSO: Z. Phys. C29, 29 (1985).

31. Ya. I. Azimov et al., Phys. Lett. 165B, 147 (1985).

32. M Aihara et al., Phys. Rev. Lett. 57, 945 (1986).

33. P. Sheldon et al., Phys. REv. Lett. 57, 1398 (1986).

34. B. L. Combridge, J. Kripfganz and J. Ranft, Phys. Lett. 70B, 234 (1977).

35. G. Arnison et al., Phys. Rev. Lett. B172, 461 (1986).

36. P. Bagnaia et al., Phys. Lett. 160B, 349 (1985).

37. AFS: Phys. Lett. 123B, 133 (1983); 118B, 193 (1982).

38. T. Åkesson et al., Phys. Lett. 158B, 282 (1985).

39. J. A. Appel et al., Phys. Lett. 176B, 239 (1986).

40. P. Aurenche et al., Phys. Lett. 140B, 87 (1984).

41. E. Auge et al., Phys. Lett. 182B, 409 (1986).

42. P. Aurenche et al., Z. Phys. C24, 309 (1984).
D. W. Duke and J. F. Owens, Phys. Rev. D26, 1600 (1982) and erratum Phys. Rev. D28 (1983).

43. G. Arnison et al., Phys. Lett. 136B, 294 (1984).

44. P. Bagnaia et al., Phys. Lett 144B, 283 (1984).

45. G. Arnison et al., Phys. Lett. 158B, 494 (1985).

46. T. Åkesson et al,. Z. Phys. C32, 317 (1986)

47. F. Ceradini, CERN-EP/86-142, talk given at the 23rd International Conference on High Energy Physics, Berkeley, CA. July 1986; Phys. Lett. 158B, 494 (1985).
48. J. A. Appel et al., Z. Phys. C30, 341 (1986).
49. S. J. Brodsky et al., Phys. Rev. D28, 228 (1983).
50. S. E. Csorna et al., Phys. Rev. Lett. 56, 1222 (1986).
51. R. D. Schamberger et al., Phys. Lett. 138B, 225 (1984).
52. D. Photiadis, Phys. Lett. 164B, 160 (1985).
53. R. D. Field, Phys. Lett. 133B, 248 (1983).
54. D. W. Duke and R. G. Roberts, Physics Reports 120, 175 (1985); W. Atwood, Proceedings of the 1980 SLAC Summer Institute on Particle Physics. For recent updates: J. Carr, Proceedings of the 1985 Annual Meeting of the DPF , Oregon, 512; G. Altarelli, Proceedings of the EPS High Energy Conference, Bari, 731 (1985).
55. CDHS: Z. Phys. C17, 283 (1983).
56. CCFRR: Z. Phys. C26, 1 (1984).
57. CHARM: Phys. Lett. 123B, 269 (1983).
58. BPF: Phys. Rev. Lett. 51, 1826 (1983).
59. BCDMS: Phys. Lett. 104B, 403 (1981).
60. EMC: Nucl. Phys. B259, 189 (1985).
61. I. Antoniadis and G. Grunberg, Nucl. Phys. B213, 445 (1983).
62. Ch. Berger and W. Wagner, UCD-86-16, PITHA-86-09.
63. J. H. Field et al., DESY 86-073.
64. PLUTO: Phys. Lett. 142B, 111 (1984).
65. TASSO: Z. Phys. C31, 527 (1986).
66. JADE: Z. Phys. C24, 231 (1984). TEX A1